In vivo study on children of the mechanical behavior of thorax and the mechanical properties of ribs

Yumin Zhu

Université Claude Bernard Lyon 1

UNIVERSITÉ DE LYON

N° d'ordre : 72-2014 Année 2014

THESE DE L'UNIVERSITE DE LYON

Délivrée par

L'UNIVERSITE CLAUDE BERNARD LYON 1

et préparée en cotutelle avec

UNIVERSITE TONGJI

ECOLE DOCTORALE MEGA

DIPLOME DE DOCTORAT
(arrêté du 7 août 2006 / arrêté du 6 janvier 2005)

Présentée et soutenue publiquement le 20 Mai 2014

par

ZHU Yumin

Evaluation *in vivo* chez l'enfant du comportement mécanique du thorax et des propriétés mécaniques des côtes

Directeur de thèse: **MITTON David**
Co-directeur : **WANG Hongyan**
Encadrant : **BERMOND François**

JURY :

SKALLI Wafa	Professeur des Universités, ENSAM, Paris	Examinateur
PITHIOUX Martine	Chargée de Recherche, CNRS, Marseille	Rapporteur
SWIDER Pascal	Professeur des Universités, Université Toulouse III, Toulouse	Rapporteur
PIALAT Jean-Baptiste	Professeur des Universités, Université Claude Bernard Lyon 1	Examinateur
WANG Hongyan	Professeur des Universités, Université Tongji, Shanghai	Examinateur
BERMOND François	Chargé de Recherche, IFSTTAR, Lyon	Examinateur
MITTON David	Directeur de Recherche, IFSTTAR, Lyon	Examinateur

Evaluation *in vivo* chez l'enfant du comportement mécanique du thorax et des propriétés mécaniques des côtes

Les données biomécaniques sur les enfants sont rares et difficiles à obtenir lors d'expérimentations. Cette recherche s'intéresse à l'évaluation *in vivo* du comportement mécanique du tronc et des propriétés mécaniques de l'os cortical des côtes.
Le comportement mécanique *in vivo* du tronc de l'enfant et de l'adulte sous charge pendant des manipulations de kinésithérapie respiratoire ont été étudiées. Trois formes typiques de courbes de force en fonction du déplacement ont été observées. Un plus grand décalage en temps entre les courbes de force en fonction du temps et les courbes de déplacement en fonction du temps ont été observés plus fréquemment chez les enfants que chez les adultes, ce qui conduit à différentes formes de courbes de force en fonction du déplacement entre les enfants et les adultes. Parmi les paramètres qui peuvent affecter le comportement mécanique du tronc, les propriétés mécaniques de l'os cortical des côtes ont été étudiées. Dans un premier temps, il a été constaté *ex vivo* que les propriétés mécaniques de l'os cortical des côtes des adultes sont liées de façon linéaire à la Densité Minérale Osseuse (DMO) mesurée par la tomodensitométrie quantitative (Quantitative Computed Tomography, QCT) et la tomographie périphérique quantitative à haute résolution (High Resolution Peripheral Quantitative Computed Tomography, HR-pQCT). La DMO peut être mesurée par QCT *in vivo*. Ensuite, les relations entre la DMO et les propriétés mécaniques pour l'adulte ont été appliquées aux enfants, et les propriétés mécaniques de l'os cortical de l'enfant ont pu être estimées. Les propriétés mécaniques ont été trouvées plus élevées dans la partie latérale des côtes que dans les régions antérieures et postérieures. Il a également été constaté que les propriétés mécaniques augmentent au cours de la croissance. Il s'agite la première étude qui a évalué les propriétés des matériaux de l'os cortical des côtes de l'enfant *in vivo*.
Cette étude peut aider à mieux comprendre la réponse mécanique du tronc de l'enfant et les propriétés mécaniques de l'os cortical costal. A court terme, ces résultats mesurés *in vivo* seront considérés dans des modèles éléments finis du tronc de l'enfant.

***In vivo* study on children of the mechanical behavior of thorax and the mechanical properties of ribs**

Biomechanical data on children, both mechanical behaviors and tissue properties, are rare and difficult to be obtained through biomechanical experiments. This thesis mainly discussed the mechanical behavior of pediatric trunk and mechanical properties of pediatric rib cortical bones *in vivo*.
The mechanical responses of the living and active pediatric and adult trunks during *in vivo* loading tests were investigated. Three typical shapes of force-displacement curves were observed. Larger time lags between force time histories and displacement time histories were observed more frequently in children than adults, resulting in different shapes of force-displacement curves between children and adults. To better understand the mechanical behavior of pediatric trunk, rib cortical bone mechanical properties were studied. It was found that mechanical properties of adult rib cortical bones were linearly related to Bone Mineral Density (BMD) measured by Quantitative Computed Tomography (QCT) and High Resolution Peripheral Quantitative Computed Tomography (HR-pQCT). The BMD could be measured by QCT *in vivo*. Then, the mechanical property-BMD relationships were introduced to child population, and the mechanical properties of pediatric rib cortical bones were estimated. The mechanical properties were found higher in the lateral part of the ribs than the anterior and posterior regions. It was also found that the mechanical properties were growing during the growth of children. This is the first study which estimated the material properties of pediatric rib cortical bones *in vivo*.
This study can help to better understand the mechanical response of pediatric trunk and mechanical properties of pediatric rib cortical bones. These results measured *in vivo* could contribute to improve the biofidelity of pediatric modeling.

DISCIPLINE : Biomécanique

MOTS-CLES :
Biomécanique, l'enfant, tronc, l'os cortical des côtes, Densité Minérale Osseuse (DMO), *in vivo*

Laboratoire de Biomécanique et Mécanique des Chocs – UMR_T9406 (Ifsttar – UCBL)
25 avenue François Mitterrand, Case 24, 69675 Bron cedex, France

Foreword

This thesis was conducted in collaboration with: the LBMC (Laboratoire de Biomécanique et Mécanique des Chocs, IFSTTAR, Lyon), the LBM (Laboratoire de Biomécanique, ENSAM, Paris), Hôpital d'Instruction des Armées Desgenettes (Lyon), Hôpital Edouard Herriot (Lyon), Hôpital Femme Mère Enfant (Lyon), and Tongji University (Shanghai, China).

This manuscript is written in English. A summary in French can be found at the end of this report. This work is supported by the Clusters-ARC from the Région Rhône-Alpes.

I would like to first thank my advisor - Dr. David Mitton - for the vital encouragement, patient guidance, and invaluable advice that he has given me throughout my graduate study. I would also like to thank Dr. François Bermond, for his kindness help, valuable suggestions, and generous assistance.

I would also like to thank Dr. Philippe Verzin, the director of LBMC, for his kind acceptance and help. I also own my acknowledgement to Dr. Dominique Cesari, without whom, I might not have the opportunity to come to LBMC.

I would like to thank Pr. Hongyan Wang, my supervisor in China, for her endlessly help and constant guidance.

This work would not have been possible without Pr. Wafa Skalli, the director of LBM, and Dr. Baptiste Sandoz. Thank you for your warm acceptance and crucial assistances. The same acknowledge should go to Benjamin Aubert, Thomas Joubert and Dr. Claudio Vergari, for their kind help during my stay in LBM.

I would like to thank Dr. Martine Pithioux and Pr. Pascal Swider for accepting the review of my work, as well as Pr. Jean-Baptiste Pialat for his valuable discussions and taking part in the jury committee.

I would like to thank Pr. Jean-Pierre Pracros and Dr. Jacqueline Payen de la Garanderie, for proving us the pediatric CT images.

I would also like to thank the students and staffs of LBMC. They have been both friends and colleagues and I will always be grateful for having been a member of the LBMC family. I especially want to thank Junfeng Peng and Romain Desbats for their correction of the summary in French.

The last but not least, my thanks would also go to my beloved parents and girl Shuangshuang Liu, for their boundless love and whole-hearted support over all these past years.

Publication:

Yumin Zhu, Karine Bruyère-Garnier, David Mitton, Emmanuel Vajda, and François Bermond. (2014). Mechanical behaviour of the in vivo paediatric and adult trunk during respiratory physiotherapy. *Proceedings of the Institution of Mechanical Engineers, Part H: Journal of Engineering in Medicine, 228 (1): 27-36.* First published on November 26, 2013. DOI: 10.1177/0954411913512282.

Conferences and communications:

Yumin Zhu, Karine Bruyère-Garnier, David Mitton, and François Bermond. Comparison between the mechanics of the in vivo child and adult trunk during chest physiotherapy. *ISN Workshop on Biomechanical Experiments, September 10, 2012, Dublin, Ireland*.

Yumin Zhu, Yuan Fang, François Bermond, Karine Bruyère-Garnier, Rafaa Ellouz, Frederic Rongieras, and David Mitton. Relationship between human rib mechanical properties and cortical bone density measured by high-resolution quantitative computed tomography. *The 38th Congress of the Société de Biomécanique, September 3-6, 2013, Marseille, France. Computer Methods in Biomechanics and Biomedical Engineering, 16 (sup1): 191-192, 2013*. DOI: 10.1080/10255842.2013.815888.

Yumin Zhu, François Bermond, Jacqueline Payen de la Garanderie, Jean-Baptiste Pialat, Baptiste Sandoz, Jean-Pierre Pracros, Wafa Skalli, and David Mitton. *In vivo* assessment of the mechanical properties of the child cortical bone using quantitative computed tomography. *The 7th World Congress of Biomechanics, July 6-11, 2014, Boston, MA, USA. (accepted).*

David Mitton, **Yumin Zhu**, Jacqueline Payen de la Garanderie, Jean-Baptiste Pialat, Baptiste Sandoz, Jean-Pierre Pracros, Wafa Skalli, and François Bermond. *In vivo* characterization of the child rib mechanical properties using quantitative computed tomography. *The 12th international symposium on Computer Methods in Biomechanics and Biomedical Engineering, October 13-15, 2014, Amsterdam, Netherlands. (accepted).*

Contents

Introduction

Motor vehicle crashes are one of the leading causes of death and injury for children all over the world (WHO, 2013). In case of a crash, trunk (thorax and abdomen) is one of the main injured body regions for children (Crandall et al., 2013). Thus, this study will focus on pediatric trunk.

Research efforts are ongoing in the area of pediatric biomechanics for traffic safety. To better understand the child biomechanical behavior, various attempts have been made such as Post-Mortem Human Subject (PMHS) tests (Kallieris et al., 1976; Kent et al., 2011; Kent et al., 2009; Ouyang et al., 2006), animal surrogate tests (Arbogast et al., 2005; Kent et al., 2006), non-injury observation on volunteers (Sandoz et al., 2011). However, achievements on pediatric subjects are limited comparing to those on adults (Franklyn et al., 2007). Pediatric materials are hard to collect and tests on child population are difficult to perform.

Anthropomorphic test devices (ATD) and computational models are important tools to study pediatric biomechanics. Knowledge of child biomechanical behavior is therefore requested. The paucity of pediatric data has led to the development of pediatric models through scaling of adult data. Due to the lack of material property data, quantitative age-dependent anatomical data and pediatric impact response data, no thoracic model has been developed directly from pediatric data till now. Children differ from adults not only in geometric shapes but also regarding tissue material properties. Anatomical structures, material properties, injury mechanisms and tolerances associated with children may change greatly due to age compared to those with adults. Consequently, there is a need for data specifically for children.

The main goal of this manuscript is to explore mechanics of pediatric trunk non-invasively using biomechanical approaches. To achieve this goal, the first chapter aims to present a literature review in the context of pediatric trunk biomechanics under loading and mechanical properties of pediatric rib cortical bones. After a brief anatomical description of the thorax and child growth, it details the studies on

biomechanical behavior of pediatric trunk through PMHS tests and *in vivo* loading tests. Then, the experiments on human ribs, including pediatric and adult ribs, are introduced to identify mechanical properties of human ribs. Finally, the studies exploring relationships between mechanical properties and bone densities are described to discuss the method which can be possibly used to study rib mechanical properties *in vivo*.

Based on the state of the art, some questions are raised:

- Pediatric trunk compliance has been previously assessed using force-deflection curves. However, such curves have been found different with each other. Do these differences come from the methods used or the population?
- Some studies have proved that bone mechanical properties are correlated to Bone Mineral Density (BMD). However, the relationships have not been studied on rib cortical bones. Do similar relationships between mechanical properties and BMD exist on human ribs?
- Can the relationships between mechanical properties and BMD be applied to child population, to estimate pediatric rib mechanical properties based on BMD measured *in vivo*?

To answer these questions, this manuscript focuses on the mechanical responses of pediatric trunk and tissue mechanical properties, and it is structured of the following parts:

- **Chapter 2** focuses on mechanical responses of pediatric trunk. The force-displacement characterizations of human trunk, both of children and adults, are observed. The different biomechanical behavior between them is discussed. Some assumptions are made to explain the different behaviors.
- **Chapter 3** deals with tissue mechanical properties. It aims to observe the relationships between adult rib cortical bone mechanical properties and BMD. Two different X-ray modalities are introduced to measure BMD, and results are compared. Since BMD of pediatric ribs can be measured *in vivo*, this chapter

opens the way to estimate mechanical properties of pediatric rib cortical bones *in vivo*.

- **Chapter 4** applies the mechanical property - BMD relationship to a child population. The mechanical properties of pediatric rib cortical bones are estimated based on the BMD measured *in vivo*. The rib mechanical properties along age are also presented.

Chapter 1 - State of the art

1.1 Introduction

Each year, more than 800 children under the age 15 are killed on European roads and 100 000 are injured (European-Commission, 2013). European Road Safety Observatory reported that more than 1 000 children under 14 years were killed on European roads every year between 2000 and 2010 (ERF, 2012). The French National Interministerial Observatory Road Safety reported that 115 children less than 14 years were killed on French roads in 2012, which is 3.2 % of the fatalities (ONISR, 2012). In the United States, motor vehicle crashes were the leading cause of death for children age 4 and every age 11 through 14 (NHTSA, 2013). During 2011, 1 140 children under 14 years were killed and accounted for 4 % of the traffic fatalities in the United States. An average of 3 children age 14 and younger were killed and 469 were injured every day in the United States in motor vehicle crashes during 2011 (NHTSA, 2013). In China, child road safety is also a serious public health issue. According to the annual report of the State Administration of Public Transportation Security, more than 3 000 children under 12 years old were killed in 2011, which is more than 5 % of the fatalities (MPSTA, 2013). Despite reductions in overall fatalities, the protection for children involved in traffic crashes is still a socio-economic problem.

According to Brown et al. 2006, the head, lower extremities and trunk (thorax and abdomen) are the main injured body regions for children under 18 years in case of a crash, as shown in Figure 1.1. Crandall et al., 2013 reported an overall AIS (Abbreviated Injury Scale) 2+ injury risk of approximately 10 % for children in CRS (Child Restraint Systems, 0 – 7 years) or seat belts (8 – 15 years). Approximately a total of 15 % child pedestrians with an AIS 3+ injury had an injury to the thorax and abdomen. In addition, the thorax and abdomen contain and protect the internal organs (such as heart, lungs, kidneys, spleen, liver), and the injuries of the organs could lead to fatality. Therefore, it is important to protect the thorax and abdomen during a crash.

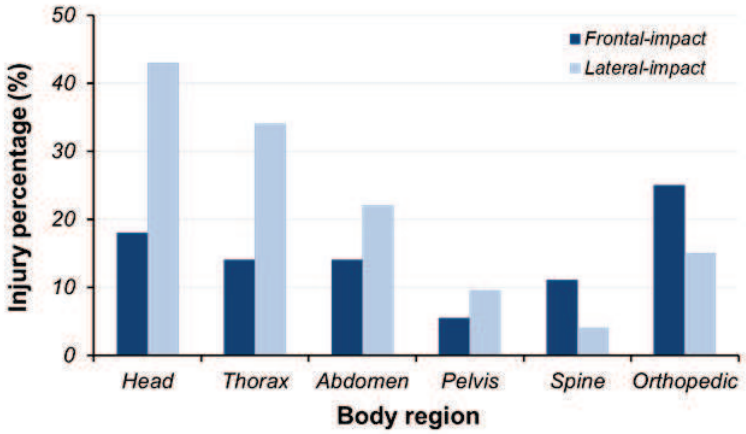

Figure 1.1: Percentage distribution of injury for children by body region (Brown et al., 2006).

From the data available in previous studies, it is obvious that better protection for children should be considered. Currently, Child Restraint Systems (CRS) have been developed to protect infants and young children involved in motor vehicle crashes. Adolescents are suggested to use the restraint systems which are designed for adults. There is a consensus that the risk of injuries could be reduced significantly with proper use of CRS. In the USA, child safety seats reduce the risk of fatal injury by 71 % for infants and 54 % for toddlers when installed and used correctly (Will et al., 2004). For the children between 4 and 11 years of age, booster seats can reduce the injury risk by 59 % compared to seat belt only (CDCP, 2006). However, the effectiveness of CRS still need to be improved, and tools to evaluate the effectiveness of CRS are poor (Beillas et al., 2012; Trosseille et al., 2001).

Initially, the effectiveness of CRS was estimated by studies of road accidents (Melvin et al., 1978). At present, pediatric Anthropomorphic Test Devices (ATDs) have been widely used in crash tests to guide the development and improvement of CRS, as well as in numerical simulations to observe the possible injuries of children during a crash (Brown et al., 2002; Kapoor et al., 2011). The most recent pediatric ATD crash test dummies are those of the Q sets, which follow the Hybrid III and P sets. Figure 1.2 shows the Q-dummy family (de Jager et al., 2005).

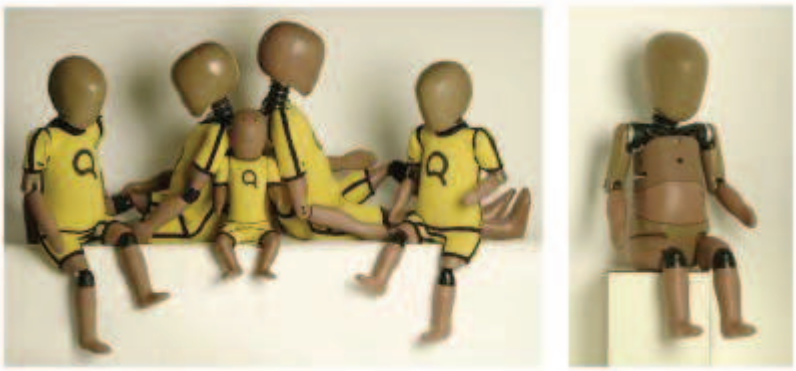

Figure 1.2: Q set child dummy family, from left to right: Q1.5, Q3, Q0, Q6, Q1 and Q1 without suit (de Jager et al., 2005).

However, there is limited data available on pediatric impact responses till now. As a result, pediatric ATDs and their corresponding Injury Assessment Reference Values (IARVs) are predominately based on scaled adult data. Unlike a human, ATD crash test dummies should be durable enough to withstand many impact tests, so they are commonly stiffer than a real human. In addition, ATD dummies have simple geometry to reproduce the complexity of human anatomy, and the injury risk of ATD dummies is estimated from implanted transducers and accelerometers, which could only measure the mechanical response at single points (Franklyn et al., 2007).

Computer models, as another type of human body surrogate, have been developed to avoid such limitations. They can provide more detailed biomechanical response than ATD dummies. Advanced Finite Element (FE) model could help to understand the impact response and the injury mechanisms, to improve the prediction and prevention of injury in traffic crashes. A number of pediatric computer models have been developed, either for specific body regions or whole-body models (Jiang et al., 2012; Mizuno et al., 2005; Roth et al., 2008). However, the data (both geometrical data and tissue mechanical properties) used to develop pediatric numerical models, are mainly scaled from adults, and the data used to validate the pediatric numerical models are also derived directly or indirectly from adults. Scaling techniques have not yet been proved to be accurate partly because of the lack of real pediatric data, so the bio-fidelity of the developed models needs to be improved (Franklyn et al., 2007). Figure 1.3 shows an example of a 3 years old child FE model obtained by scaling techniques.

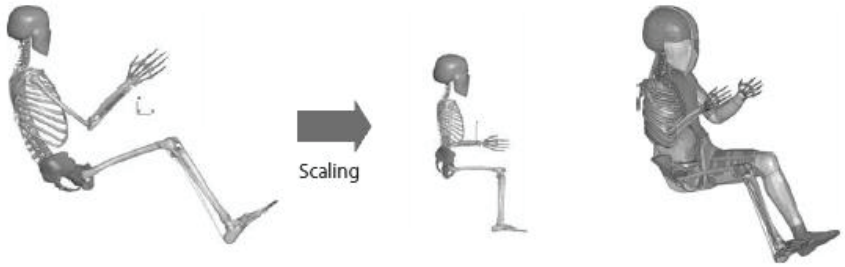

Figure 1.3: 3 years old child FE model obtained by scaling techniques (Mizuno et al., 2005).

Children differ from adults not only in anatomical structures or the proportion of body segments, but also in tissue properties. There is considerable variation in anatomical structures as well as tissue properties between infants, young children, adolescents and adults (Franklyn et al., 2007). Taking into account the growth effect is a great challenge for scaling techniques.

To develop biofidelic pediatric thorax models, geometrical data and material properties are required. The geometrical data can be directly obtained from medical images using biplanar X-rays (Benameur et al., 2005; Dansereau et al., 1988; Mitton et al., 2008) or Computed Tomography (CT) (Jiang et al., 2012; Sandoz et al., 2013a), while tissue properties are rare (Agnew et al., 2013b; Berteau et al., 2012; Pezowicz et al., 2012). In adult population, tissue properties as well as the biomechanical responses of thorax could be studied through a couple of methods, including cadaveric tissue tests and whole-body cadaveric impact tests. However, it is difficult and even impossible to perform such tests on pediatric cadavers in most of the countries. To our knowledge, only few experiments using pediatric cadavers have been reported (Kallieris et al., 1976; Kent et al., 2011; Kent et al., 2009; Ouyang et al., 2006). As an alternative, animal surrogates have been proposed to study pediatric trunk response (Kent et al., 2006; Kroell et al., 1981). However, animal surrogates have significant differences with children. The anatomical configuration, the organ positions and tissue properties are rather different. Also, age correction (the relationship between age and the stage of development) between children and animal surrogates is not well known (Franklin, 2007). Therefore, it is challenging to use the

data from animal surrogates tests. Considering these limitations, it is clear that a non-invasive method would be valuable for studies on pediatric population.

The main objectives of this study are to explore non-invasive methods to study: 1) the biomechanical responses of pediatric trunk under loading and 2) the material properties of pediatric rib cortical bone.

This chapter will present a state of the art. First, the anatomy of the thorax will be introduced briefly. Then, the studies on biomechanical responses of pediatric trunk under impact or low speed loading will be summarized. Finally, a review of the studies on material properties of pediatric rib cortical bones will be given out. Since there is limited pediatric data available for thorax, the studies on adults will also be included.

1.2 Anatomy

Human trunk is the central part of the body. The trunk includes the thorax and abdomen. The thorax is the upper part of the trunk between the neck and the abdomen. The abdomen constitutes the part of the body between the thorax and pelvis. The thorax is composed of the rib cage, muscles, skin and inner organs (e.g. lungs and heart). The diaphragm separates the thorax and abdomen. The abdomen contains the majority of the organs, such as liver, kidneys, spleen. However, the muscles, skin and internal organs are not the main concerns in this study and they will not be discussed. The anatomy of rib cage will be highlighted.

1.2.1 Rib cage

The rib cage is a bony and cartilaginous structure which surrounds the thoracic cavity, forming a core part of the human skeleton. It makes up the thoracic wall and provides support for the muscles of the neck, thorax, upper abdomen and back. A typical rib cage consists of 12 thoracic vertebrae, 12 pairs of ribs with costal cartilages, the sternum and the intercostal muscles.

Posteriorly, each rib is connected to the thoracic vertebrae of the spine. Anteriorly, the upper 7 pairs of ribs connect directly to the head of the sternum by means of costal cartilage and they are termed “true ribs”. The 8 - 10 pairs of ribs connect to the sternum via a cartilaginous attachment. Because of this indirectly connection, these ribs are termed “false ribs”. The 11 and 12 pairs of ribs do not attach to the sternum, and are termed “floating ribs” (Moore et al., 2013). Between the ribs lie the intercostal muscles. The intercostal muscles and the elasticity of costal cartilages allow movement when inhaling and exhaling. Figure 1.4 shows a typical human rib cage.

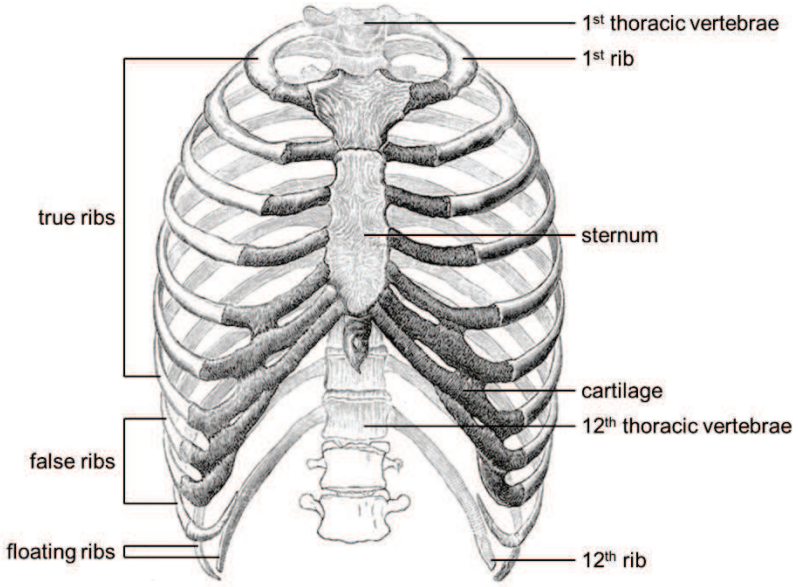

Figure 1.4: Rib cage anatomy (Gray, 1918).

1.2.1.1 Rib

The ribs, which continue anteriorly as costal cartilage, are described as long curved flat bone with two faces (internal and external) and two edges (inferior and superior). It consists of three parts. The posterior part consists of a head, a neck and a tubercle. The rib head typically has two facets; one for articulation with the corresponding vertebra, and another for articulation with the above vertebra. The rib tubercle is a prominence on the posterior surface which also articulates with the corresponding vertebra. The rib neck just simply connects the rib head with body. The middle part which is called the body or the shaft is the main part of the rib. It is thin and flat with two surfaces and two edges. The anterior or sternal extremity is flattened, and

presents a porous, oval, concave depression, into which the costal cartilage is received (Moore et al., 2013). Figure 1.5 shows a typical human rib.

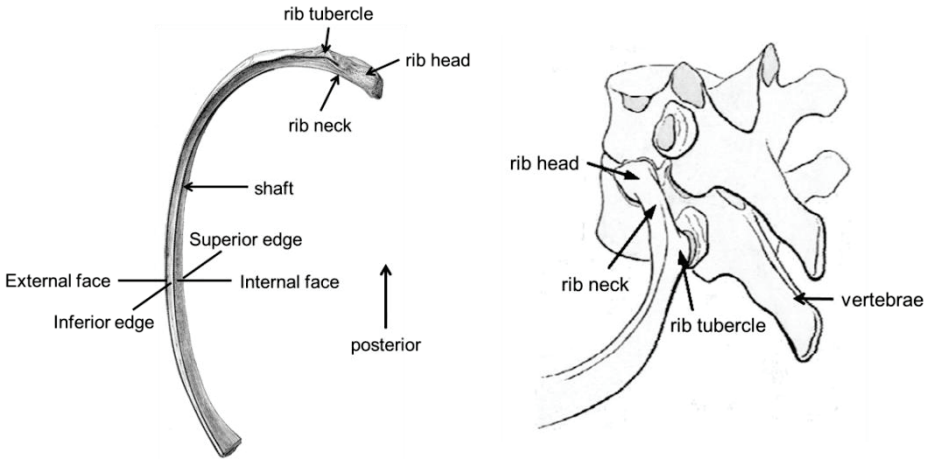

Figure 1.5: Left: a typical rib; right: a posterior-oblique view of the connection between rib and vertebrae (Gray, 1918).

Bone is a living, growing tissue. It is a porous mineralized structure, made up of cells, vessels, crystals of calcium compounds (hydroxyapatite), the proportion of which varies according to bone types and regions. The rib is made up of 2 types of bones: the cortical bone and the trabecular bone. Cortical bone forms the compact and thin outer layer of the rib while trabecular bone forms the soft porous internal structure. The distribution of cortical bone is non-uniform and the geometry of rib cross-section varies along the rib, as shown in Figure 1.6 (Mohr et al., 2007).

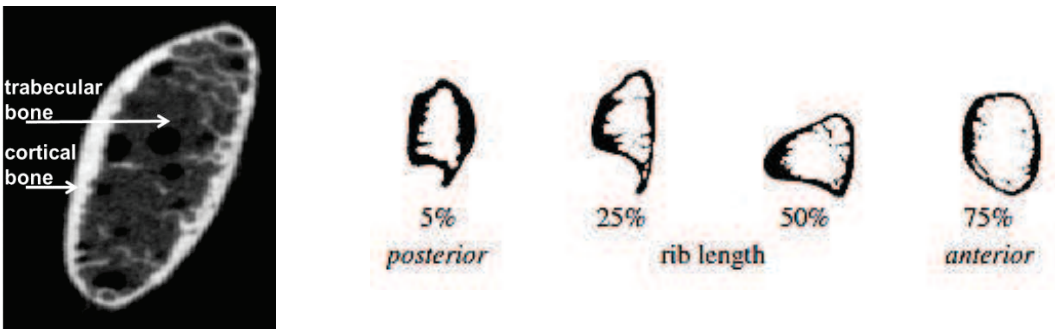

Figure 1.6: Left: cross section of a rib from a micro-computed tomography (µCT, Scanco XtremeCT, Switzerland) scan; right: the geometry of cross sections along the rib (%: percentage of rib length from posterior to anterior) (Mohr et al., 2007).

1.2.1.2 Costal cartilage

The costal cartilage is a hyaline cartilage junction between the rib and the sternum. It is only found at the anterior end of the rib. The first (from rib 1) 7 pairs of costal cartilages connect the ribs to sternum directly. Eight to ten pairs of costal cartilages are articulated with the lower border of the cartilage of the preceding rib, and join together to the sternum. At the lateral termini of the costal cartilage, it roughly has the same cross-section shape as its adjoining rib. The costal cartilage changes slightly along their length to the junction with the sternum (Gray, 1918).

The costal cartilages contribute to the elasticity of the chest wall. However, limited studies have investigated the material properties of the costal cartilages. Due to the difference in test methods, results also present an important variability (Forman, 2009; Lau et al., 2008; Yamada et al., 1970).

1.2.1.3 Vertebrae

Thoracic vertebrae compose the middle segment of the spine, between the cervical vertebrae and the lumbar vertebrae. Typically, humans have 12 thoracic vertebrae. Each vertebra is composed of a vertebral body, two transverse processes and a spinous process. Each thoracic vertebra is connected to a pair of ribs, one on either side of the rib cage, through articular facets on the transverse processes. The space between each vertebra contains an intervertebral disc that connects the vertebrae.

1.2.1.4 Sternum

The sternum is a long flat bony plate located anteriorly to the heart in the middle of the thorax. It connects to the ribs via cartilage, forming the anterior section of the rib cage. It helps to protect the inner organs and major blood vessels from physical trauma. The sternum is composed of highly vascular tissue, covered by a thin layer of cortical bone. It consists of three main regions: the manubrium, the body, and the xiphoid process.

1.2.2 Child growth and development

During growth, the body segments and also the proportions of body segments change significantly. The head of children is relatively large, the neck is short, the chest and abdomen is round and limbs are short. Also, the growth of the body segments is not linear and do not start at the same time. For instance, the growth rate of the lower limbs is faster than the upper torso, as a result, the gravity shifts from the thorax in infant to the pelvic area in adolescents (Beusenberg et al., 1993). Figure 1.7 illustrates the proportional changes in body segments during growth (Burdi et al., 1969). Figure 1.8 shows growth-patterns for various body segments (Beusenberg et al., 1993).

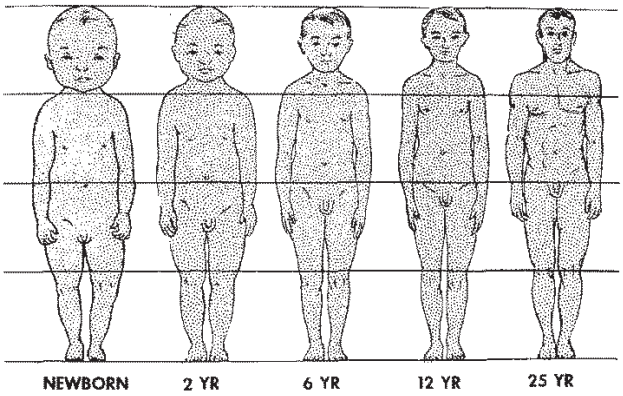

Figure 1.7: The proportional changes in body segments during growth (Burdi et al., 1969).

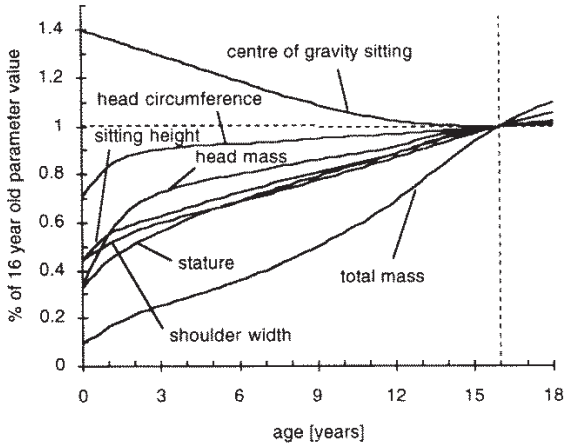

Figure 1.8: Body segments growth-patterns (Beusenberg et al., 1993).

During growth, the chest becomes flatter and wider gradually. The ribs in neonates are more horizontal than in adults (Hammer et al., 2005; Openshaw et al., 1984). Kent et al., 2005 also reported the changes of rib angle. Combining the studies on rib angle, it is assumed that human rib angle decreases before 18 years old and then increases with ageing. Besides the geometrical changes, ribs gradually ossify from their cartilaginous origins during growth. Therefore, the rib becomes more rigid and the proportion of the cartilages changes. It was reported that the ratio between cartilage length and whole rib length for rib 6 was approximately 45 % for 0.3- to 3-year old children while 33 % for 12- to 15-year old young adults (Sandoz et al., 2013a). As shown in Figure 1.9, the chest of a young adult is much wider than an infant. Also, less costal cartilages could be found at the anterior end of the ribs in the young adult. The ribs of infants and young children are relatively soft and flexible, enabling greater movement of compression than in adults; hence, fractures are less possible to occur for children but the possibility of compression on the inner organs increases (Stürtz, 1980).

The changes during growth may influence the biomechanical responses. A review of studies on pediatric trunk responses and tissue properties are essential. Thus, the following sections will mainly discuss: 1, the biomechanical responses of pediatric trunk under *ex vivo* and *in vivo* loadings; 2, the material properties of pediatric rib cortical bone. Since few pediatric bone properties are available, the material properties of adult cortical bone in ribs and other anatomic sites will be included.

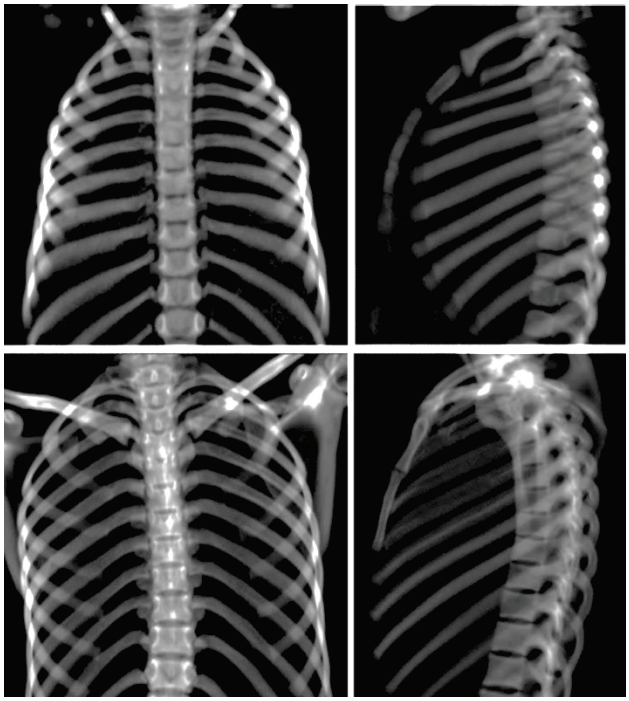

Figure 1.9: Front view and lateral view of pediatric chests, derived from 3-dimensional (3D) reconstruction of CT slices (SliceX, Arts et Métiers ParisTech). Top: a chest of a 15-month-old girl; Bottom: a chest of a 16-year-old girl.

1.3 Biomechanics of pediatric trunk under loading

Injury occurs when an impacting object transfers the impact energy to a biologic system. Understanding the biomechanical responses under loading is the first step for injury protection. Human trunk is viscoelastic, so the trunk biomechanical responses differ for low-speed and high-speed loadings. Numerous tests with different configurations have been conducted on adult PMHS to assess the responses of trunk (Lobdell et al., 1973; Nahum et al., 1975; Verzin et al., 2009). However, it is difficult to obtain pediatric PMHS subjects. Indeed, four pediatric PMHS tests have been reported so far in the literature (Kallieris et al., 1976; Kent et al., 2011; Kent et al., 2009; Ouyang et al., 2006). This section will provide an overview of existing experiments exploring biomechanical responses of pediatric trunk under *ex vivo* and *in vivo* loadings.

1.3.1 Pediatric Post Mortem Human Subject (PMHS) tests

The first study on pediatric cadavers was performed by Kallieris et al., 1976, as shown in Figure 1.10. They dynamically loaded the abdominal region of 4 pediatric cadavers aged from 2.5 years to 11 years and the tests were conducted within 16 - 120 hours after the death of the subjects. Pediatric cadavers were restrained with a 50 mm wide lap belt during a frontal impact at a speed of 8.3 m/s and 11.1 m/s. The deceleration ranged from 176.4 m/s^2 to 205.8 m/s^2. Slight injuries such as muscular hemorrhages and ligaments injuries were found in this study.

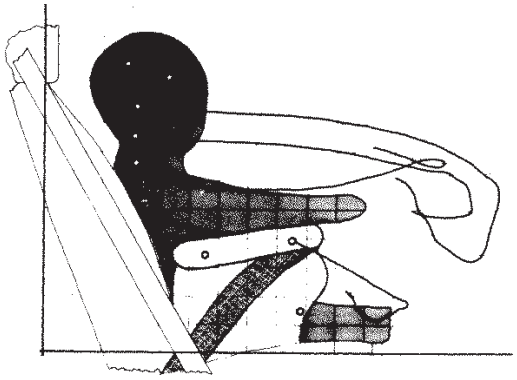

Figure 1.10: Pediatric PMHS tests a frontal impact (Kallieris et al., 1976).

The second study was performed by Ouyang et al., 2006, as shown in Figure 1.11. Nine pediatric cadavers were divided into two groups: the younger group (aged from 2 – 4 years, 4 subjects) and the older group (aged from 5 – 12 years, 5 subjects), and were subjected to frontal impact on the whole thoracic region. Cadavers from younger group were impacted with an impactor weighing 2.5 kg and 5 cm in diameter, while the older group impacted with an impactor weighing 3.5 kg and 7.5 cm in diameter. The velocity of the impactor ranged from 5.9 to 6.5 m/s. Injuries were found in 7 cadavers after the impact, and they suggest that energy to maximum deformation is the best predictor for injury. Force - thorax deformation relationships were also generated for the two age groups.

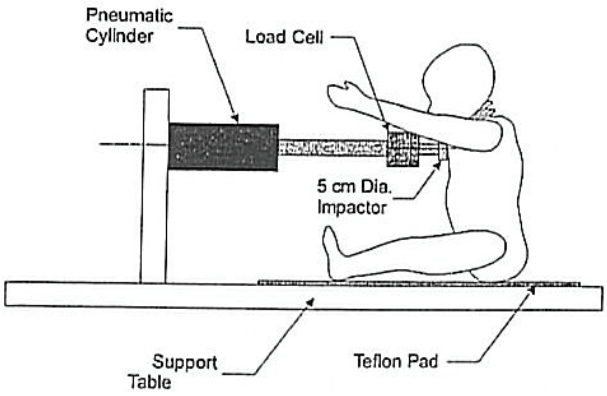

Figure 1.11: Thoracic impact on child PMHS (Ouyang et al., 2006).

The other two studies were performed by Kent et al., 2009 and 2011. In the study of Kent et al., 2009, a 7 years old female cadaver was sequentially tested for thoracic and abdominal compressions in 5 different loading configurations, as shown in Figure 1.12. The aim of the study was to guide the scaling of existing adult thoracic response data for application to the child and to assess the validity of a porcine abdominal model. The force – thorax deformation behavior of the pediatric chest when subjected to non-impact, dynamic loading from a diagonal belt and a distributed loading surface was quantified. They also discussed the relationship between the stiffness value of the thorax and the age, and suggested that the stiffness value increased in the fourth decade of life and then decreased, resulting in an approximate stiffness value of children and elderly adults.

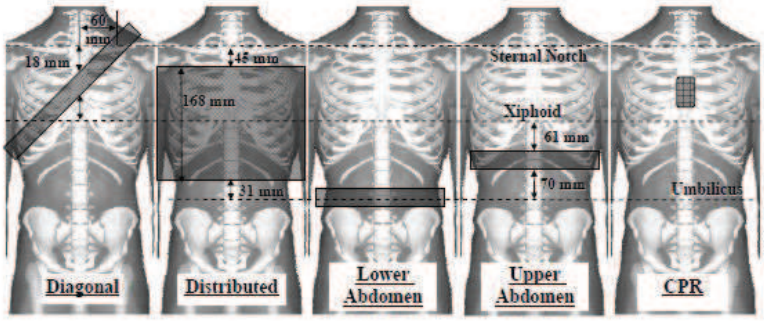

Figure 1.12: Pediatric PMHS tests in 5 different loading configurations (Kent et al., 2009).

Table 1.1: Studies on biomechanical responses of pediatric thorax and abdomen with pediatric PMHS

	No.	Age (year)	Statue (cm)	Weight (kg)	Region	Loading patterns	Loading speed	Maximun force (N)	Deceleration (g)	Deformation (mm)	Sternum VC* (m/s)
Kallieris et al., 1976	4	2.5 - 11	97 - 139	16 - 31	abdomen	lap-belt	30 and 40 km/h	1600 - 3800	18-21		
Ouyang et al., 2006	4	2 - 4	85 - 97	10.5 - 13.5	thorax	blunt impact	5.9 - 6.0 m/s	740 -825	63.9 - 124.8	44.8 - 57.7	1.5 - 2.7
	5	5 - 12	101 - 142	13 - 29	thorax	blunt impact	5.9 - 6.5 m/s	900 - 1560	35.6 - 91.7	31.5 - 72.3	0.7 - 4.5
Kent et al., 2009	1	7	119	26.8	abdomen	belt	2.2 - 2.3 m/s	1655 - 5352		33 - 39	
					thorax	belt	2.2 - 2.8 m/s	906 - 5941		31 - 57	
					thorax	distributed		2068 - 6657		26 - 31	
Kent et al., 2011	3	6 - 15	119 - 170	24 - 50	thorax and abdomen	belt		607 - 6968		21.7 - 54.6	

* VC: the viscous criterion (Kroell et al., 1986; Viano et al., 1988).

To expand the database reports by Kent et al., 2009, two additional pediatric cadavers aged 6 and 15 years were tested in Kent et al., 2011. The same test protocol was employed. In general, the two additional PMHS did not change the conclusions drawn by Kent et al., 2009. The 6 years old subject showed a similar thoracic and abdominal response to the 7 years old subject in Kent et al., 2009, but the 15 years old subject showed a slightly stiffer thoracic response.

The main information and results of the four studies on pediatric cadavers are summarized in Table 1.1.

1.3.2 Animal surrogates tests

Since pediatric cadavers are hard to collect. Animal models, particularly porcine models, have been introduced as a surrogate because they have a similar anatomy to human and could be placed in a similar manner to a human in tests. Although animals have their specific development stages in their lifetime, which are different to children, some studies have proposed a correction between human and pigs as shown in Table 1.2 (Franklin, 2007).

Table 1.2: Developmental correction between human and pigs (Franklin, 2007)

Stage of life	Human	Pig
Weaned	6 - 12 months	6 weeks
Childhood	10 years	6 months
Physically mature	18 years	1.5 years
Middle age	40 years	4 years
Elderly	70 years	5 years
Lifespan	80 years	6 years

Pigs have been proposed to benchmark the abdominal response of children since 1980s (Kroell et al., 1981). Arbogast et al., 2005 and Kent et al., 2006 performed studies to determine a proper porcine model that best correlated with a 6 years old child, specifically for the abdomen. It was suggested that the mechanical response of the 6 years old pediatric abdomen could be obtained approximately by using a porcine model with 77 days of age and 21.4 kg of mass (Arbogast et al., 2005). The quasi-

static response of that pig compared well to children with belt loading on lower abdomen. In the study of Kent et al., 2006, series experiments including 18 quasi-static and 47 dynamic tests were performed on 47 juvenile swine (Figure 1.13). They suggested that the porcine abdomen structural characterization found in the study could be used in the development of both mechanical and computational pediatric abdominal models.

Though animal models can give a behavior close to children which could not be obtained by other means, there are still a number of significant differences between children and pigs, such as the positions of the internal organs and the shapes of the rib cage. Tissue properties and mechanical responses to impacts obtained from animal tests are not easy to correlate with children, and the correlation is also hard to validate.

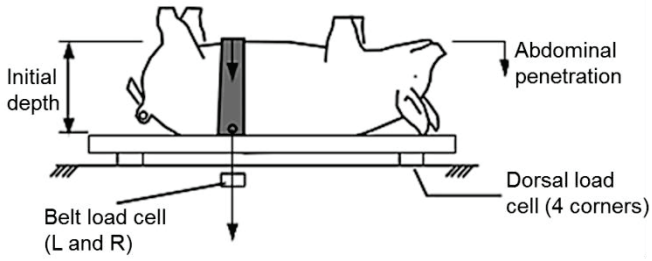

Figure 1.13: Lap belt penetration on an porcine model (Kent et al., 2006).

1.3.3 *In vivo* loading tests

1.3.3.1 Cardiopulmonary resuscitation (CPR)

Since pediatric PMHS is hard to collect for impact tests and animal surrogate tests have obvious limitations, another method has been developed to study mechanical responses of human thorax. A series of studies obtained the force and displacement relationships of adult thorax by Cardiopulmonary Resuscitation (CPR) (Arbogast et al., 2006; Halperin et al., 2002). Then this method was applied to pediatric subjects to quantify their thoracic response under loading (Maltese et al., 2008). During cardiopulmonary resuscitation in clinical environment, Maltese et al. 2008 measured force – thorax deflection characteristics for 18 cardiac arrest subjects aged from 8 to 22 years old. They reported an average maximum chest deflection of 39 mm

corresponding to a force of 309 N. Some other parameters such as linear stiffness of the chest were also reported. Compared with the study of Arbogast et al., 2006 on adult subjects, they suggested that the stiffness of human thorax increased from youth to middle age and then decreases in the elderly. However, the age range of the subjects in Maltese et al., 2008 were not so wide, and the sample size also needed to be expanded.

The chest compressions performed during CPR were under emergency condition, so the different mattresses under the patients affected the deflection measurements. Nishisaki et al. 2009 suggested that deflection of the mattress contributed approximately 28 % of measured chest compression depth on ICU beds and 10% of measured chest compression depth on stretchers with back boards in place. They performed CPR events on 12 patients aged from 8 to 22 years old. The measured mean chest depth during CPR was 47 ± 8 mm on ICU beds, and 45 ± 7 mm on stretcher beds with overestimation of 13 ± 4 mm and 4 ± 1 mm respectively.

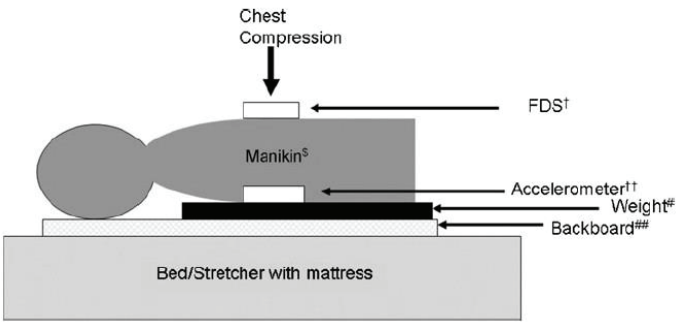

Figure 1.14: Description of CPR reconstruction (FDS: force and deflection monitor) (Nishisaki et al., 2009).

Niles et al. 2012 also performed chest compressions on 35 subjects during CPR. Subjects were divided into two groups according to the age: a younger group with 16 pediatric subjects aged from 8.1 to 14.9 years and an older group with 19 subjects aged from 15 to 24 years. By correcting the effect of mattresses, they reported the maximum chest deflection of 36.2 mm with corresponding force of 307 N for the younger group and 36.8 mm with corresponding force of 336 N for the older. The

mean chest compression actual depth and force were not significantly different in these two different age groups (Niles et al., 2012).

Kent et al., 2009 also performed CPR on a pediatric PMHS subject. The CPR tests on a 7 year old PMHS subject showed a maximum chest deflection of 11 mm to 14 mm with corresponding force of 50 N to 150 N. They also reported the force – chest deflection curve as shown in Figure 1.15.

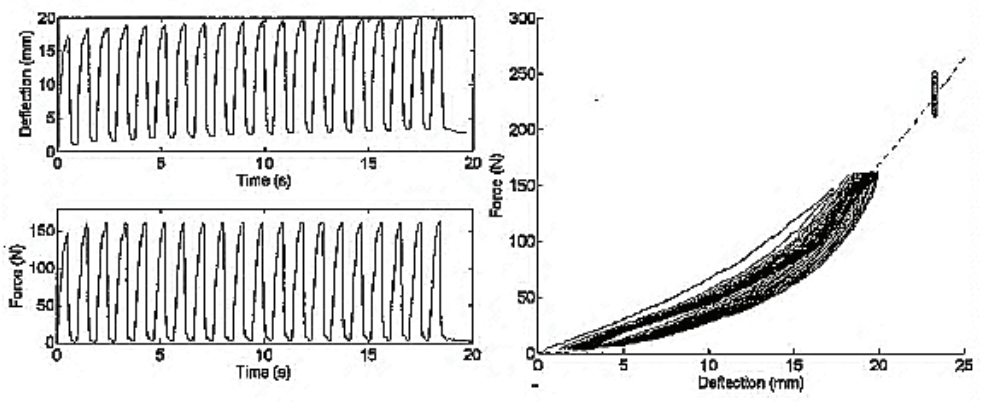

Figure 1.15: Chest compressions on a 7 years old PMHS subject during CPR. Left: force and deflection along time; Right: force – chest deflection curves (Kent et al., 2009).

From the studies with CPR method, it is possible to study biomechanical responses of pediatric thorax under loading in clinical environment. However, some limitations of the CPR method should be pointed out. First, the subjects in the previous studies were in cardiac arrest or PMHS, thus, the effects of breathing and muscle tension were not considered. Second, the subjects participating in CPR measurements in the previous studies were not so young (older than eight years), thus, the age range of the subjects should be expanded and younger children should be considered. Considering these limitations, a new method should be developed to study the biomechanical responses under loading on living children.

1.3.3.2 Chest Physiotherapy

Chest physiotherapy treatment is a clinical method which is now widely used for newborn babies suffering from respiratory disease. Chest physiotherapy treatment

improves bronchial pulmonary exchanges, in order to clear the lungs and to help the patients to breath, as shown in Figure 1.16 (Perrotta et al., 2005; Roque i Figuls et al., 2012). Chest physiotherapy treatment gives the possibility to study the force – deflection characteristics of living and active pediatric chest in a clinical environment.

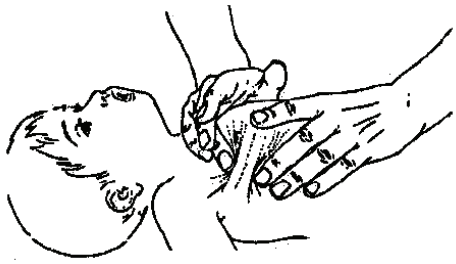

Figure 1.16: Chest physiotherapy treatment on children (Marechal et al., 2007).

Sandoz et al. 2011 quantified the mechanical response of the infant and toddler trunk under loading during physiotherapy treatments with 26 children aged from 45 days to 7 years. They reported the average maximum chest deflection of 22 mm with average maximum force of 240 N. The force-deflection relationships were also presented as shown in Figure 1.17. Furthermore, they reported the peculiarity of the *in vivo* child's trunk mechanical behaviour: the increase in force always occurred before the increase in displacement. Compared with the force-displacement characteristics from pediatric PMHS by CPR method as shown in Figure 1.15, the peculiar characteristics of the living and active pediatric trunk seems different. The reasons were not discussed in detail in Sandoz et al. 2011. So there remains a question: do such differences come from the methods used and/or population? Thus, it is interesting in a further study to quantify and explain the force-displacement characteristics of living and active pediatric trunk during respiratory physiotherapy.

The main studies on pediatric trunk responses under low-speed loading conditions are summarized in Table 1.3.

This section provides an overview of studies exploring biomechanical responses of pediatric thorax and abdomen under impact or low-speed loading conditions. Force – chest deflection characteristics could be useful for developing and validating pediatric models. For example, Jiang et al., 2012 developed a 10 years old pediatric thoracic

model and validated against the force – chest deflection characteristics obtained from CPR method. However, previous studies showed different force – chest deflection characteristics on cardiac arrest children and living children. Tissue property may play an important role in the different responses under loading. Moreover, it is important to understand how tissue properties change with age since children undergo significant changes during growth. Thus, the next section will focus on pediatric tissue properties, and rib cortical bone is the main concern.

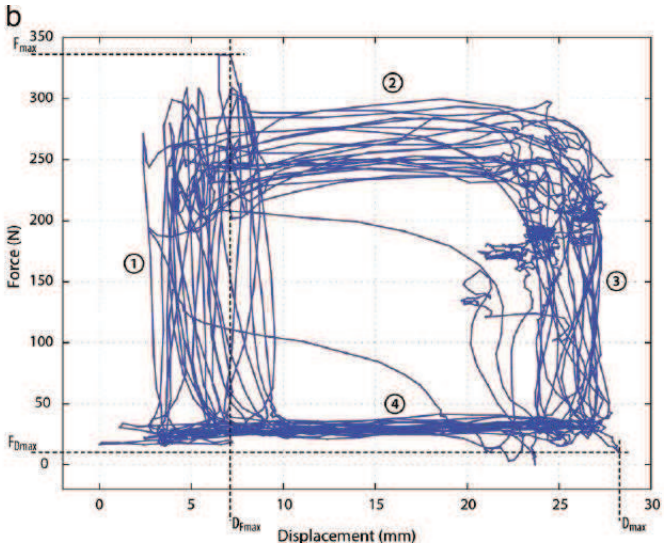

Figure 1.17: Force-deflection relationships of infant and toddler trunk under loading during physiotherapy treatments (Sandoz et al., 2011).

Table 1.3: The main studies on pediatric trunk responses *in vivo*

Studies	Subjects	No.	Age (year)	Region	Loading patterns	Maximum speed (m/s)	Maximum force (N)	Maximum deformation (mm)
Maltese et al., 2008	cardiac arrest	18	8 - 22	thorax	CPR	0.22	309	39
Nishisaki et al., 2009	cardiac arrest	12	8 - 22	thorax	CPR			41
Niles et al., 2012	cardiac arrest	16	8 - 15	thorax	CPR		307	36
		19	15 - 24	thorax	CPR		336	37
Kent et al., 2009	PMHS	1	7	thorax	CPR		50 - 150	11 -14
Sandoz et al., 2011	living and active	26	0 - 7	thorax abdomen	Chest physiotherapy	0.2	240	22

1.4 Mechanical properties of human bones

While studies on adult bone properties are common, few studies can be found on pediatric bones till now (Franklyn et al., 2007). The main reason is that pediatric materials for tests are difficult to obtain. Thus, a non-invasive method to study pediatric material properties could overcome this limitation. In this section, tests on human ribs exploring rib material properties will be discussed. Then, an overview of studies on relationships between human bones properties and their densities will be summarized in order to propose a non-invasive method to study pediatric rib cortical bone properties.

1.4.1 Material properties of human rib cortical bone

It is generally accepted that human cortical bone is anisotropic and viscoelastic (Dempster et al., 1952; Lakes et al., 1979; Reilly et al., 1974). In human ribs, it was found in a numerical study that the changes of trabecular bone properties has negligible influence on rib responses compared to cortical bone (Li et al., 2010). Thus, rib cortical bone is the main concern in this study. Various tests have been performed with adult rib sections or small samples under different protocols, resulting in various results. This section will give a brief overview of studies exploring pediatric and adult rib cortical bone properties.

1.4.1.1 Pediatric rib cortical bone properties

Compared to the studies on adult ribs, studies on pediatrics ribs are rare. Berteau et al., 2012 determined the material properties (Young's modulus and Poisson's ratio in transversal direction) of the ribs through UltraSonic (US) measurements. Twelve rib segments were harvested from two female subjects aged 15 and 17 years. The mean Young's modulus (E) was determined as 14.1 and 15.4 GPa for the two subjects, respectively.

After a first study on pediatric ribs (Pfefferle et al., 2007), a second detailed study (Agnew et al., 2013b) was reported by the same group. In the second study, 44 rib sections were collected from 12 subjects aged from 5 months to 9 years old. Three-

point bending tests with a loading rate of 0.042 mm/s were performed on the rib specimens, as shown in Figure 1.18. They reported a mean Young's modulus of 4.9 GPa with a mean ultimate stress of 87.4 MPa. However, Agnew et al., 2013b suggested that stature may be more appropriate than age for questions regarding material properties of growing bones.

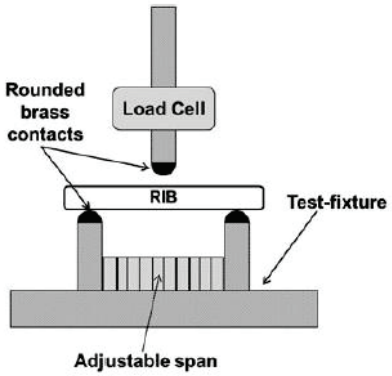

Figure 1.18: Three-point bending tests on pediatric ribs (Agnew et al., 2013b).

A relationship between Young's modulus and age is drawn in Figure 1.19. The different protocols in these two studies should be highlighted since different protocols may have influence the properties measurements. An overall relationship for the two studies under different protocols is challenging. However, Figure 1.19 suggests an increasing trend of the Young's modulus (E) through age for pediatric rib cortical bones.

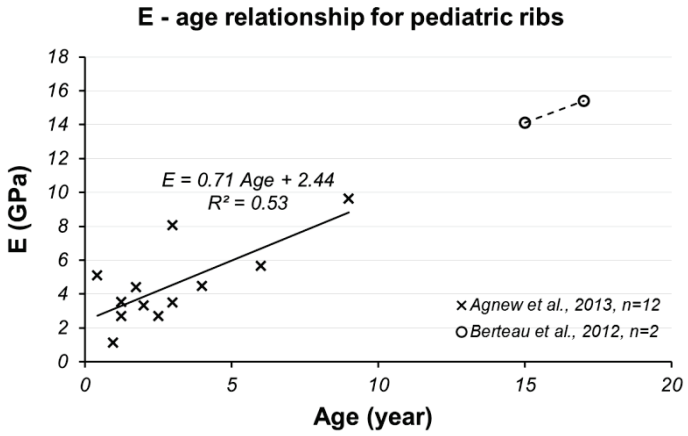

Figure 1.19: Young's modulus (E) – age relationship for pediatric ribs, derived from Berteau et al., 2012 and Agnew et al., 2013b.

1.4.1.2 Adult rib cortical bone properties

A number of studies have performed three-point bending tests on adult rib sections or rib coupons to investigate the properties (Charpail et al., 2005; Cormier et al., 2005; Granik et al., 1973; Mitton et al., 2014; Stitzel et al., 2003; Subit et al., 2013; Yoganandan et al., 1998).

Granik et al., 1973 performed three-point bending tests on 10 rib specimens from 6th and 7th ribs. They reported an average Young's modulus of 11.5 GPa and an average failure stress of 106.2 MPa. However, the age of the specimens was not clear and the number of the specimens is too small to draw a conclusion on the age effect for the material properties.

Yoganandan et al., 1998 also performed quasi-static three-point bending tests on 120 rib specimens from 30 cadavers aged from 29 to 81 years. Rib sections with a length of 150 mm were collected from 7th and 8th ribs. Results did not show significant difference of properties between the two rib levels. The average Young's modulus was 2.3 GPa and 1.9 GPa for the 7th and 8th ribs respectively. The average peak force was 153 N and 137 N for the 7th and 8th ribs respectively. The age effect on material properties was not discussed in the study.

Stitzel et al., 2003 presented a study of dynamic three-point bending tests on 92 small rib cortical bone coupons from anterior, lateral, and posterior locations of the rib cages of four cadavers. Results indicated that material properties varied significantly with respect to region. The Young's modulus and ultimate stress in the lateral portion (11.9 GPa, 153.5 MPa) of the ribs are significantly larger than those in the anterior (7.5 GPa, 116.7 MPa) and posterior (10.7 GPa, 127.7 MPa) locations. In addition, the stiffness, the ultimate stress and the ultimate strain for all subjects generally increased with the rib level.

Cormier et al., 2005 conducted dynamic three-point bending tests on 56 rib sections from anterior, lateral, and posterior locations of the rib cages of four cadavers. They showed a significant variation of peak moment by thoracic region. The average values of the peak moment were reported of 2, 2.9 and 3.9 Nm for the anterior, lateral and

posterior portion, respectively. They also reported significant differences in cross-sectional geometry with respect to rib level. However, they did not report the Young's modulus.

However, three-point bending tests have inherent limitation that introduces uncertainty in calculating material properties. Linear elastic beam theory assumptions are used in calculation, which results in an overestimation of ultimate stress. It was reported that linear elastic beam equations over-predicted the ultimate tensile stress by a factor of 1.56 for square cross-sections, and by a factor of 2.1 for circular cross-sections (Burstein et al., 1972). It was also reported that calculating material properties based on deflection data from whole bone three-point bending under-predicted the elastic modulus and ultimate strain by approximately 40 % (Funk et al., 2004). Therefore, some other studies performed tensile tests on isolated cortical bone coupons to measure material properties of human rib cortical bones (Kemper et al., 2005; Kemper et al., 2007; Subit et al., 2013).

Kemper et al., 2005 investigated the tensile material properties of 117 rib cortical bone coupons from 6 cadavers aged from 18 to 67 years. In contrast to the findings of Stitzel et al., 2003, they reported that there were no significant differences in material properties of human rib cortical bones according to thoracic region or rib level. The overall average Young's modulus was 13.9 GPa, and ultimate stress was 124.2 MPa. Considering in conjunction with the previous studies, they suggested that the material properties of cortical bone remained constant within an individual thorax while the geometry of each rib changed, which resulted in variations in the strength of the whole rib.

To determine which variables contribute to regional variations in the strength of human ribs, Kemper et al., 2007 conduct 94 matched tests on human rib specimens, including 46 tension coupon tests and 48 whole rib three-point bending tests. The results of the tension coupon tests showed that there were no significant differences in material properties with respect to region or rib level. In contrast, significant differences in material properties were found in three-point bending tests. They suggested that variations existed in the structural response of human ribs with respect

to region and rib level, which were due to the changes in local geometry of each rib. However, material properties of rib cortical bones remained constant within an individual thorax, but significant variation could exist between individuals due to the effects of age and gender.

A more recent study on adult rib cortical bones was performed by Subit et al., 2013. 10 rib coupons were harvested from the cortical shell of the 6th and 7th left ribs from three cadavers. The coupons were tested to fracture under quasi-static (0.01 mm/s and 0.02 mm/s) and dynamic (24 mm/s) loading. Fracture however did not always occur in the smallest cross-sectional areas, which indicated the anisotropic and nonhomogeneous nature of human rib cortical bones. Young's modulus ranged from 11.4 to 18.5 GPa, failure stress from 83.4 to 143.9 MPa and failure strain from 0.71 to 1.49 % in quasi-static tests. Failure stress ranged from 94.7 to 155.9 MPa in dynamic tests. The average Young's modulus was reported of 13.5 GPa for quasi-static tests and the failure stresses were 112 MPa for quasi-static tests and 124.6 MPa for dynamic tests, respectively. The main results of the studies were summarized in Table 1.4. The test configurations were summarized in Table 1.5.

Table 1.4: Main results of published tests on human rib cortical bones

	Element	Test type	E (GPa)	σ_{max} (MPa)
Granik et al., 1973	Section	three-point bending	11.5	106.2
Yoganandan et al., 1998	Section	three-point bending	2.3 (7th rib) 1.9 (8th rib)	NA NA
Stitzel et al., 2003	Coupon	three-point bending	7.5 (anterior) 11.9 (lateral) 10.7 (posterior)	116.7 (anterior) 153.5 (lateral) 127.7 (posterior)
Kemper et al., 2005	Coupon	tension	13.9	124.2
Kemper et al., 2007	Coupon	tension	14.4	130.9
	Section	three-point bending	18.9 (anterior) 21.1 (lateral)	128.8 (anterior) 176.2 (lateral)
Subit et al., 2013	Coupon	tension	13.5 NA	112.1 124.6
Mitton et al., 2014	Section	three-point bending	8.4	74.0

* E: Young's modulus; σ_{max}: ultimate stress (failure stress); NA: not available.

Table 1.5: Configurations of published tests on human rib cortical bone

	Number of subjects	Age range (year)	Mean Age (year)	Number of specimens	Element	Rib level	Test type	Loading rate (mm/s)
Granik et al., 1973	10	NA	NA	NA	Section	6 & 7	three-point bending	NA
Yoganandan et al., 1998	30	29 - 81	64	120	Section	7 & 8	three-point bending	0.042
Stitzel et al., 2003	4	61 - 71	65	92	Coupon	1 - 12	three-point bending	356
Cormier et al., 2005	4	61 - 71	65	52	Section	2 - 12	three-point bending	500 - 1000
Kemper et al., 2005	6	18 - 67	50	117	Coupon	1 - 12	tension	
Kemper et al., 2007	6	42 - 81	60	46	Coupon	4 - 7	tension	
				48	Section	4 - 7	three-point bending	172
Subit et al., 2013	3	54 - 71	64	10	Coupon	6 & 7	tension	0.01 and 0.02
					Coupon	7		24

* NA: not available.

Previous studies on adult ribs showed various results of properties. The variations may due to different test configurations. On the whole, tension tests on rib coupons showed relative stable properties, but results are affected by loading rates. On the contrary, three-point bending tests showed results in a wide range. Results could be different due to test samples (coupon or whole rib), loading rate, rib level and region of the rib. All the studies illustrated that human rib cortical bone is anisotropic and heterogeneous. Regarding age effect, previous studies did not give a clear answer on how properties change along the age. As an attempt, Figure 1.20 and Figure 1.21 show relationships between human rib cortical bone properties and age. It should be pointed out that test configurations are different, and it is rather challenging to draw a conclusion of the whole based on tests under different configurations.

In conclusion, material properties of human rib cortical bones showed variations due to different test conditions. For child population, biomechanical tests are not easy to conduct. A non-invasive method should be considered for studies on child population.

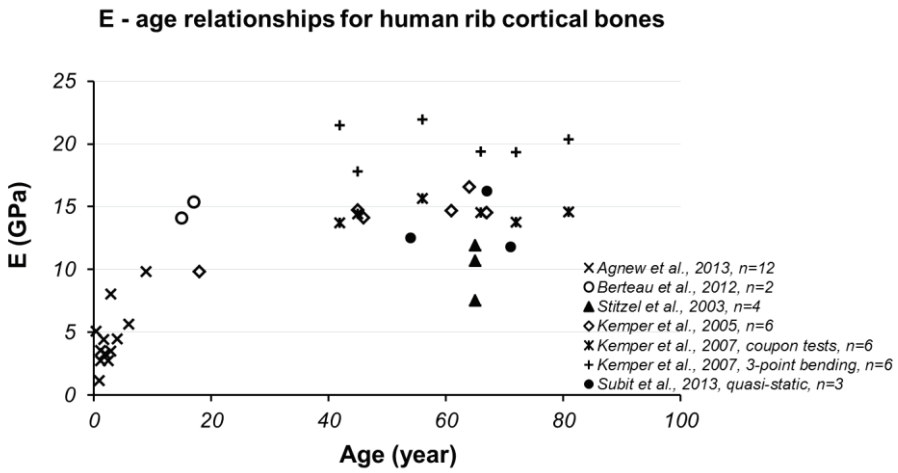

Figure 1.20: Young's modulus (E) – age relationships for human rib cortical bones, derived from previous studies.

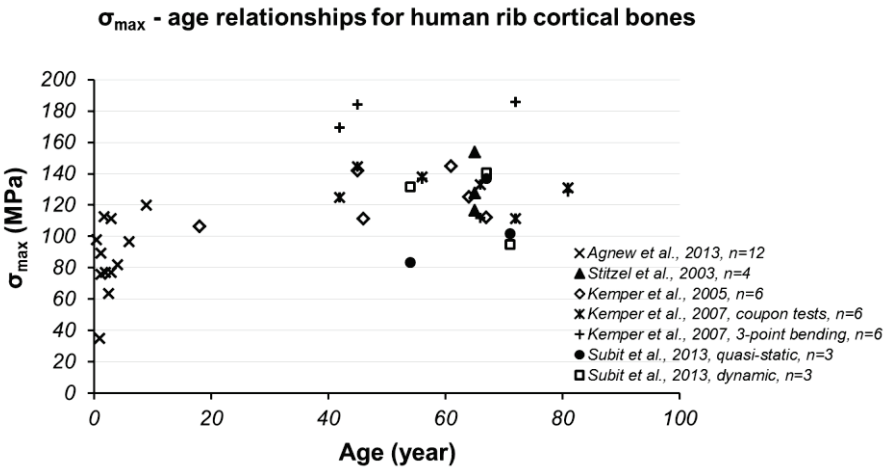

Figure 1.21: Ultimate stress (σ_{max}) – age relationships for human rib cortical bones, derived from previous studies.

1.4.2 Relationships between bone material properties and its densities

Previous studies have reported that bone material properties, especially stiffness (Young's modulus) and strength (ultimate stress), are related to bone densities including ash density, apparent density (wet or dry, which is weight per unit volume) and BMD measured by Quantitative Computed Tomography (QCT). The studies on relationships between bone mechanical behavior and its compositions (apparent bone density or ash density) could go back early to 1950s (Vose et al., 1959). After the invention of CT technology in 1970s, CT technology has been used to study bone mechanical properties using a mathematical relationship between CT density and bone mechanical properties. Some studies found the relationships between mechanical properties, ash density, apparent density and QCT density on human trabecular bones (Hvid et al., 1989). The main goals of the previous studies were to derive empirical properties-density relationships. However, the proposed relationships are different from one to another. A review on such studies is necessary. Figure 1.22 lists some studies focusing on relationships between cortical bone mechanical properties and the densities.

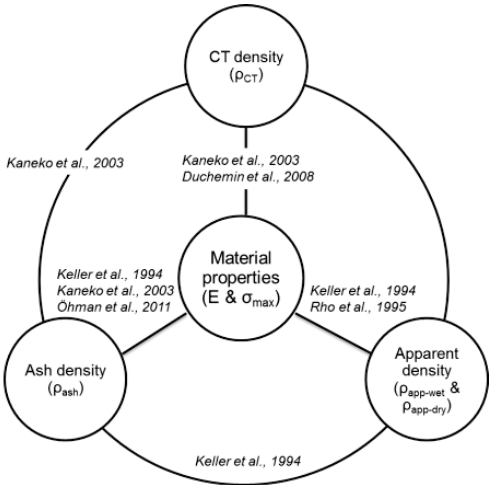

Figure 1.22: Relationships between cortical bone mechanical properties (E: Young's modulus, σ_{max}: ultimate stress) and ash density (ρ_{ash}), apparent density (wet: $\rho_{app-wet}$ and dry: $\rho_{app-dry}$) and CT density (ρ_{CT}).

Keller, 1994 corrected the compressive mechanical properties of both trabecular and cortical bones to ash density and apparent dry density. They harvested 496 cube specimens from five male donors, including 199 vertebral bones (donor's age: 70, 77 and 84 years) and 297 femoral bones (donor's age: 46 and 67 years). A strong linear relationship was found between ash density and apparent dry density ($r^2 > 0.97$). Linear and power models were used to describe the relationships between compressive mechanical properties (E_c and σ_{max-c}) and the densities (ρ_{ash} and $\rho_{app-dry}$). It was found that ash density could better describe the mechanical properties of trabecular and cortical bones expressed as a power function. The power functions were described as Equations (1-1) and (1-2).

$$E_c = 10.5\ \rho_{ash}^{2.75}\ (r^2 = 0.97) \qquad (1\text{-}1)$$

$$\sigma_{max\text{-}c} = 117\ \rho_{ash}^{1.93}\ (r^2 = 0.97) \qquad (1\text{-}2)$$

Rho et al., 1995 used ultrasonic transmission technique to determine mechanical properties of cortical and trabecular bones from eight donors. Apparent wet density ($\rho_{app-wet}$) of the cortical bones was determined by Archimedes' principle and showed strong relationships to elastic modulus (E). The densities and E for trabecular bones correlated stronger than cortical bones. It indicated that apparent wet density better

predicted the elastic modulus of trabecular bones than cortical bones. The densities - E relationships for cortical bones were defined as Equation (1-3).

$$E = 0.014\ \rho_{app\text{-}wet} - 6.142\ (r^2 = 0.77) \quad (1\text{-}3)$$

Kaneko et al., 2003 performed 80 tensile and compressive tests with cube-shaped cortical specimens collected from femoral diaphysis of nine cadavers (age range: 53 – 78 years). They identified relationships between QCT density, ash density and the tensile and compressive mechanical properties of the femoral cortical bones. Strong linear relationships were found between QCT density (ρ_{QCT}), ash density (ρ_{ash}) and mechanical properties ($0.73 < r < 0.93$, $p < 0.05$). Linear relationship between QCT density and ash density (in mg/cm^3) was described as Equation (1-4). Linear relationships between QCT density and mechanical properties were described as Equations (1-5) and (1-6).

$$\rho_{ash} = 0.831\rho_{QCT} + 127\ (r^2 = 0.88,\ p < 0.001) \quad (1\text{-}4)$$

$$E_t = 0.02\rho_{QCT} - 4.4\ (r^2 = 0.77),\ E_c = 0.02\rho_{QCT} - 4.3\ (r^2 = 0.77) \quad (1\text{-}5)$$

$$\sigma_{max\text{-}t} = 0.09\rho_{QCT} - 18.4\ (r^2 = 0.74),\ \sigma_{max\text{-}c} = 0.15\rho_{QCT} - 46.1\ (r^2 = 0.83) \quad (1\text{-}6)$$

Duchemin et al., 2008 also performed 46 tensile and 46 compressive tests with femoral cortical bone samples from 13 donors aged from 54 to 101 years. Densities of the bone samples were measured by QCT and were found to be linearly corrected to Young's modulus and ultimate strength ($0.43 < r^2 < 0.72$, $p < 0.001$). The relationships were described as Equations (1-7) and (1-8).

$$E_t = 0.012\rho_{QCT} + 0.26\ (r^2 = 0.51),\ E_c = 0.009\rho_{QCT} + 1.30\ (r^2 = 0.43) \quad (1\text{-}7)$$

$$\sigma_{max\text{-}t} = 0.064\rho_{QCT} - 21.82\ (r^2 = 0.57),\ \sigma_{max\text{-}c} = 0.097\rho_{QCT} - 5.95\ (r^2 = 0.72) \quad (1\text{-}8)$$

Recently, Öhman et al. , 2011 collected femoral and tibial cortical bones from 12 children (age range: 4 – 15 years) and 12 adults (age range: 22 – 61 years). Compression tests were performed on 107 cortical bone specimens. Ash density (ρ_{ash}) was found to be a good predictor of compressive elastic modulus (E_c) and ultimate compressive stress ($\sigma_{max\text{-}c}$) for both children and adults. It was found that mechanical

properties of pediatric cortical bone were different from that of adult tissue. However, relationships between ash density and mechanical properties of children and adults share the same regression curve, as shown in Figure 1.23. This seems to demonstrate that the correlations found for adult bones could be extended to pediatric bone tissues. The relationships between ash density and mechanical properties were described with the following equations (1-9) and (1.10).

$$E_c = 12.9\ \rho_{ash}^{2.0}\ (r^2 = 0.86) \quad (1\text{-}9)$$

$$\sigma_{max\text{-}c} = 144.7\ \rho_{ash}^{2.0}\ (r^2 = 0.91) \quad (1\text{-}10)$$

Existing studies clearly indicated that human bone densities are correlated to mechanical properties. Figure 1.23 illustrated the relationships between Young's modulus and QCT densities (ρ_{QCT}) for the above studies. Compared to apparent density and ash density, CT density could be assessed in a clinical environment. As a non-invasive method, QCT technique could be employed to study bone mechanical properties with a large population. For trabecular bones, QCT density has been also proved to be a good predictor of bone mechanical properties (Kopperdahl et al., 2002). However, trabecular bones are not the main concern in this study. To the author's knowledge, there is no study exploring relationships between mechanical properties and densities for human rib cortical bones. Could the relationships found in femoral or tibial cortical bones be extended to ribs? Moreover, the study by Öhman et al., 2011 showed that children shared the same relationships found in adults. Would the same relationships for children and adults be found for ribs? Since tests on pediatric subjects or tissues are hard to perform, QCT density provides an interesting opportunity to assess pediatric rib mechanical properties *in vivo*.

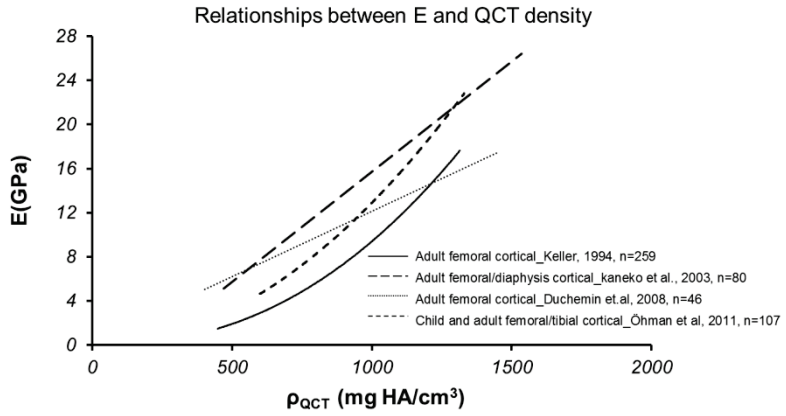

Figure 1.23: Relationships between Young's modulus (E) and QCT densities (ρ_{QCT}) (the data of Öhman et al., 2011 are derived from a combinition of Öhman et al., 2011 and Kaneko et al., 2003).

1.5 Conclusions and specific aims

This chapter firstly highlighted the importance of protection for children in vehicle traffic crashes. In case of a crash, trunk is one of the main injured body segments, and this thesis will focus on pediatric trunk. To build up or validate a pediatric model, the main difficulties are related to pediatric data. Only small amount of biomechanical data on children could be found in the literature. A better knowledge of pediatric trunk, including mechanical response and tissue properties is expected.

The second part in this chapter introduced the specific anatomical characteristics of children. There are considerable variations of anatomy and tissue properties for children during growth. To develop a pediatric model with high bio-fidelity, essential anatomical data and mechanical properties are critical. However, existing pediatric data are mainly based on scaling from adults. Scaling technique, which is a widely used method on pediatric modeling, has certain limitations.

Unlike adults, pediatric data can hardly be acquired directly from tests on cadavers or cadaveric tissues. To overcome this limitation, *in vivo* methods are expected for studies on children. Some methods which could be used to study biomechanical responses of children in clinical environments were proposed.

Trunk compliance was previously assessed using force-deflection curves. However, such curves have been found different with each other. Do these differences come from the methods used? To answer this question, the first goal of this thesis is to explore the force-deflection characteristics of pediatric trunk under loading *in vivo*.

For a better understanding of the mechanical responses of pediatric trunk, tissue property is also an important concern. Since trabecular bone properties has negligible influence on rib responses compared to cortical bone (Li et al., 2010), rib cortical bone is the main issue in this thesis. Very few studies on material properties (Young's modulus and maximal strength) of the pediatric rib cortical bone could be found in literature. Thus, non-invasive methods are valuable to study rib cortical bone mechanical properties of children.

Some studies have proved that bone mechanical properties are correlated to BMD, which can be measured by QCT non-invasively. However, this method has not been applied to ribs. Are there similar relationships between mechanical properties and bone mineral density (assessed by QCT) on human ribs? Can this method be used for a child population? This thesis will bring answers to these questions.

In brief, the following chapters will be:

Chapter 2, Mechanical behavior of the *in vivo* pediatric and adult trunk during respiratory physiotherapy. Some adult subjects will also be introduced to illustrate the different mechanical responses between children and adults.

Chapter 3, Mechanical properties of adult ribs, to explore relationships between mechanical properties and BMD of adult rib cortical bones based on X-ray modalities.

Chapter 4, Mechanical properties of pediatric ribs, to estimate the mechanical properties of pediatric rib cortical bones *in vivo*.

A flow chart illustrating the major components of this thesis is shown in Figure 1.24.

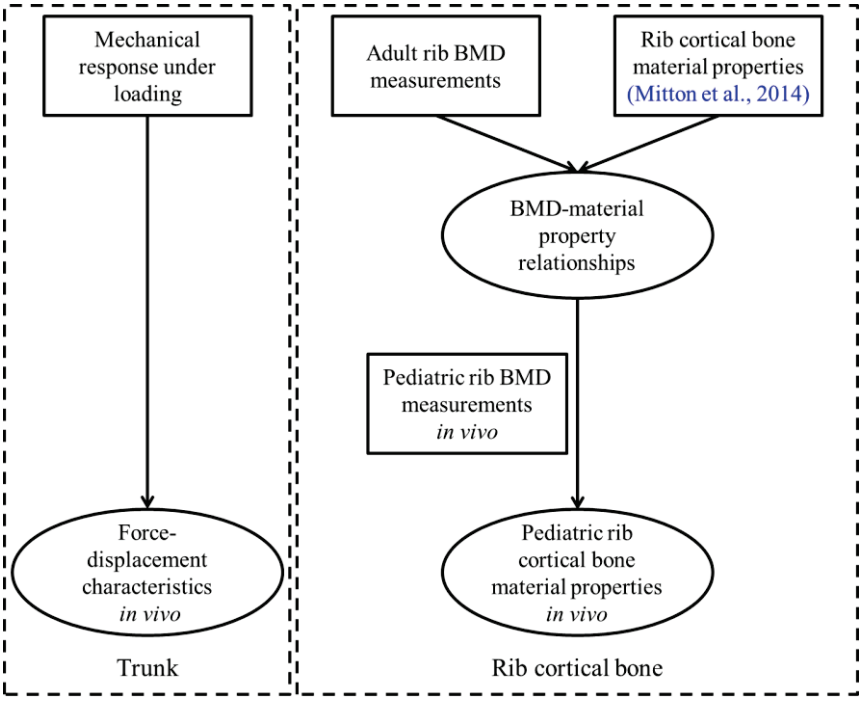

Figure 1.24: Flow chart of the thesis.

Chapter 2 - *In vivo* mechanical behavior of the pediatric and adult trunk during respiratory physiotherapy

This chapter will mainly discuss *in vivo* mechanical behavior of pediatric and adult trunk during respiratory physiotherapy. The data have been collected in a previous project for the children (Sandoz et al., 2011) and unpublished data on adults. The main contribution of current PhD work was the analysis of the data and the writing of a paper (Zhu et al., 2014).

2.1 Introduction

The pediatric and adult trunk mechanical response has been previously studied through experiments conducted on Post-mortem Human Subjects (PMHS). However, only a few studies of pediatric PMHS tests exist in the literature (Kallieris et al., 1976; Kent et al., 2011; Kent et al., 2009; Ouyang et al., 2006). In order to measure the mechanical response of a child's trunk in a clinical environment, researchers have proposed alternative methods in the past few years (Arbogast et al., 2009; Bermond et al., 2006; Maltese et al., 2008; Niles et al., 2012; Sandoz et al., 2011). Maltese et al., 2008 reported the force-deflection properties of 18 cardiac arrest pediatric patients aged from 8 to 22 years during cardiopulmonary resuscitation (CPR) (Maltese et al., 2008). They acquired data using force and acceleration sensors interposed between the hands of the person administering CPR and the sternum of the patient. Maltese et al., 2008 combined their results with the studies of Arbogast et al., 2006 and Kent et al., 2004 and suggested that the stiffness of the human thorax increases from youth to middle age and then decreases with aging. Although CPR technology affords a unique opportunity to access the force-deflection characteristics of living human subjects, the investigated living human subjects are cardiac arrest; therefore, the effects of muscle contraction and respiration of the patient were not considered.

Today, respiratory physiotherapy is widely used on new-borns suffering from minor respiratory disease such as bronchiolitis (Perrotta et al., 2005; Roque i Figuls et al., 2012). Sandoz et al., 2011 studied the *in vivo* child's trunk response under dynamic loading during respiratory physiotherapy with 26 active pediatric subjects aged from 45 days to 7 years. They reported the peculiarity of the *in vivo* child's trunk mechanical behavior: the increase in force always occurred before the increase in displacement. The peculiar force-displacement characteristics of the active pediatric trunk differ from results of other studies, but the reasons were not discussed in detail. Do these differences come from the methods used and/or the population (i.e. children and adults)? In order to explore this question, the objective of this study was to quantify and explain the force-displacement characteristics of the living and active pediatric and adult trunk during respiratory physiotherapy.

2.2 Methods

2.2.1 Population

Eight pediatric patients aged from 5 months to 15 months took part in this study. All the pediatric patients suffered from bronchiolitis and were in the recovery stage. Chest respiratory physiotherapy was used to speed their recovery. No rib or abdominal disease was diagnosed. The children's parents were informed of the anonymous measurements and invited to participate in this study. Eight healthy adult volunteers aged from 30 years to 87 years participated. The participating adults were also informed of the anonymous recordings and treated in the same manner. This study was approved by the ethical committee of IFSTTAR (Institut Français des Sciences et Technologies des Transports, de l'Aménagement et des Réseaux).

2.2.2 Manipulation method of chest respiratory physiotherapy

Chest respiratory physiotherapy is a medical treatment widely used with pediatric patients suffering from bronchiolitis to help them clear tracheobronchial secretions. Sandoz et al., 2011 studied chest respiratory physiotherapy to measure the *in vivo*

child's trunk mechanical response by assessing the mechanical parameters calculated from the displacement of the child's trunk and the loading force applied by the physiotherapist. The current study follows and improves the measurement protocol described in Sandoz et al., 2011 and focuses on children and adults. The *in vivo* mechanical behavior of pediatric and adult trunk is described in this study.

Sandoz et al., 2011 described in detail the manipulation method of chest respiratory physiotherapy. All measurements were performed in the office of a physiotherapist - specialized in respiratory physiotherapy - who performed all manipulations. During the manipulations, the pediatric patients and adult volunteers lay on a manipulation table in a supine position. The physiotherapist always put his left hand on the thorax in the middle of the sternum and his right hand on the abdomen. The physiotherapist performed multiple compressions on the trunk of both children and adults. A force plate (Bertec© FP4060-10, Colombus, USA) was embedded in the manipulation table to record the force applied by the back of the subjects to the manipulation table at 1000 HZ. Seven reflective targets were temporarily glued to the back of the physiotherapist's hands. Some of the seven targets were occasionally hidden by arms or legs. Only three visible targets (per hand) throughout the recording were selected for study. Two synchronized digital cameras filmed the manipulation at 90 fps. The two-dimensional (2D) coordinates of each selected target were obtained by using an automatic tracing software (MotionTrack, Vannier Photelec©, Antony, France). The 3D displacement and geometric centroid of each traced target were then calculated using a calibration object and "Direct Linear Transformation" (DLT) algorithm (Abdel-Aziz et al., 1971). At the end of each manipulation, the recorded video and the measured force were synchronized using an electroluminescent contact sensor. Figure 2.1 shows the two cameras' views of the manipulation.

Figure 2.1: The cameras' views of the manipulation. Top: pediatric patients. Bottom: adult volunteers.

2.2.3 The measured and calculated parameters

The force plate recorded the force applied by the physiotherapist. As the force plate recorded the force applied simultaneously to the chest and the abdomen, the displacement of the centroid of the six traced targets was considered to be the displacement of the whole trunk. Since the studied subjects were living and even active during the manipulation, the period when the force-displacement curves showed several consecutive regular cycles was considered for the analysis and parameters were calculated on that basis. No less than five consecutive regular cycles for each of the subjects were obtained in this study. The measured and calculated parameters for these cycles are listed in Table 2.1.

Table 2.1: Measured and calculated parameters of children and adults

Parameter	Descriptions
Age	The age of the pediatric and adult subjects
Gender	The gender of the pediatric and adult subjects
Thoracic circumference	Measure at the center of the sternum
E	Anteroposterior thickness of the trunk, measured as the highest vertical position of the centroid of the targets minus the thickness of the physiotherapist's hands (25 mm)
F_{max}	The maximum vertical force measured by the force-plate
D_{max}	The maximum anteroposterior (vertical) displacement of the trunk, the zero deflection is the point of maximum E
C_{max}	The maximum vertical normalized displacement, computed as the ratio of the maximum displacement and the maximum anteroposterior thickness of the trunk, $C_{max}=D_{max}/E$
V_{max}	The maximum vertical loading speed, calculated from the temporal derivation of the anteroposterior displacement
D_{Fmax}	The displacement when the maximum load occurred
C_{Fmax}	The normalized displacement when the maximum load occurred, $C_{Fmax}=D_{Fmax}/E$
F_{Dmax}	The load when the maximum displacement occurred
VC	The viscous criterion (Kroell et al., 1986; Viano et al., 1988). VC=V*C. The maximum V_{Cmax} value was reported
Time lag ratio	The time lag divided by the duration time of the manipulation cycle

2.2.4 Accuracy assessment

According to the manufacturer's accuracy statement, the relative error of the measurement in the vertical direction of the force plate is 0.2 %. The accuracy of the 3D reconstruction algorithm is satisfactory with a 1 mm average position error (Sandoz et al., 2011). In addition, the system deformation which can be attributed to the deformation of the physiotherapist's hands, the deformation of the mattress on the manipulation table and the deformation of the table itself, was estimated by loadings without patients, with hands directly placed on a wood board whose dimensions were 300 mm × 400 mm. Results showed that the system vertical deformation was about 2 mm at maximum.

2.2.5 Statistics

The data were divided into two groups: children group and adults group. The XLStat software (Version 2013.1.01, Addinsoft) was used for the statistical analysis. The Wilcoxon rank-sum test showed no significant difference for the parameters by gender in either group ($p > 0.05$). Therefore, no distribution between males and females will be made.

2.3 Results

Figure 2.2 illustrates an example of the synchronized force and displacement curves along time. The curves show the consistency of the force applied by the physiotherapist. During the manipulation, pediatric patients were always much more active than adult volunteers. To better control the pediatric patients and to achieve a better therapeutic effect, the physiotherapist sometimes loaded to the maximum force immediately then held the child's trunk and released the force a bit. In contrast, the physiotherapist applied smooth force on the adult trunk. Note that a time lag between the force time histories and displacement time histories was found in both children and adults. A larger time lag was observed in children. The time lag ratio of children was always around 5 % to 25 %, and it was larger than that of adult volunteers, which was always less than 5 %.

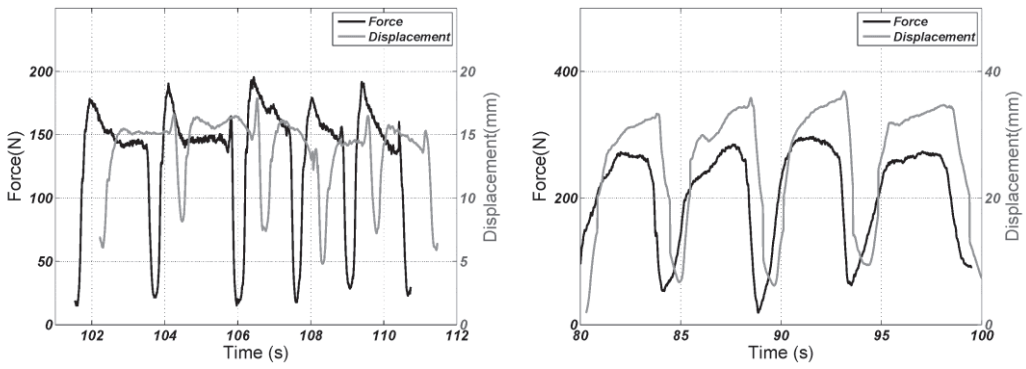

Figure 2.2: Force and displacement curves along time. Left: 5-month-old boy. Right: 67-year-old female. The displacement includes system deformation.

Three typical shapes of force-displacement curves were observed in this study, as shown in Figure 2.3. These different shapes illustrate the peculiar *in vivo* behavior of living subjects. The differing shapes were related to the time lags/time lag ratios. Shapes I and II were mainly observed in adult volunteers, who have smaller time lags/time lag ratios, while shape III was mainly observed in pediatric patients. Note that shapes I and II were found to coexist in some adult volunteers, while shapes II and III coexisted in some pediatric patients.

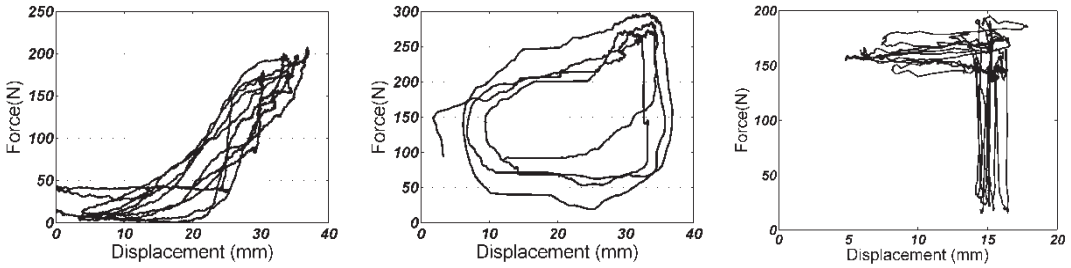

Shape I Shape II Shape III

Figure 2.3: Different shapes of force-displacement curves. Left: 37-year-old female. Middle: 67-year-old female. Right: 5-month-old boy. The displacement includes system deformation.

To further understand the relationship between time lag and the corresponding shape of the force-displacement curve, a simulation was performed with a pediatric subject. Initially, the displacement time histories lagged about 0.5 s behind the force time histories. In the simulation, the force time histories were fixed while the displacement time histories were shifted gradually with a time step of 0.1 s to reduce the time lag. The shape of the force-displacement curves changed with the reduction in time lag, as shown in Figure 2.4.

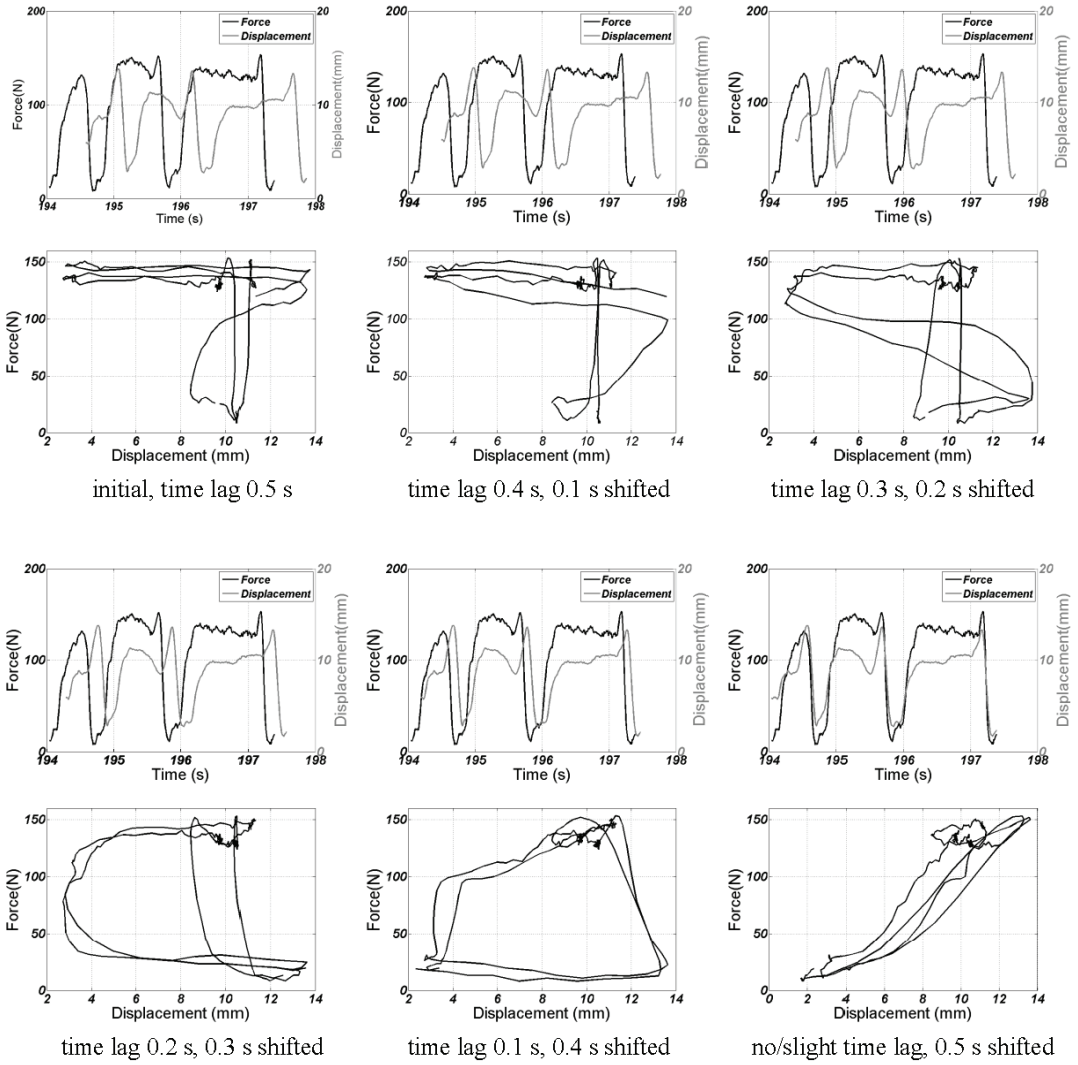

Figure 2.4: Different time lags and the corresponding force-displacement curves. Simulated from the initial data of a 7-month-old boy.

The way in which the physiotherapist applied force can influence the displacement response, as shown in Figure 2.5. Despite the non-modification of the usual practice of the physiotherapist on pediatric patients, some modifications were made on adult volunteers. The physiotherapist changed the loading pattern on a 30-year-old adult. Rapid loading (loading cycle 1 in Figure 2.5) could result in Shape II of force-displacement curves while gradual loading (loading cycle 2 in Figure 2.5) resulted in Shape I of force-displacement curves.

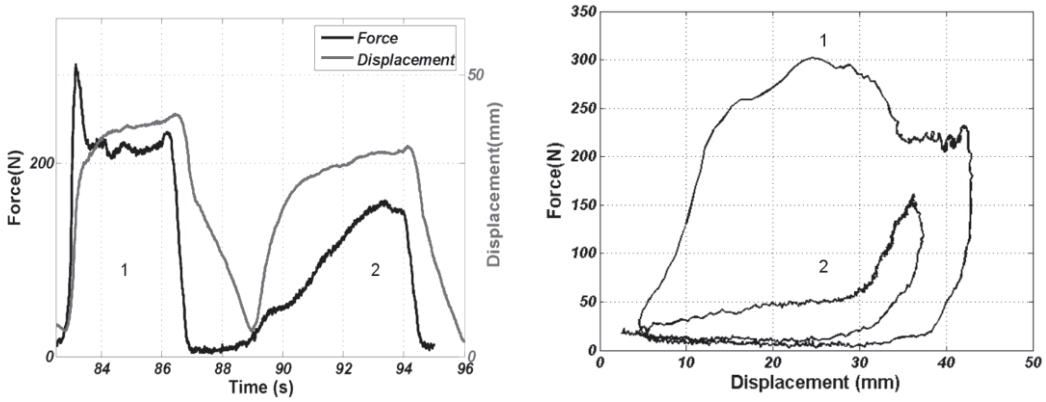

Figure 2.5: Different load patterns in a 30-year-old adult volunteer. Left: force and displacement curves along time. Right: force-displacement curves.

All the measured and calculated parameters are summarized and sorted by patient age in Table 2.2. The descriptions of the parameters could be found in Table 1.3. The upper part shows the parameters of the children group and the bottom half shows the adults group. As expected, the E of the adults is larger than that of children. The mean value of D_{max} of the adults group reaches 44 mm, which is more than twice that of the children group (18 mm), but C_{max} of the two groups is similar (24 % for adults group and 23 % for children group). F_{max} of the adult volunteers is 250 N, a little larger than 208 N on pediatric patients. V_{max} is relatively stable for the children group with a mean value of 0.25 m/s while the mean value of the adults group is 0.44 m/s. The mean V_{Cmax} of both the children and adults group is far smaller than 1000 mm/s, which was the tolerance level proposed by Viano et al., 1988 for chest impact in adults. Due to the peculiar shapes of the force-displacement curves, the maximum displacement did not necessarily occur at the point of maximum load. Therefore, the parameters D_{Fmax}, F_{Dmax} and C_{Fmax} are listed here but without comparison between the two groups.

Table 2.2 Results of the measured and calculated parameters, the displacement includes system deformation.

Patient No.	Child(C) /Adult(A)	Gender	Age (month)	Thoracic Circumference (cm)	E (mm)	D_{max} (mm)	C_{max}	F_{max} (N)	V_{max} (m/s)	D_{Fmax} (mm)	C_{Fmax} (mm)	F_{Dmax} (N)	VC_{max} (mm/s)	Force-displacement Curve Shape*
1	C	M	5	46	66	15	0.22	180	0.11	12	0.18	142	15.5	III
2	C	M	5	46.5	80	19	0.23	215	0.27	12	0.15	128	43.3	III
3	C	M	5.5	48	73	17	0.24	217	0.53	1	0.01	155	34.2	II & III
4	C	M	7	46	74	17	0.23	187	0.26	11	0.15	163	25.9	III
5	C	M	7.5	46	70	18	0.26	219	0.22	3	0.04	124	31.0	II & III
6	C	F	9.5	53	74	18	0.24	242	0.29	14	0.19	73	46.0	II & III
7	C	F	10	54	89	25	0.29	219	0.17	20	0.22	43	23.5	II
8	C	M	15	49	71	13	0.18	187	0.13	1	0.02	92	11.5	III
	Mean		8.1	49	75	18	0.24	208	0.25	9	0.12	115	28.8	
	Min		5	46	66	13	0.18	180	0.11	1	0.01	43	11.5	
	Max		15	54	89	25	0.29	242	0.53	20	0.22	163	46.0	
	SD		3.4	3	7	4	0.03	22	0.13	7	0.08	42	12.3	
Patient No.	**Child(C) /Adult(A)**	**Gender**	**Age (year)**	**Thoracic Circumference (cm)**	**E (mm)**	**D_{max} (mm)**	**C_{max}**	**F_{max} (N)**	**V_{max} (m/s)**	**D_{Fmax} (mm)**	**C_{Fmax} (mm)**	**F_{Dmax} (N)**	**VC_{max} (mm/s)**	**Force-displacement Curve Shape***
1	A	M	30	103	191	52	0.27	302	0.81	25	0.13	188	161.1	I & II
2	A	F	37	82	148	36	0.24	203	0.14	27	0.18	80	14.2	II
3	A	F	37	86	145	37	0.25	207	0.12	37	0.25	199	6.9	I
4	A	M	48	99	174	37	0.21	188	0.18	37	0.21	185	16.7	I & II
5	A	M	66	107	251	55	0.22	292	0.64	15	0.06	9	81.5	II
6	A	F	67	87	191	39	0.20	346	0.60	23	0.12	259	65.6	II
7	A	F	68	103	210	37	0.17	185	0.13	32	0.15	158	14.9	II & III
8	A	F	87	102	236	58	0.25	276	0.91	45	0.19	145	89.3	I & II
	Mean		55	96	193	44	0.23	250	0.44	30	0.16	153	56.3	
	Min		30	82	145	36	0.17	185	0.12	15	0.06	9	6.9	
	Max		87	107	251	58	0.27	346	0.91	45	0.25	259	161.1	
	SD		19.9	10	38	9	0.03	62	0.33	10	0.06	77	53.8	

* I: Shape I; II: Shape II; III: Shape III

2.4 Discussion

This study measured and compared the force-displacement characteristics of the active pediatric and adult trunk during respiratory physiotherapy in a clinical environment. Chest respiratory physiotherapy is a common therapeutic method used to provide care for pediatric patients suffering from bronchiolitis (Demont et al., 2007; Marechal et al., 2007). The manipulations offered the opportunity to study the *in vivo* mechanical behavior of the pediatric trunk. Furthermore, respiratory physiotherapy was also applied to adult volunteers in this study. The physiotherapist applied regular force to the trunk during the manipulations without emergency or stress and the manipulations did not result in pain, injury or fracture.

The current study is somewhat similar to studies conducted by Arbogast et al., 2006 and Maltese et al., 2008. They also evaluated the force-displacement characteristics of the adult and young child chest but during CPR in a hospital emergency setting. Thus, some significant differences exist between these two previous studies and the current study. First, the loading areas are different. The CPR method applies force only on the sternum, whereas respiratory physiotherapy applies distributed force on the chest and abdomen via the physiotherapist's hands. Thus, findings obtained by applying the CPR method may be specific to sternal loading conditions. Second, the duration time of each operating cycle differs. Cardio-pulmonary resuscitation is conducted in emergency conditions, while respiratory physiotherapy is a regular therapeutic method. Each cycle of CPR has a compression and releasing stage and the cycle duration is usually less than 0.5 s. In this study, to better facilitate the expectoration of secretions in pediatric patients, the physiotherapist usually maintained compression at the end of the loading phase before releasing. In the current study, the cycle duration of pediatric patients and adult volunteers is around 2 s and 4 s, respectively. Finally, the involved subjects are different. Respiratory physiotherapy is used much more frequently on new-borns and infants; therefore, the involved pediatric patients are very young. In Maltese et al., 2008's study, the involved subjects were children older than 8 years and young adults. Of more importance, the involved children and adults in the current study were all living and active. The force-displacement characteristics

of the trunk were illustrated with real living and active subjects. On the contrary, subjects who underwent cardio-pulmonary resuscitation are with a cardiac arrest; therefore, the effect of muscle contraction and respiration of the subjects was not considered.

The current study confirmed one of the findings obtained by Sandoz et al., 2011: the displacement always lagged behind the force. This was also mentioned in studies of the CPR method, which explained that the lag was due to the viscous nature of the chest (Arbogast et al., 2006; Maltese et al., 2008). In addition, Arbogast et al., 2006 suggested that the response during CPR demonstrated more hysteresis than the PMHS in adults. However, the time lag was negligible in the CPR method and their presented force-displacement curves were similar to Shape I in the current study. Larger time lags were observed in this study and the time lags in pediatric patients were larger than in adult volunteers. A simulation was performed to show that different time lags between force time histories and displacement time histories can lead to different shapes of the force-displacement curve. With a slight time lag, the force-displacement curve can assume shape I. If the time lag is around 0.2 s (the time lag ratio is about 5 %), the force-displacement curves will take on shape II. With a larger time lag, the force-displacement curves tend towards shape III. To confirm that the large time lags are not caused by the synchronization or measurement systems, the physiotherapist repeated the operations on a wood board, and no time lags were observed in the tests. Thus, our results provide evidence that time lags between the displacement and the force are a characteristic of the living human trunk under a non-injury, low-rate compression condition.

Various factors may be associated with the time lag. First, the subject's respiration may affect the response of the trunk. The physiotherapist applied regular force to the trunk, and usually the applied pressure sequences were synchronized with the respiratory cycle (Marechal et al., 2007). Adult volunteers were asked to exhale when force was applied and inhale during the release phase. Children were too young to follow this order. Therefore, it was possible for the children to work against the physiotherapist during the manipulations. For example, assume the child inhaled at

the beginning of the compression and opposed the motion of the chest; as a result, the force was increased but without any displacement, and the displacement response of the trunk was delayed. The children were much more active during the manipulations, and this might also have affected the displacement responses of the trunk. Second, muscle contraction could be a confounding factor. Most of the children were crying during the manipulations in the current study. Muscle contraction might have stiffened the thorax and delayed the displacement response. Third, the way in which the physiotherapist applied the force can also influence the displacement response, as shown in Figure 5. Note that these factors also could have influenced each other. For instance, due to an instinctive reaction, the physiotherapist's rapid loading could result in muscle contraction, and such muscle contraction could also block the respiration. Thus, the three factors could have influenced each other and caused the peculiar trunk response during respiratory physiotherapy.

The human body undergoes significant changes during growth, including structural and material changes. Kent et al., 2005 suggested that the ribs become more perpendicular to the spine as age increases but the cortical shell becomes thinner. A far greater percentage of cartilage exists in the child rib cage and the cartilage changes to bone gradually during aging (Forman, 2009; Sandoz et al., 2013a). A high percentage of cartilage may explain the larger time lags of pediatric patients in the current study.

The measured and calculated parameters of the children group are similar to those in Sandoz et al., 2011 and somewhere close to the data from the studies measured with the CPR method. Maltese et al., 2008 studied the force-displacement characteristics of the child chest on 18 child cardiac arrest subjects with the CPR method. The average maximum deflection and corresponding force were 39 (SD 5) mm and 309 (SD 55) N, respectively, which is a little larger than 18 (SD 4) mm for the average maximum deflection and 208 (SD 22) N for the maximum force in the current study. This difference can be explained by the age of the children (14-year-old and 0.7-year-old, respectively). The maximum compression speeds were almost the same in these two studies. Kent et al., 2009 also quantified the force-displacement characteristics of the

Table 2.3 Mechanical parameters of pediatric and adult trunk from previous studies and current study.

Children

	N	Age / Year	Subject	Method	D_{max} / mm	C_{max}	F_{max} / N	V_{max} / m/s	VC_{max} / mm/s
Current study*	8	0.7(0.3)	Living	Respiratory Physiotherapy	18 (4)	0.24 (0.03)	208 (22)	0.25 (0.13)	28.8(12.3)
Sandoz et al.[8] *	26	1(1.3)	Living	Respiratory Physiotherapy	22 (9)	0.19 (0.06)	240 (46)	0.20 (0.11)	24.7(25)
Maltese et al.[6]	18	14(4)	Cardiac arrest	CPR	39(5)	N/A	309(55)	0.25(0.04)	N/A
Ouyang et al.[2]	9	5.2(2.4)	PMHS	Thoracic Impact	50.4 (15.5)	N/A	977 (272)	6.1 (0.2)	2011.1(1110.7)
Kent et al.[3]	1	7	PMHS	CPR	11 to 20	0.07 to 0.13	50 to 150	N/A	N/A
				Thoracic belt	27 to 31	0.17 to 0.20	2068 to 6657	2.6	N/A
				Abdominal belt	33 to 39	0.20 to 0.24	1655 to 5352	2.3	N/A
Kent et al.[4]	3	9.3(3.8)	PMHS	belt loading	21.7 to 54.6	N/A	607 to 6968	N/A	N/A

Adults

	N	Age / Year	Subject	Method	D_{max} / mm	C_{max}	F_{max} / N	V_{max} / m/s	VC_{max} / mm/s
Current study*	8	55(19.9)	Living	Respiratory Physiotherapy	44(9)	0.23(0.03)	250(62)	0.43(0.35)	56.3(53.8)
Arbogast et al.[10]	91	18 - 92	Cardiac arrest	CPR	41.6(7.5)	N/A	297(80)	0.26(0.05)	N/A
Kent et al.[11]	13	71(10)	PMHS	hub testing	31(9)	0.10 to 0.20	474(150)	0.25(0.08)	N/A

* The displacement includes system deformation.

child chest using a 7-year-old pediatric post-mortem human subject under CPR loading and belt compressions. The CPR method had a maximum deflection ranging from 11 mm to 20 mm, with a maximum loading force ranging from 50 N to 150 N, which is a little smaller than in the current study. All of the studies are related to non-impact, dynamic loading conditions, and the rates of compression in these studies are not comparable to the impact tests conducted on pediatric PMHS (Kallieris et al., 1976; Kent et al., 2011; Kent et al., 2009; Ouyang et al., 2006). Ouyang et al., 2006 conducted frontal impacts to study the injury mechanism of the child's thorax with nine child PMHS at a mean impact rate 6.1 m/s. The mean maximum deformation of the chest and the mean maximum force reached 50.4 mm and 977 N, respectively. The mean sternal V_{Cmax} was 2011.1 mm/s, which is much larger than in the current study. Injuries after impact were found in 7 subjects in their study.

For the adults group, the results of the current study are somewhere similar to Arbogast et al., 2006. They measured the thoracic force-deflection during CPR with 91 adults and compared their results to that measured during hub-based loading of adult PMHS by Kent et al., 2004. Arbogast et al., 2006 reported that the mean maximum thoracic deflection was 41.6 (SD 7.5) mm and the mean maximum applied force was 297 (SD 80) N. These results were nearly the same as the current study. However, the mean maximum loading rate in their study (0.26 m/s) was a little smaller than that in the current study (0.43 m/s), which could be the result of different methods employed. Arbogast et al., 2006 also suggested that the CPR subjects had increased chest deflections versus the PMHS subjects with an equivalent applied force and the response during CPR demonstrated more hysteresis than the PMHS.

Comparing the response of the pediatric and adult trunk in the current study, the maximum displacement, maximum loading force and maximum loading rate of the adults group are higher, but the maximum normalized displacement of both groups is similar. All these data give us a better understanding of the living and active pediatric and adult trunk mechanical response under non-impact, dynamic loading conditions, and could be helpful in pediatric and adult trunk modeling. The parameters from previous studies and the current study are listed in Table 2.3.

Some limitations have to be mentioned. First, the rate of loading in the current study was far lower than real crash rates. Therefore, the studied mechanical response of the pediatric and adult trunk may not represent the real reaction of the trunk in the case of a crash. However, this study provided fundamental data regarding the mechanical response under non-injury, low-rate compression conditions. Second, most of the studied children were very young. Children were sometimes very active during the respiratory physiotherapy in the current study, and this could have affected the biomechanical response. Third, the chest and abdomen were treated globally in this study. Therefore, the results represent the whole trunk response. The load applied to the chest and abdomen could be distinguished in further study by using sensors between the practitioner's hands and the subjects. This could help in understanding the mechanical behavior of each region of the trunk. Fourth, it would be interesting to compare children suffering from bronchiolitis with healthy children to investigate the bronchiolitis influence. Unfortunately, it is difficult to collect data from healthy children. Finally, the system deformation is also a limitation. The system deformation can be attributed to the deformation of the physiotherapist's hands, the deformation of the mattress and the deformation of the table itself. In this study, the system deformation contributed to approximate 10 % and 5 % of the total deformations at maximum for the pediatric patients and adult volunteers, respectively. Further studies could separate the system deformation.

2.5 Conclusion

This study investigated the mechanical response of the living and active pediatric and adult trunks during respiratory physiotherapy. Three typical shapes of force-displacement curves were observed. Larger time lags between force time histories and displacement time histories were observed more frequently in children than adults. Different time lags resulted in different shapes of force-displacement curves between children and adults. Factors including respiration, muscle contraction and loading patterns are part of the assumptions to explain this phenomenon.

This study also provided fundamental data regarding the mechanical response of the pediatric and adult trunk under a non-injurious, low-rate compression condition. Complementary data (e.g. muscle activity, breathing) should be collected in the future to go towards *in vivo* trunk modeling.

Chapter 3 – Relationships between rib cortical bone mechanical properties and Bone Mineral Density

3.1 Introduction

The previous chapter investigated the mechanical response of the living and active pediatric and adult trunks during respiratory physiotherapy. Different trunk behavior was found on children and adults. Assumptions have been proposed to explain this phenomenon. For a better understanding of the mechanical responses of pediatric trunk, tissue property is also an important concern. The following chapters will focus on investigating mechanical properties of tissue.

As mentioned before, data of pediatric tissue properties are rare. Pediatric tissues are difficult to collect and experiments on tissue properties are hard to perform. Thus, a non-invasive method on child studies would be helpful. In this chapter, the main goal is to explore a non-invasive method on adult bones which could then be used on a child population.

How could bone mechanical properties be assessed *in vivo*? Some studies reported that bone mechanical properties (e.g. elasticity and strength) are related to Bone Mineral Densities (BMD) measured by Quantitative Computed Tomography (QCT), both for trabecular and cortical bones (Duchemin et al., 2008; Helgason et al., 2008). However, studies mostly concentrated on vertebral, femoral or tibial bones. Whether similar relationships could be expanded to human rib cortical bones is not known. Thus, the goal of this study is to find relationships between BMD measured by QCT and the elastic modulus as well as the ultimate strength (based on biomechanical experiments) for adult rib cortical bones.

3.2 Methods

3.2.1 Population

Seven cadavers were collected from the Département Universitaire d'Anatomie Rockefeller (Lyon, France) through the French program on voluntary corpse donation to science, including 6 males and 1 female aged from 65 to 85 years (mean: 76.6, S.D.: 7.6). Thirteen rib segments of 120 mm in length were taken from the lateral part of the 6^{th} or 8^{th} rib in the straightest part. The surface of the specimens and soft tissues were cleaned and then kept frozen at - 20 ℃. They were thawed at 4 ℃ for 12 hours and at 20 ℃ for 2 hours before the measurements or experiments. Table 3.1 shows the information of the subjects.

Table 3.1: Subjects characteristics

N	Subject ID	Age (years)	Gender	Ribs for measurements/tests*
1	67-2010	85	M	6R, 8R
2	206-2010	67	M	6L, 8L
3	211-2010	80	M	6L, 8L
4	250-2010	80	M	6L, 8R
5	24-2011	65	M	6R
6	138-2011	77	M	6L, 8L
7	144-2011	82	F	6L, 8L
	Mean	76.6		
	S.D.	7.6		

* The number is the rib level number (from top to bottom), L: left; R: right.

3.2.2 Bone Mineral Density (BMD) measurements

3.2.2.1 BMD measured by QCT

QCT is a medical technique which measures BMD using a standard X-ray CT scanner with a calibration phantom to convert Hounsfield Units (HU) of the CT image into BMD values. Before harvesting the rib segments, all the cadavers were full-body scanned by clinical CT devices, including GE LightSpeed Ultra (GE Healthcare, Waukesha, USA) and Philips iCT 256 (Philips, Netherlands). The main acquisition and reconstruction parameters used to obtain CT slices were listed in Table 3.2. The

CT grey level values of the slices (Hounsfield Units (HU)), can be affected by different parameters such as the X-ray source tube voltage, peak kilovoltage (kVp), current (μA), filter types and so on. To correct the scanner drift and the influence of the parameters, a reference phantom was used (Phantom 062M, CIRS Inc., Virginia, USA) during each scan, to convert the HU to equivalent BMD (ρ_{CT}, in milligrams of hydroxyapatite (HA) per cubic centimeters, mg HA/cm^3). The reference phantom contains 3 different bone-equivalent plastic components (200, 800 and 1397 mg HA/cm^3), However, the HU for a specific object (e.g. the 3 reference rods) was found to vary under different scan conditions (this will be detailed in the following chapter). In this study, each subject was scanned together with the same phantom, resulted a specific HU-BMD relationship. Based on this specific relationship, the BMD of scanned objects (ρ_{CT}, in mg HA/cm^3) can be obtained. A CT slice with phantom and the phantom itself are shown in Figure 3.1.

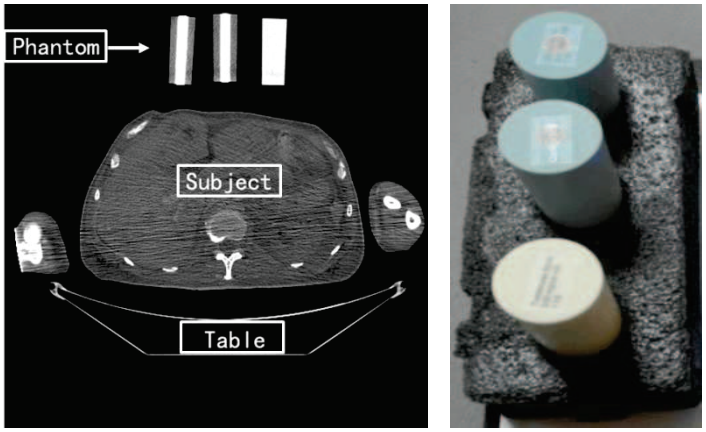

Figure 3.1: Left: a CT slice of a subject scanned together with a phantom; Right: the 3 reference rods of the phantom.

Table 3.2: Main acquisition and reconstruction parameters of the CT slices

N	CT device	Filter type	Tube voltage (kVp)	Current (μA)	Slices thickness (mm)	Thickness between slices (mm)	Field of view (mm*mm)	Matrix	Pixel size (mm)
1	GE LightSpeed Ultra	Body Filter	120	250	1.25	0.625	495*495	512*512	0.97
2	GE LightSpeed Ultra	Body Filter	120	240	1.25	1.25	500*500	512*512	0.98
3	GE LightSpeed Ultra	Body Filter	120	195	1.25	0.625	500*500	512*512	0.98
4	GE LightSpeed Ultra	Body Filter	120	235	1.25	0.625	495*495	512*512	0.97
5	GE LightSpeed Ultra	Body Filter	120	235	1.25	0.625	495*495	512*512	0.97
6	Philips iCT 256	A	120	346	0.9	0.45	495*495	512*512	0.97
7	Philips iCT 256	B	120	537	1	1	495*495	512*512	0.97

Then, the CT slices of the rib cage were 3D (3 dimensional) reconstructed. Previous study has proposed some methods for 3D reconstruction of bones, for example: Keyak et al., 1990. Custom softwares “SliceX” and “IdefX” which were developed by LBM (Laboratoire de Biomécanique, Arts et Métiers ParisTech, France) were used in this study (Aubert et al., 2014). For each 6th and 8th rib, 100 equally spaced cross sectional images from vertebra to the sternum were extracted using the method which was detailed in Sandoz et al., 2013b, as shown in Figure 3.2. The external and internal contours of the rib cortical bone in each cross sectional images were also defined by the custom software. To minimize the partial volume effect and to ensure the location of cortical part, the Region of Interest (ROI) was defined based on the mid-line (the black line as shown in Figure 3.3), which is the center line of the external and internal contours. A simulation was performed to choose the proper percentage of the inner part that could define the ROI. It was found that taking 5 % to 40 % of the inner part (2.5 % to 20 % of both sides along the mid-line) as the ROI could give a stable value of the mean HU. Thus, the 20 % inner part (10 % of both sides along the mid-line) was decided as the ROI in this study, as shown in Figure 3.3. The mean HU value of the pixels in the ROI was then calculated using MATLAB (The Mathworks, Natick, MA, USA). Based on each specific HU-BMD relationship, the mean BMD of the rib cross-section was calculated. For each studied rib, 10 equally spaced cross sectional images from 5 % to 95 % (vertebrae to sternum) of its length were calculated.

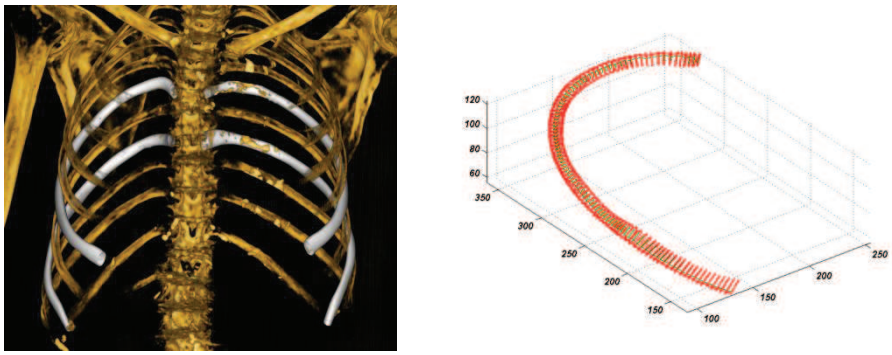

Figure 3.2: Left: 3D reconstruction of the rib cage from the CT slices, the white ribs are the 6th and 8th ribs; Right: an example of 100 equally spaced rib cross sectional images extracted from vertebra to sternum.

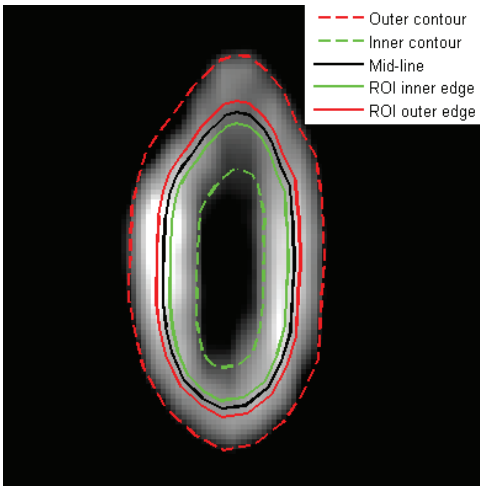

Figure 3.3: A rib cross sectional image with contours and ROI.

3.2.2.2 Bone Mineral Density (BMD) measured by High Resolution Peripheral Quantitative Computed Tomography (HR-pQCT)

HR-pQCT has been used to generate high-resolution images of bones. It can measure the bone mineral density, and assess the 3D geometry and microstructure of the bones. However, HR-pQCT could only measure small size samples.

The 13 rib segments were measured by HR-pQCT device (Xtreme CT, Scanco Medical AG, Brüttisellen, Switzerland), which give parallel slices with an isotropic voxel size of 82 μm. Ribs were automatically segmented, and the cortical and trabecular region of the rib was separated using a semi-automated contouring method

embedded in the HR-pQCT system (μCT Evaluation, Scanco Medical AG, Brüttisellen, Switzerland) (Burghardt et al., 2010; Mitton et al., 2014). The total area (Tt.Ar), the cortical area (Ct.Ar), section modulus (Z), cross sectional area moment of inertia (I) and the cortical bone mineral density (Ct BMD, $\rho_{HR\text{-}pQCT}$, in mg HA/cm^3) were computed with the scanner manufacturer's Image Processing Language (IPL, Scanco Medical AG, Brüttisellen, Switzerland). The mean cortical thickness (Ct.Th) was calculated using a direct method (Hildebrand et al., 1999). Figure 3.4 shows a rib cross sectional image obtained from HR-pQCT. The measured parameters were listed together with other results in Table 3.3 in the following section.

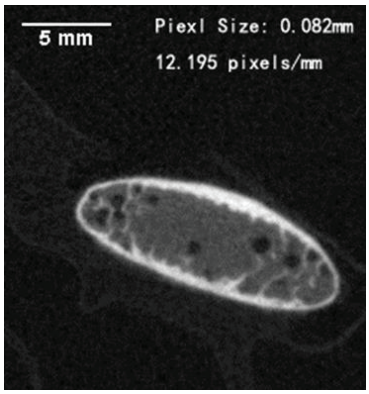

Figure 3.4: A rib cross sectional image obtained by HR-pQCT.

3.2.3 Experiment and mechanical properties measurements

The mechanical properties (Young's modulus E and maximal bending strength σ_{max}) of the 13 rib specimens have been obtained previously (Mitton et al., 2014) and these data were reused in this study. The methods to obtain these data are described in Appendix 1. The mechanical properties of these 13 rib specimens are listed in Table 3.3 in the following section.

3.2.4 Statistics

The statistical analysis was performed using Statgraphics software (version 16.2.04, StatPoint Technologies, Warrenton, USA).

The mean and the standard deviation (S.D.) of the parameters were calculated. The Student's t-test was used for paired comparisons, and an alpha value of $p < 0.05$ is used to assign statistical significance. Linear regression analyses were performed to discuss the correlations between mechanical properties (E and σ_{max}) and BMD measure by QCT and HR-pQCT (ρ_{CT} and $\rho_{HR\text{-}pQCT}$). Squared Pearson's coefficient r^2 was reported to evaluate the correlations. The standard error of the estimate (S.E.E) was also calculated to evaluate the accuracy of the prediction.

3.3 Results

3.3.1 Preliminary results

The Wilcoxon rank-sum test (p-value below 0.05) showed that there was no difference for any parameters by gender ($p > 0.278$), rib levels ($p > 0.685$) or the rib sides (left or right) ($p > 0.7$). Thus, no distinction between genders, rib levels or sides will be made afterwards.

The mean BMD ($\rho_{HR\text{-}pQCT}$) and cross-sectional parameters for each rib segment measured by HR-pQCT was reported in Table 3.3. The BMD distribution along each specimen was presented in the Appendix 2. Since specimens were cut in the lateral part, the mean BMD of ribs in the lateral part measured by QCT (ρ_{CT}) were presented in the table for a comparison purpose. The mechanical properties (E and σ_{max}) measured by two approaches were also listed in Table 3.3.

The BMD for each rib measured by QCT was summarized in Table 3.4. Detailed information illustrating how BMD changes along each rib was presented in Appendix 2. Figure 3.5 showed the distribution of the mean BMD as well as the standard deviation along the rib. Higher BMD values were observed in the lateral part than the anterior and posterior parts. The whole ribs were divided into three parts: the posterior part is defined from 5 % to 25 % of the rib length, the lateral part from 35 % to 65 % rib length and the anterior part from 75 % to 95 % rib length. The BMD in the anterior part of the ribs was significantly lower than the lateral and the posterior part (student's t-test, $p = 0.001$ and $p = 0.03$, respectively).

Table 3.3: Summary of the parameters obtained by HR-pQCT, the BMD measured by QCT and mechanical properties of rib specimens.

N	Specimen ID	Tt.Ar (mm^2)	Ct.Ar (mm^2)	Ct.Th (mm)	I (mm^4)	Z (mm^3)	$\rho_{HR\text{-}pQCT}$ (mg HA/cm^3)	ρ_{CT} (mg HA/cm^3)	E_a (GPa)	$\sigma_{max\,a}$ (MPa)	E_n (GPa)	$\sigma_{max\,n}$ (MPa)
1	67-2010_6R	88.8	21.6	0.69	167.1	43.8	623.4	357.3	5.2	59	4.9	30
2	67-2010_8R	75.9	28.6	0.87	129.1	41.7	729.2	521.0	7.4	85	8.8	52
3	206-2010_6L	90	27.4	0.83	231.3	52.9	636.7	515.2	4.0	49	6.3	34
4	206-2010_8L	92.5	28.7	0.95	224.4	53.5	823.3	555.8	7.2	104	7.4	51
5	211-2010_6L	65.7	22.5	0.94	149.5	36	897.8	535.9	12.2	179	11.7	97
6	211-2010_8L	67.1	24.3	0.91	126.3	37.6	878.9	673.3	10.8	165	11.6	106
7	250-2010_6L	97.2	30.2	0.93	246	59.2	901.2	631.5	8.9	187	10.4	125
8	250-2010_8R	83.2	29.6	0.93	165	48.2	889.0	672.9	12.5	208	10.1	111
9	24-2011_6R	58.5	19.9	0.72	76.1	26.5	836.4	505.3	9.9	119	9.3	73
10	138-2011_6L	71	23.7	0.75	113.3	36.1	633.3	302.8	6.0	73	6.0	65
11	138-2011_8L	63.6	23.5	0.79	88.8	30.9	633.4	290.0	7.6	79	6.9	56
12	144-2011_6L	48.7	20.7	0.81	64.4	21.2	677.0	407.2	6.9	71	6.7	58
13	144-2011_8L	64	22.7	0.82	115.9	32.7	644.2	349.9	10.9	129	10.2	103
	Mean	74.3	24.9	0.84	145.9	40	754.1	486	8.4	116	8.5	74
	S.D.	14.9	3.6	0.09	58.9	11.2	117.7	133.6	2.7	53	2.3	31

* Tt.Ar: total area of the rib section; Ct.Ar: the cortical area; Ct.Th: cortical thickness; I: cross sectional area moment of inertia; Z: section modulus; $\rho_{HR\text{-}pQCT}$: cortical BMD measured by HR-pQCT; ρ_{CT}: cortical BMD measured by QCT; E_a: elastic modulus measured with analytical approach; $\sigma_{max\,a}$: maximal bending strength measured with analytical approach; E_n: elastic modulus measured with numerical approach; $\sigma_{max\,n}$: maximal bending strength measured with numerical approach. The mechanical properties come from Mitton et al., 2014.

Table 3.4: Summary of the BMD measured by QCT (mg HA/cm^3).

N	Subject ID	Rib cross sectional slices (% of the length, vertebrae to sternum)										Mean global*	Mean posterior*	Mean lateral*	Mean anterior*
		5	15	25	35	45	55	65	75	85	95				
1	67-2010_6R	299	352	401	461	379	303	286	270	181	122	305	351	357	191
2	67-2010_8R	295	470	494	604	544	477	459	326	437	284	439	420	521	349
3	206-2010_6L	161	311	274	546	571	410	534	478	222	67	357	249	515	256
4	206-2010_8L	237	429	663	619	616	471	518	470	402	67	449	443	556	313
5	211-2010_6L	382	581	595	476	482	554	631	528	428	395	505	519	536	450
6	211-2010_8L	312	517	629	712	695	674	613	642	565	189	555	486	673	465
7	250-2010_6L	115	569	664	665	628	659	573	444	355	662	534	449	632	487
8	250-2010_8R	363	873	751	684	671	778	558	483	493	126	578	662	673	367
9	24-2011_6R	393	581	431	561	551	454	456	398	287	235	435	469	505	307
10	138-2011_6L	261	365	355	323	298	360	230	213	207	82	269	327	303	167
11	138-2011_8L	194	302	400	312	299	290	259	264	288	52	266	299	290	201
12	144-2011_6L	192	205	368	349	455	448	376	309	297	192	319	255	407	266
13	144-2011_8L	196	394	438	393	403	302	302	274	197	107	301	343	350	193
	Mean	262	458	497	516	507	475	446	392	335	198	409	405	486	309
	S.D.	88	171	147	140	133	154	140	127	122	171	112	117	134	110

* global: slices 5% - 95%; posterior: slices 5% - 25%; lateral: slices 35% - 65%; anterior: slices 75% - 95%.

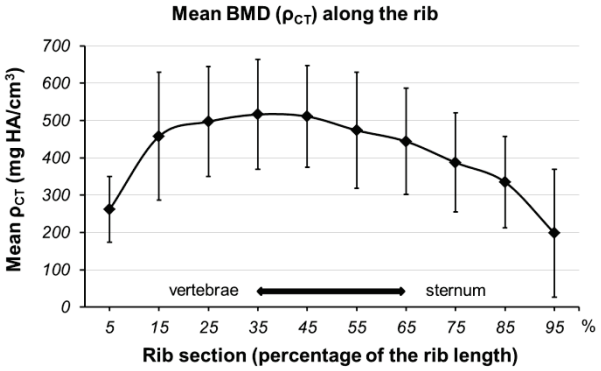

Figure 3.5: Mean and S.D. of the BMD along rib (measured by QCT, n=13).

3.3.2 Correlations between the parameters

The BMD measured by HR-pQCT was significantly correlated with the mechanical properties ($p < 0.01$), as shown in Figure 3.6. The standard error of estimation (S.E.E), which was associated with the prediction of the elastic modulus and the ultimate bending strength by $\rho_{HR\text{-}pQCT}$ was quantified: 1.99 GPa and 27.94 MPa with analytical approach and 1.46 GPa and 23.38 MPa with numerical approach, respectively.

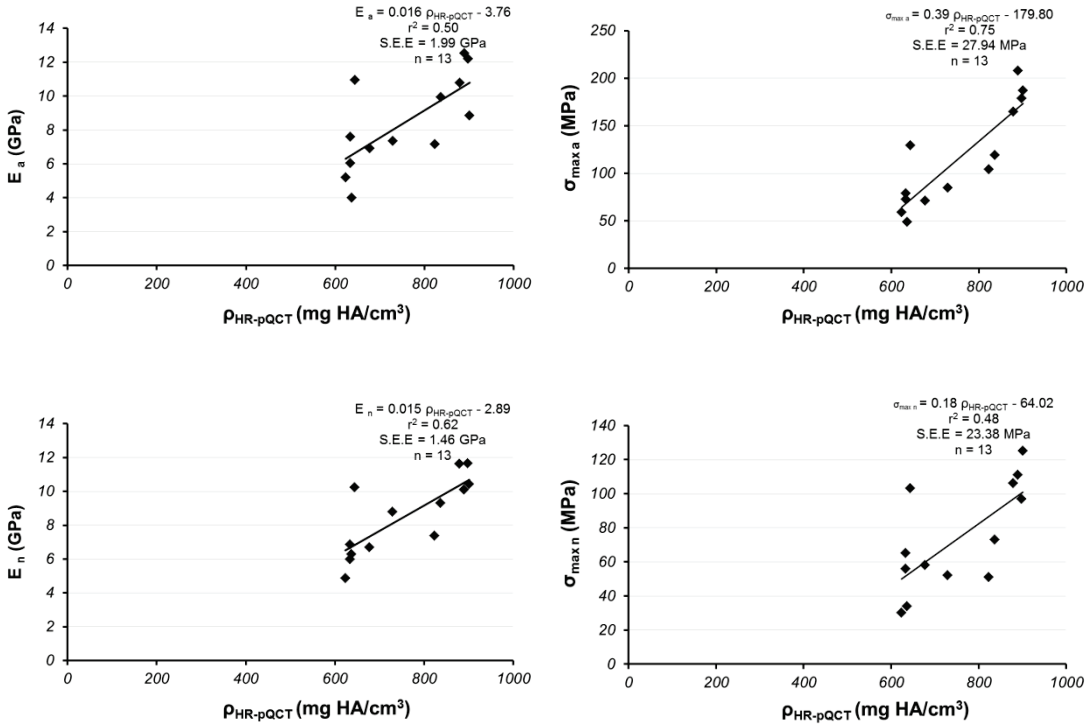

Figure 3.6: Correlations between the BMD measured by HR-pQCT and the mechanical properties (assessed by the analytical approach: top and the numerical approach: bottom).

The BMD measured by QCT was also correlated with the mechanical properties, as shown in Figure 3.7. It was found that ρ_{CT} correlated with the numerical elastic modulus with a determination coefficient r^2 of 0.42 ($p = 0.0158$), and correlated with the analytical maximal bending strength with a determination coefficient r^2 of 0.50 ($p = 0.0086$). The S.E.E was 1.79 GPa and 39.55 MPa, respectively. However, the corrections between ρ_{CT} and analytical elastic modulus and numerical maximal bending strength were not significant ($r^2 = 0.22$ and 0.28, respectively, $p > 0.06$).

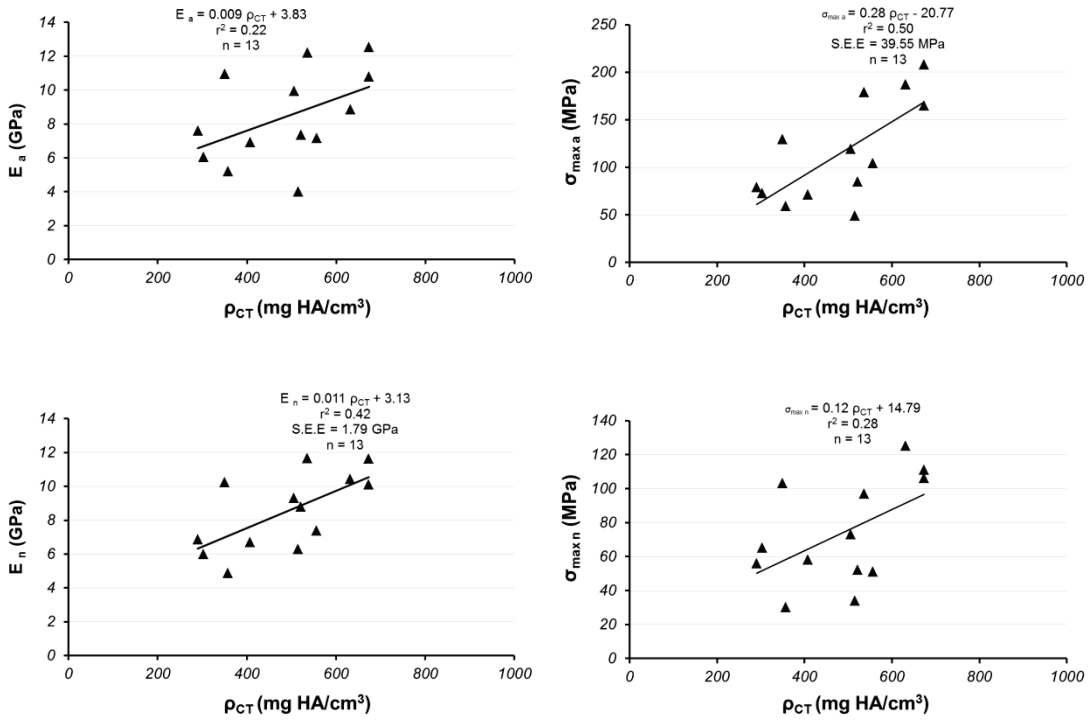

Figure 3.7: Correlations between the BMD measured by QCT and the mechanical properties (assessed by the analytical approach: top and the numerical approach: bottom).

3.3.3 Comparison between BMD measured by two modalities

The BMD obtained by QCT for the ribs in the lateral part was different from the corresponding BMD measured by HR-pQCT, but results obtained by the two modalities were significantly correlated as:

$$\rho_{CT} = 0.98\ \rho_{HR\text{-}pQCT} - 252.9\ (r^2 = 0.75,\ p < 0.001). \qquad (3\text{-}1)$$

The mean difference between the two results was 268.1 mg HA/cm^3, with the mean difference ± 2SD ranged from 200.6 – 403.2 mg HA/cm^3, as shown in Figure 3.8.

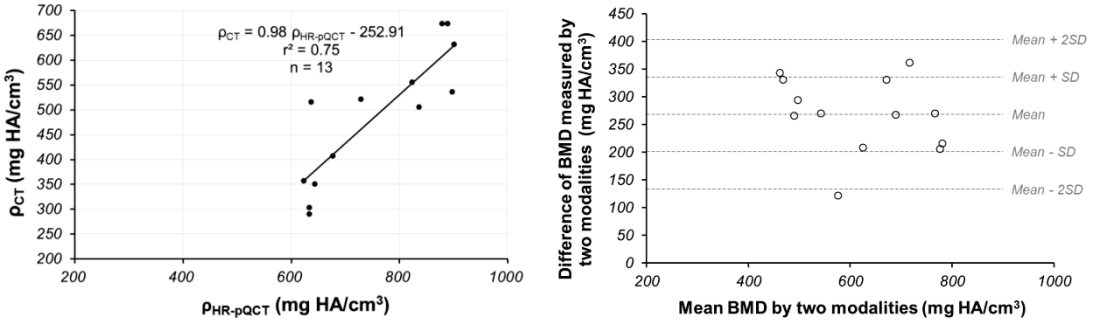

Figure 3.8: Left: correlations for BMD measured by QCT and HR-pQCT. Right: difference between the BMD obtained by QCT and HR-pQCT.

It was assumed that the different results obtained by the two methods were due to the pixel size of the images. Figure 3.9 showed an example of two images for approximately the same rib cross section obtained by the two different imaging techniques. The images obtained by QCT did not have enough resolution to show the edge of the cortical part, and this resulted in blurred images. Even more, the cortical thickness in the QCT images seems to be thicker than it really is. This has also been reported by (Perz et al., 2013). As mentioned above, the mean thickness of the cortical bone was 0.84 mm and it was even smaller than the pixel size (0.97 mm). It has been proven that if the object or region to be imaged is less than twice the Full Width at Half Maximum (FWHM) resolution in x-, y- and z-dimension of the imaging system, the BMD in the object or region is underestimated (Hoffman et al., 1979). This is called "partial volume effect", and a higher resolution could decrease this effect. In the current study, the resolution in HR-pQCT images is 0.082 mm while 0.97 mm in QCT images, thus, the partial volume effect could be neglected in HR-pQCT images but played an important role in QCT images. The BMD measured by HR-pQCT could be treated as an accurate BMD while the BMD measured by QCT were under estimated.

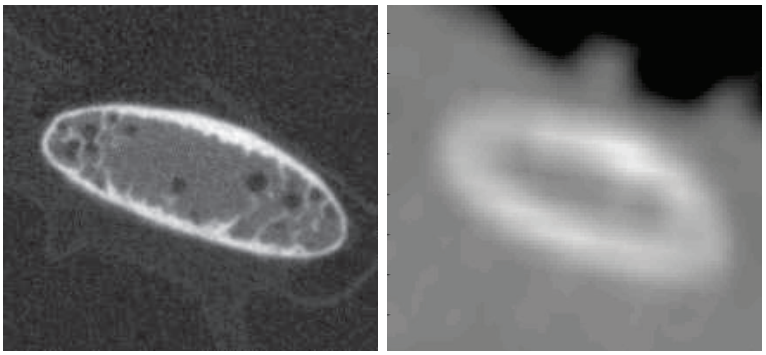

Figure 3.9: Images for the same rib cross section. Left: from HR-pQCT (pixel size: 0.082 mm); Right: from QCT (pixel size: 0.97 mm).

To better understand the partial volume effect, a simulation was performed with 20 HR-pQCT images from 6 rib specimens (3 or 4 rib sectional images were selected randomly for each specimen). The pixels of the original HR-pQCT image as well as the matrix of the original cortical contours were enlarged with the following method: the mean value of 4 pixels (2 x 2 squares) was considered as a new pixel, and this enlarged the pixel size twice; the mean value of 4 x 4 pixels as a new one and the pixel size was enlarged by four times, and so on, as illustrated in Figure 3.10. All the original images were enlarged 2, 4, 8 and 12 times, respectively. The mean BMD of the simulated images were calculated based on the simulated cortical contours, as shown in Figure 3.11.

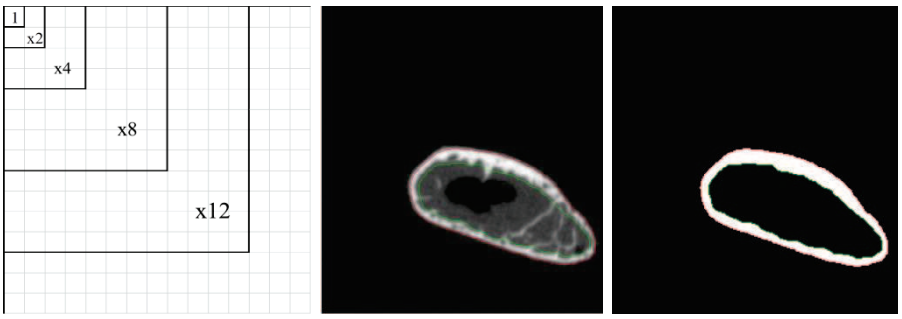

Figure 3.10: Simulation of the partial volume effect.
Left: the method to enlarge the pixels;
Middle: an original rib cross sectional image from HR-pQCT;
Right: the original cortical contour from HR-pQCT.

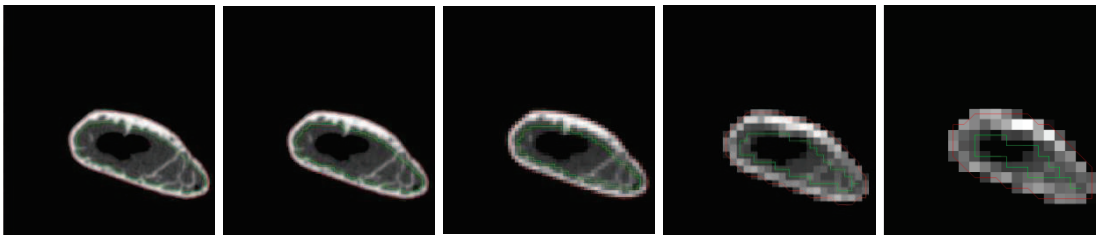

Orignal	simulation (x2)	simulation (x4)	simulation (x8)	simulation (x12)
0.082 mm	0.164 mm	0.328 mm	0.656 mm	0.984 mm

Figure 3.11: The original HR-pQCT image and the simulated images with cortical contours.

Results showed that the "cortical part" was amplified during the enlarging of the pixel size and the calculated BMD decreased, as shown in Figure 3.12. The detailed results of the simulations were listed in Table 3.5.

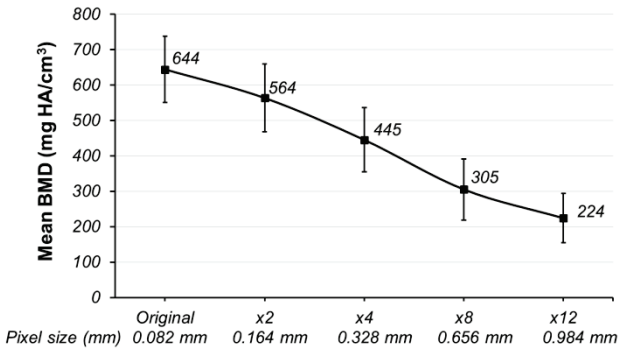

Figure 3.12: The relationship between the BMD and the pixel size (n = 20).

Table 3.5: Results of the simulations

Pixel size (mm)			Simulations				
			Original 0.082	x2 0.164	x4 0.328	x8 0.656	x12 0.984
N	Subject ID	Mean Ct.Th (mm)	BMD (mg HA/cm^3)				
1	138-2011_6L_1	0.75	581	498	381	250	196
2	138-2011_6L_2	0.75	602	518	401	270	189
3	138-2011_6L_3	0.75	561	482	377	259	196
4	138-2011_8L_1	0.79	577	502	402	290	199
5	138-2011_8L_2	0.79	547	475	368	233	148
6	138-2011_8L_3	0.79	595	499	366	222	165
7	144-2011_6L_1	0.81	676	586	460	316	255
8	144-2011_6L_2	0.81	652	563	441	279	203
9	144-2011_6L_3	0.81	584	511	395	266	168
10	144-2011_8L_1	0.82	618	555	453	325	235
11	144-2011_8L_2	0.82	626	546	426	271	177
12	144-2011_8L_3	0.82	573	493	381	240	172
13	67-2010_6R_1	0.69	644	567	452	312	234
14	67-2010_6R_2	0.69	654	570	456	306	255
15	67-2010_6R_3	0.69	605	508	383	259	211
16	67-2010_6R_4	0.69	572	478	349	186	122
17	206-2010_8L_1	0.95	876	791	662	518	400
18	206-2010_8L_2	0.95	779	700	576	421	300
19	206-2010_8L_3	0.95	712	647	532	415	315
20	206-2010_8L_4	0.95	852	782	643	467	340
Mean		0.80	644	564	445	305	224
S.D.		0.09	94	95	91	86	70

The results above only illustrated that the measurements of BMD decreased according to larger pixel size. However, the mean cortical thickness and the BMD for each rib segment are different. To better evaluate the partial volume effect, the cortical thickness of the segments should be taken into account. Thus, two parameters were defined as following:

1) r, which is the ratio of simulated value of BMD to the original value (or real value) of BMD, $r = BMD_{simulated} / BMD_{original}$.
2) p, which is the ratio of rib cortical thickness to the pixel size, p = cortical thickness / pixel size.

The relationships between r and p for each simulated rib segment are presented in Figure 3.13. Based on this simulation, it is suggested that the measured BMD of the cortical part was under-estimated when the thickness of the cortical part was approximately less than 8 times of the pixel size, and it could substantially undervalue the BMD when the thickness of the cortical part was less than twice of the pixel size. For example, the mean rib cortical thickness in this study is 0.84 mm and the pixel size is 0.97 mm. In the next chapter, the pixel size of the scans on child population is 0.68 mm, and the mean rib cortical thickness of a 10 years old child is suggested between 0.57 mm to 0.67 mm with an average value of 0.62 mm (Jiang et al., 2012). The ratios of rib cortical thickness to pixel size are 0.87 and 0.91, respectively. Thus, the underestimation of BMD could be similar for adult rib cortical bones (mean cortical thickness 0.84 mm) with pixel size of 0.97 mm and children (mean cortical thickness 0.62 mm) with pixel size of 0.68 mm. The relationship of BMD measured by QCT and HR-pQCT, which is presented as Equation (3-1), could be used for child population.

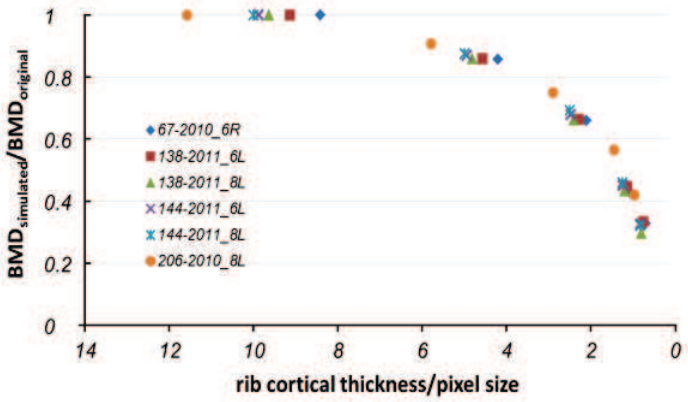

Figure 3.13: The under-estimation of BMD according to the ratio between cortical thickness to pixel size.

3.4 Discussion

This study provided relationships between mechanical properties and the corresponding BMD measured by QCT and HR-pQCT for human rib cortical bones. The results indicate that human rib cortical bone mechanical properties could be

assessed by measuring BMD. QCT and HR-pQCT are two common approaches used to measure BMD. HR-pQCT can give more sharp-edged rib cross sectional images, which are useful to assess accurate rib BMD, while QCT could only provide blurred images due to the low resolution. However, HR-pQCT can only be used to measure small specimens *ex vivo*. On the contrary, QCT measures BMD in a clinical environment. Thus, QCT could provide the bone mechanical properties *in vivo*. This is rather interesting for studies on children since pediatric tissue mechanical properties are rare and hard to be assessed by experiments. The only shortage for QCT measurement is the resolution of the CT images. Based on the technology right now, the matrix of a clinical CT slice is usually 512 x 512, while the Field of View (FOV) of a clinical CT scan on adult rib cage is usually 500 mm x 500 mm. Thus, the pixel size of the image is approximately 1 mm and is not enough to obtain a sharp-edged rib cross sectional image as the mean rib cortical thickness is only 0.84 mm (measured in current study).

Compared to BMD obtained by HR-pQCT, the BMD measured by QCT was less accurate. Partial volume effect was an important reason for the lower values of BMD. However, results from both methods are linearly related ($r^2 = 0.75$, $p < 0.001$). A simulation was performed and indicated that the inaccuracy of BMD measurement by QCT came from the partial volume effect. It showed that the BMD was under evaluated by large pixel size. Despite the inaccuracy of QCT method, it can evaluate BMD *in vivo*, which could be useful for child studies.

The BMD of adult rib cortical bones measured by HR-pQCT was similar but also a little lower than the results measured by Kemper et al., 2007, which reported a mean BMD of 892 mg HA/cm^3, while it was found 754 mg HA/cm^3 in the current study. The mean cortical area was 24.9 mm² in the current study and it was similar as 22.3 mm² reported by Kemper et al., 2007. The mean cortical thickness was also in the range of previous studies. Mohr et al., 2007 reported a mean cortical thickness of 0.81 mm and Charpail, 2006 reported a mean value of 0.61 mm for adult ribs. In the current study, the mean cortical thickness of adult ribs was reported as 0.84 mm. HR-pQCT was showed as a relative accurate method to measure the BMD and the cortical

thickness of human ribs. However, this approach could not lead to *in vivo* studies on human ribs but could be considered as a reference.

The BMD measured by QCT and HR-pQCT were different but significantly related, with a determination coefficient r^2 of 0.75 ($p < 0.001$). The mean difference between the two results in this study was 268 mg HA/cm^3. Both of the BMD measured by QCT and HR-pQCT correlated with the elastic modulus and maximal bending strength of rib cortical bone. However, the correlations with BMD measured by HR-pQCT were a little stronger than BMD measured by QCT. This could be explained by the accuracy of the BMD measurements.

The measurements of BMD by QCT indicated that mechanical properties of human ribs increased then decreased along the rib from vertebrae to sternum, resulting in highest mechanical properties in the lateral part of the ribs. This has been previously described by Stitzel et al., 2003. They presented a study of dynamic three-point bending tests on 92 small rib cortical bone coupons from anterior, lateral, and posterior locations of the rib cages of four cadavers. Their experimental results indicated that material properties varied significantly with respect to region. The Young's modulus and ultimate stress in the lateral portion (11.9 GPa, 153.5 MPa) of the ribs are significantly larger than those in the anterior (7.5 GPa, 116.7 MPa) and posterior (10.7 GPa, 127.7 MPa).

Previous studies have reported that BMD correlated with bone material properties, however, exiting studies only concentrated on human vertebral, femoral or tibial bones (Duchemin et al., 2008; Kaneko et al., 2003; Öhman et al., 2011). This study provided the BMD – mechanical properties relationships for human rib cortical bones for the first time. It was found that the $\rho_{HR\text{-}pQCT}$ – E relationship of human rib cortical bones in the current study meet the cloud of points of BMD – E relationships of human femoral cortical bones in previous studies, as shown in Figure 3.14. This may indicate that human rib cortical bones could share the BMD – E relationship with cortical bones in other anatomical sites. Besides, the study of Öhman et al., 2011 suggested that both children and adults share the relationships between mechanical properties and BMD, thus, the relationships found in this chapter will be used on child

population, to estimate pediatric rib cortical bone mechanical properties. However, it should be noted that the density from these previous studies was assessed by QCT whereas the density was assessed by HR-pQCT in the current study. Compared to rib cortical bones, the cortical bones in other anatomical sites have enough thickness to minimize partial volume effect.

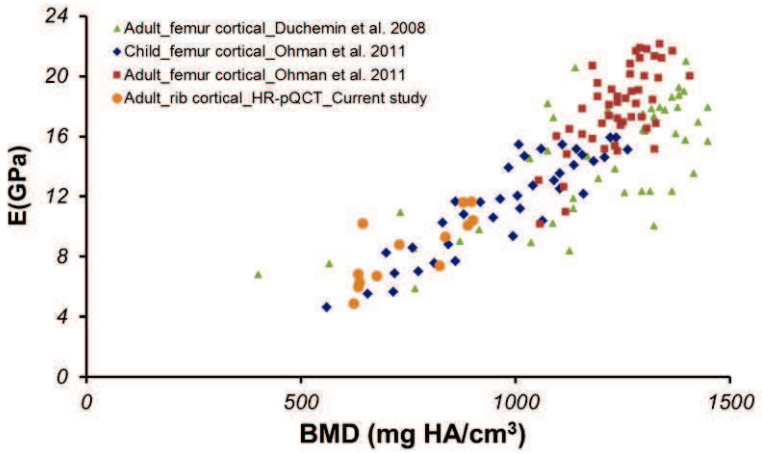

Figure 3.14: Correlations between the BMD and mechanical properties (the data of Öhman et al., 2011 are derived from a combinition of Öhman et al., 2011 and Kaneko et al., 2003).

Some limitations in this study should be pointed out. First, the mechanical properties measured in this study were based on three-point bending experiments. However, tension coupon tests would be more accurate to measure bone mechanical properties. Second, partial volume effect was an important reason for the inaccuracy of BMD measurement with QCT images. This limitation could partly explain the lower correlations and the uncertainties in the relationships between mechanical properties and BMD measured by QCT. Finally, the size of population in this study is limited and should be extended.

3.5 Conclusions

This study provided significant relationships between mechanical properties of human rib cortical bones and BMD measured by QCT and HR-pQCT. These linear

relationships could be used to predict rib mechanical properties from CT scan images. BMD measured by QCT and HR-pQCT are different but linearly related. This *ex-vivo* study is a first step towards the prediction of mechanical properties of human rib cortical bones *in vivo*. In the next chapter, the BMD of pediatric rib cortical bones will be evaluated, and the relationships between the mechanical properties and BMD (for adults) will be used to estimate the mechanical properties of pediatric rib cortical bones.

Chapter 4 – *In vivo* estimation of pediatric rib cortical bone mechanical properties

4.1 Introduction

In the previous chapter, relationships between mechanical properties and BMD were found on adult rib cortical bones. The main goal of this chapter is to estimate the elastic modulus as well as the ultimate strength of pediatric rib cortical bones *in vivo*, based on mechanical property-BMD relationships which were found on adult rib cortical bones. Since the methods of BMD measurements for children and adults are similar but with a little difference, two main issues will be discussed in this chapter: first, the BMD conversion, which is related to the calibration phantoms of the CT scan; second, the estimation of pediatric rib cortical bone material properties.

4.2 Methods

4.2.1 Population

Twenty-eight pediatric patients including 14 boys and 14 girls aged from 9 months to 19 years participated in this study. The patients were divided into 7 groups according to age (4 patients each group). All the children suffered from various known diseases and CT scan was performed on their chest for examination purpose. No rib fracture or rib disease was diagnosed. The scans were performed in Hôpital Femme Mère Enfant (Lyon, France) with a same CT scanner (Philips Brilliance 40, Philips, Netherlands). This study was approved by the French ethical committee (Comité de Protection des Personnes Sud-Est II). Table 4.1 shows the information of the patients.

4.2.2 BMD measurements

The CT images were generated contiguously in the transverse plane of the patients. The acquisition and reconstruction parameters used to obtain CT slices changes

according to the subjects. In general, the tube current changed from 34 to 168 mAs, besides, adaptive tube voltage (80 and 120 kVp) were chosen to minimize the radiation dose. Different filter types (type B and D) were used to enhance either soft tissue features or bone detail in images. The slice thickness was 1.5 mm or 1.0 mm with a spacing of 0.75 mm or 0.5 mm between slices, respectively. The matrix kept 512 x 512 and Field of View (FOV) was 350 mm x 350 mm, resulted in a pixel size of 0.68 mm of the CT images.

Table 4.1: List of the subjects

Group	N	Subject	Age (year)	Sex	Stature (cm)	Mass (kg)	BMI* (kg/m^2)	Description of the disease
1	1	DE01	0.9	M	68	7.0	15.1	dyspnea
	2	DE02	0.7	M	70	8.6	17.6	cough
	3	DE03	0.8	M	80	7.0	10.9	tuberculosis
	4	DE04	1.2	F	73	8.0	15.0	pulmonary abscess
2	5	DE05	1.8	F	79	10.0	16.0	cystic fibrosis
	6	DE06	1.9	F	75	12.0	21.3	neuroblastoma
	7	DE07	1.3	F	72	8.0	15.4	cystic fibrosis
	8	DE08	2.1	M	90	13.0	16.0	cat scratch
3	9	DE09	3.3	F	97	17.5	18.6	chronic bronchitis
	10	DE10	3.1	M	90	12.0	14.8	severe asthma
	11	DE11	3.5	M	85	13.0	18.0	syndrome
	12	DE12	2.4	F	90	13.0	16.0	cystic fibrosis
4	13	DE13	6.8	M	122	22.0	14.8	cystic fibrosis
	14	DE14	7.3	M	130	27.0	16.0	asthma
	15	DE15	6.8	F	118	19.4	13.9	cystic fibrosis
	16	DE16	6.6	M	121	25.0	17.1	pneumonia
5	17	DE17	8.7	F	133	27.0	15.3	asthma
	18	DE18	11.1	M	135	50.0	27.4	pneumonia
	19	DE19	11.6	F	157	46.0	18.7	pneumonia
	20	DE20	9.1	F	140	47.0	24.0	tuberculosis
6	21	DE21	14.7	M	170	54.0	18.7	Mac lead
	22	DE22	13.4	M	154	50.0	21.1	pneumonia
	23	DE23	13.0	F	162	43.0	16.4	lymphedema
	24	DE24	14.4	F	160	53.0	20.7	pneumonia
7	25	DE25	18.0	M	180	55.0	17.0	pneumonia
	26	DE26	16.2	F	162	51.0	19.4	pneumonia
	27	DE27	17.7	M	180	82.0	25.3	lymphedema
	28	DE28	19.1	F	181	73.0	22.3	teratoma

* BMI: body mass index, = weight/$stature^2$.

A typical CT slice of the patients are showed in Figure 4.1. During each CT scan, a pad-like calibration phantom (as shown in Figure 4.1, Model 3 CT Calibration Phantom, Mindways Software, US) was placed on top of the CT scanner table and under the patient. The patient and the phantom were scanned together. The calibration phantom provided a linear calibration in each image for estimating the equivalent density of materials within the patient being scanned. The Model 3 CT Calibration Phantom is composed of a plastic base containing 5 embedded rods of reference material. The base material is not used as a reference material. The 5 rods contain known and varying amounts of low and high atomic materials. Since the phantom was used to estimate the equivalent density of cortical bone, the 3 reference materials who has higher equivalent densities (rod C, D and E, with equivalent density of 58.9 ± 0.1, 157.0 ± 0.3 and 375.8 ± 0.9 mg K_2HPO_4/cc) were selected to convert the CT grey level values (Hounsfield Units, HU) to equivalent K_2HPO_4 densities (ρ_{CT}).

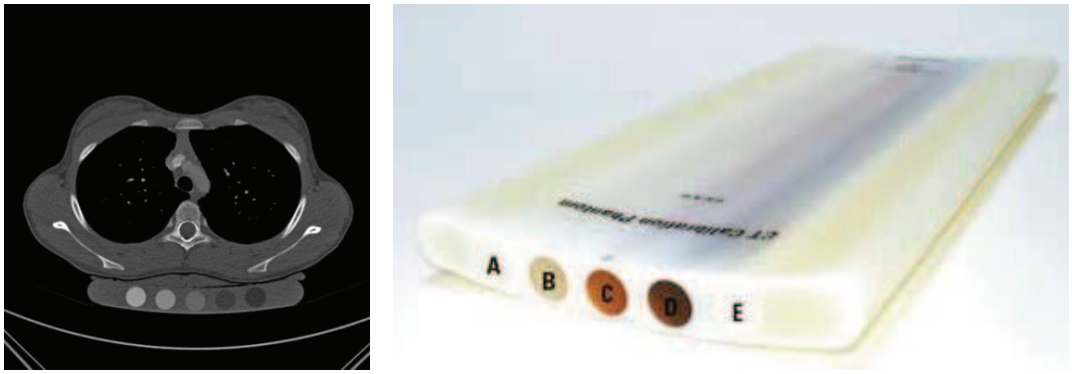

Figure 4.1: Left: a typical CT slice of the patient with the calibration phantom; Right: Model 3 CT Calibration Phantom (Mindways Software, US).

For each 6th rib of the patients, 100 equally spaced cross sectional images from vertebral to the sternal were extracted using the method which has been described in the previous chapter, as shown in Figure 4.2. The contours of the rib cortical part were defined by custom software "SliceX" and "IdefX" which were developed by LBM (Laboratoire de Biomécanique, Arts et Métiers ParisTech, France). To avoid the edge effect and to ensure the location of cortical part, the Region of Interest (ROI) was defined as the 20 % inner part (10 % of both sides along the mid-line), which has also been described in the previous chapter, as shown in Figure 4.3. The mean HU value of

the pixels in the ROI was then calculated by MATLAB (The Mathworks, Natick, MA, USA), as the HU for the rib cross-sectional image. Based on the calibration phantom, which gave the HU - BMD relationship, the mean BMD of the rib cross section was acquired in mg K_2HPO_4/cc. For each studied rib, 10 equally spaced cross-sectional images from 5 % - 95 % (vertebrae to sternum) of its length were calculated.

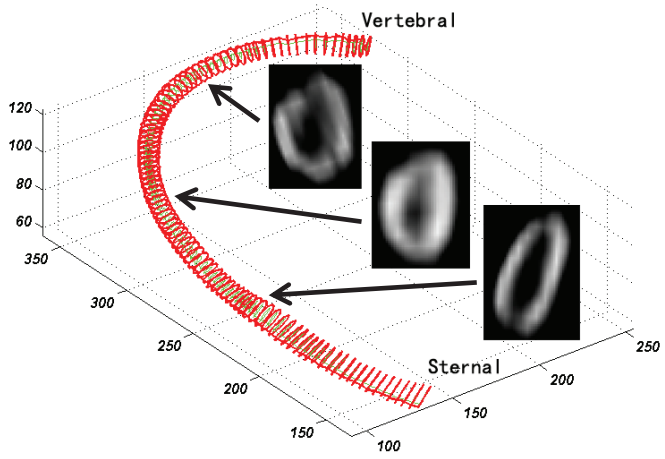

Figure 4.2: An example of 100 cross-sectional images from vertebral to sternal, along with 3 examples of rib cross sectional images (subject DE20, 9 years old girl).

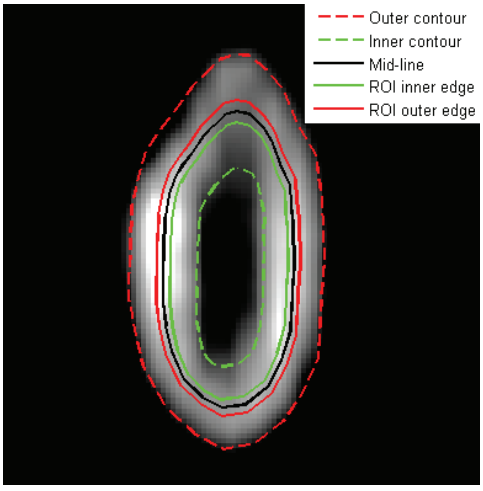

Figure 4.3: A rib cross sectional image with contours and Region of Interest (ROI).

4.2.3 Cross calibration of two phantoms

As mentioned above, the calibration phantom was used for each acquisition. It is because the HU values of the slices can be affected by factors including, but are not

limited to, manufacturer-supplied corrections for beam hardening and scattered radiation, x-ray energy spectrum, localized beam hardening effects, and artifacts in the images (MindwaysSoftwareInc., 2005). It was observed in this study that the HU for a specific material varied according to parameters such as X-ray source tube voltage (kVp), tube current (μA), and filter types. To correct the scanner drift and the influence of the parameters, a reference phantom is necessary during each scan, to convert the HU into equivalent BMD (ρ_{CT}, in milligrams of dipotassium phosphate (K_2HPO_4) per cubic centimeters, mg K_2HPO_4/cc). The data in this study also gives the opportunity to investigate the HU variations under different acquisition conditions and reconstruction parameters, which could be interesting for potential studies on pediatric ribs using non-calibrated CT images (Sandoz et al., 2013b).

Although different kinds of reference phantoms have been introduced in various studies, the material compositions of the reference rods are almost only of two kinds: hydroxyapatite (HA) and dipotassium phosphate (K_2HPO_4). Hydroxyapatite is the main mineral of human bones and more commonly used as calibration references, while K_2HPO_4 has similar attenuation as HA since their Compton effects and photoelectric effects are similar. As a consequence, the densities reported according to the two standards are comparable to each other (Suzuki et al., 1991). Both of these two standards were used in our study. The phantom reported densities in mg HA/cm^3 was involved in the study on adult subjects, while the phantom reported densities in mg K_2HPO_4/cc was involved in the study on pediatric patients. Since the main purpose of this study is to predict material properties of pediatric rib cortical bones base on relationship between material property and BMD in mg HA/cm^3, a cross calibration of the two phantoms should be performed to convert BMD in mg K_2HPO_4/cc into BMD in mg HA/cm^3. Both phantoms are illustrated in Figure 4.4.

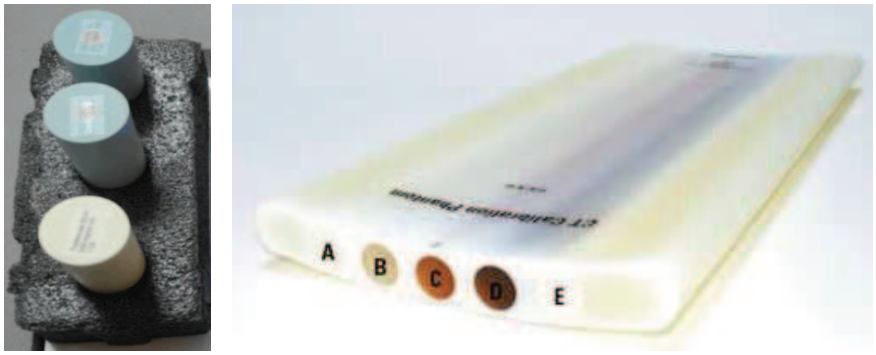

Figure 4.4: Left: Phantom 062M (CIRS Inc., Virginia, US, in mg HA/cm^3) used on adult subjects; Right: Model 3 CT Calibration Phantom (Mindways Software, US, in mg K_2HPO_4/cc) used on pediatric subjects.

In the previous chapter, ten cadaveric adult subjects were scanned together with Phantom 062M, using 2 clinical CT devices including GE LightSpeed Ultra and Philips iCT 256. For each subject, several scans were performed using different acquisition and reconstruction parameters (tube current, filter type, etc.), resulting totally 47 different scans. The tube voltage resisted 120 kVp for all these scans. These data allows studying the HU variation with same tube voltage but other acquisition and reconstruction parameters (tube current, filter type, etc.) are different.

The scans on child population gave the opportunity to evaluate the role of tube voltage. Twenty-eight children were scanned with Model 3 CT Calibration Phantom. Seven children were scanned under a tube voltage of 80 kVp while others were scanned under a tube voltage of 120 kVp. Images were post-processed after each scan using different filters. They can be generated to enhance bone detail on the one hand and to observe subtle low contrast masses on the other, without the need to re-scan the patient. In brief, the scans on child population result in totally 51 sets of images, including 14 sets of images with 80 kVp and 37 sets with 120 kVp.

To cross calibrate the two phantoms, 6 scans were performed using a CT-scan Philips MX8000 IDT 10 (Philips Inc., Netherlands), as shown in Figure 4.5. For each scan, images were reconstructed with filter type B and filter type D. Scans were performed with the following acquisition parameters (120 kVp, 297 mAs, slice thickness 1 mm, 0.5 mm between slices, matrix 512 x 512, FOV 350 mm x 350 mm, pixel size 0.68

mm). The HU of the reference rods was calculated with software ImageJ (version 1.47, National Institutes of Health, US).

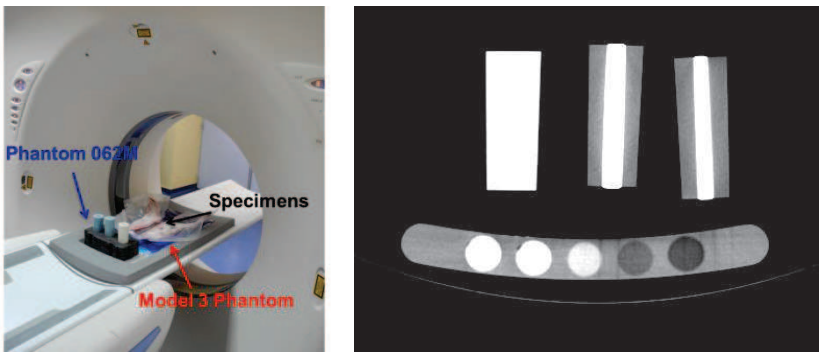

Figure 4.5: Cross calibration of the two phantoms. Left: two phantoms scanned together with specimens; Right: a CT slice of the two phantoms.

4.2.4 Statistics

The statistical analysis was performed by Statgraphics software (version 16.2.04, StatPoint Technologies, Warrenton, US).

The mean and the standard deviation (S.D.) of the parameters were calculated. The Student's t-test was used for paired comparisons, and an alpha value of $p < 0.05$ is considered to assign statistical significance. Linear or power regression analyses were performed to discuss the correlations between parameters. Determination coefficient r^2 was reported to evaluate the correlations.

4.3 Results

The Wilcoxon rank-sum test (p-value below 0.05) showed that there was no difference for any parameters by gender ($p > 0.278$) or the rib sides (left or right) ($p > 0.7$). Thus, no distinction between genders or sides will be made afterwards.

4.3.1 Analysis of two calibration phantoms

Variations of HU were found for the reference rods of the phantom 062M (HA equivalent) on adult cadavers, as shown in Table 4.2. It illustrated that HU could vary approximately 3% - 6%, under the condition of same clinical CT device and tube voltage. Considering the 47 CT scans as a whole (different CT devices but the same tube voltage of 120 kVp), the variation of HU reaches to approximately 7% - 8%.

Table 4.2: Mean HU of the reference rods in Phantom 062M

HU of Phantom 062M

Reference rod Eq. density (mg HA/cm^3)		Trabecular Bone 200	Dense Bone 800	Cortical Bone 1397
GE LightSpeed, n=16 @ 120 kVp	Mean HU	248.17	854.62	1229.53
	S.D.	8.11	40.42	70.39
	C.V., %	3.27%	4.73%	5.73%
Philips iCT 256, n=19 @ 120 kVp	Mean HU	255.06	920.76	1335.80
	S.D.	11.06	41.90	50.19
	C.V., %	4.34%	4.55%	3.76%
Philips Mx 8000, n=12 @ 120 kVp	Mean HU	292.32	974.41	1405.66
	S.D.	14.15	48.31	56.77
	C.V., %	4.84%	4.96%	4.04%
All, n=47, @ 120 kVp	Mean HU	262.23	911.94	1317.46
	S.D.	21.06	63.01	90.72
	C.V., %	8.03%	6.91%	6.89%

* HA: Hydroxyapatite; Eq.: equivalent; C.V.: coefficient of variation, C.V.=S.D./Mean HU

Figure 4.6 showed the relationship between HU and equivalent BMD (in mg HA/cm^3) based on these 47 scans. It suggested that HU of a specific material could be converted to BMD (ρ_{CT}, in mg HA/cm^3) with the following equation:

$$\rho_{CT} = 1.11HU - 126.66 \quad (r^2 = 0.98, p < 0.001) \qquad (4\text{-}1)$$

However, it should be noted that Equation (4-1) might be only used under the condition of the tube voltage in 120kVp and subjects scanned by the 3 mentioned clinical CT devices. Using Equation (4-1) as a unique equation to convert HU into BMD has risks, since HU for a specific material can have a variation of approximately 7% - 8%. For example, for the 3 reference rods of the phantom, the differences between calculated BMD based on Equation (4-1) and the real BMD (200, 800 or 1397 mg HA/cm^3) are significant, as shown in Figure 4.7. For this reason, the

calibration phantom was scanned together with subjects for each scan in this study. A specific regression between HU and equivalent BMD (in mg HA/cm^3) was calculated for each scan, and was used to convert HU into BMD.

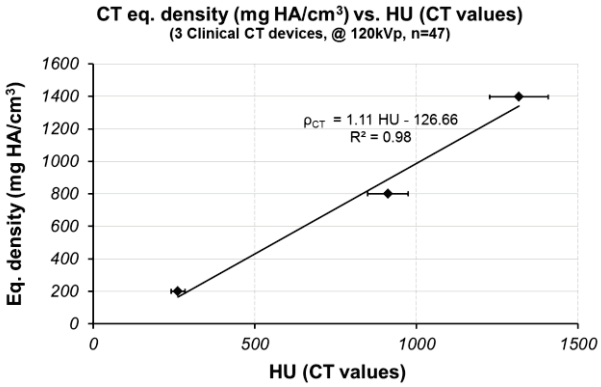

Figure 4.6: The relationship between HU and equivalent BMD (in mg HA/cm^3).

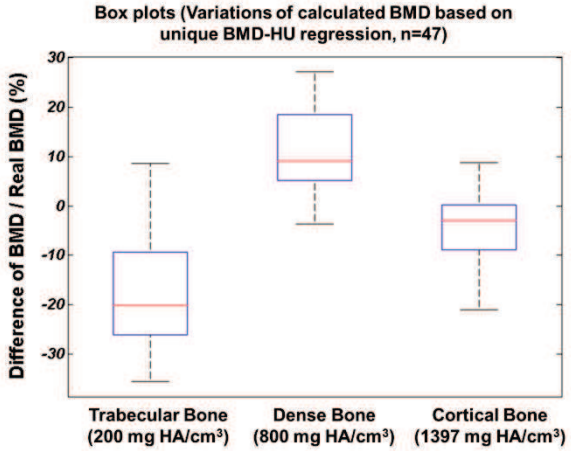

Figure 4.7: The differences between calculated BMD based on Equation (4-1) and the real BMD for the 3 reference rods of the phantom.

The scans on child population gave the opportunity to evaluate the role of tube voltage. For a specific material scanned by a unique CT device, if the tube voltage changed from 120 kVp to 80 kVp, the HU changed. For example, if the tube voltage changed from 120 kVp to 80 kVp, the HU of reference rod C (with an equivalent density of 58.9 mg K_2HPO_4/cm^3) could change from 209.16 to 235.13, increasing 12.4 %, while the HU of rod E (with an equivalent density of 375.8 mg K_2HPO_4/cm^3) could change from 513.79 to 705.74, increasing 37.3 %, as shown in Table 4.3.

Table 4.3: Mean HU of the reference rods in Model 3 CT Calibration Phantom

HU of Model 3 CT Calibration Phantom

Reference rod		C	D	E
Eq. density (mg K_2HPO_4/cm^3)		58.9	157.0	375.8
Philips Brilliance 40, n=14, @ 80kVp	Mean HU	235.13	467.42	705.74
	S.D.	22.08	33.70	48.42
	C.V., %	9.39%	7.21%	6.86%
Philips Brilliance 40, n=37, @ 120kVp	Mean HU	209.16	388.93	513.79
	S.D.	19.84	28.76	37.01
	C.V., %	9.49%	7.39%	7.20%

Figure 4.8 showed the relationship between HU and equivalent BMD (in mg HA/cm^3) based on the 14 scans at 80 kVp and 37 scans at 120 kVp. It indicated the importance of the tube voltage since it could greatly change the HU of a specific material, especially for the materials with higher values of equivalent BMD. The relationships between HU (in mg K_2HPO_4/cm^3) and BMD were suggested as Equation (4-2) (at 120 kVp) and (4-3) (at 80 kVp).

$$\rho_{CT} = 1.01HU - 175.45 \quad (r^2 = 0.90, p < 0.001) \qquad (4\text{-}2)$$

$$\rho_{CT} = 0.63HU - 123.85 \quad (r^2 = 0.96, p < 0.001) \qquad (4\text{-}3)$$

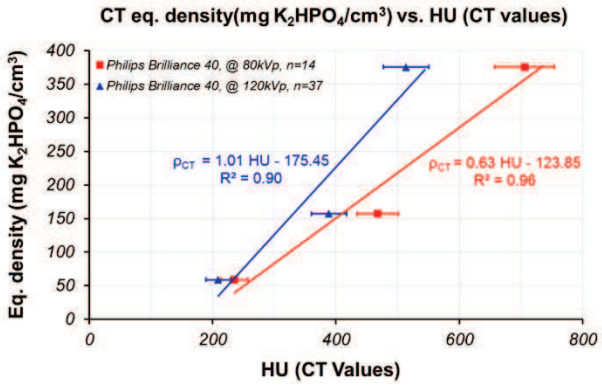

Figure 4.8: The relationship between HU and equivalent BMD (in mg K_2HPO_4/cm^3).

The results of the cross calibration are shown in Table 4.4. The results indicated that the variations of HU were less than 1 % if the parameters kept all the same (same CT device, same acquisition and reconstruction parameters). The change of filter type could lead to approximately 5 % - 10 % variations of HU.

Table 4.4: Mean HU of the reference rods in Phantom 062M and Model 3 CT Calibration Phantom

HU of Phantom 062M and Model 3 CT Calibration Phantom

		Phantom 062M (HA eq.)			Phantom Model 3 (K_2HPO_4 eq.)		
Reference Rod		Trabecular Bone	Dense Bone	Cortical Bone	C	D	E
Eq. density (mg/cm^3)		200	800	1397	58.9	157	375.8
Philips Mx8000, Filter B, n=6	Mean HU	278.82	928.63	1352.03	206.05	380.55	517.26
	S.D.	0.61	9.35	6.44	1.83	1.76	1.71
	C.V., %	0.22%	1.01%	0.48%	0.89%	0.46%	0.33%
Philips Mx8000, Filter D, n=6	Mean HU	305.83	1020.19	1459.28	239.67	421.99	567.34
	S.D.	1.53	4.21	12.16	2.06	2.29	2.22
	C.V., %	0.50%	0.41%	0.83%	0.86%	0.54%	0.39%
Philips Mx8000, n=12	Mean HU	292.32	974.41	1405.66	222.86	401.27	542.30
	S.D.	19.09	64.74	75.84	23.77	29.30	35.42
	C.V., %	6.53%	6.64%	5.40%	10.67%	7.30%	6.53%

The densities reported according to the two standards were converted to each other based on the results of the 12 cross calibration scans, as shown in Figure 4.9. The BMD using the two calibration phantom was related as:

$$\rho_{CT}\,(\text{mg HA/cm}^3) = 1.08\ \rho_{CT}\,(\text{mg } K_2HPO_4\text{/cc}) + 55.77\ (r^2 = 0.99,\ p < 0.001) \quad (4\text{-}4)$$

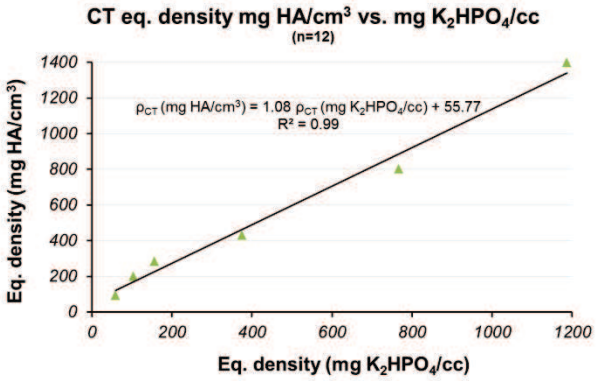

Figure 4.9: The relationship between BMD in two phantoms.

In conclusion, the HU of a specific material changes under different conditions of the CT scan. For a specific subject, the variation of HU can be less than 1 % when scanned in a same and constant condition. If some parameters are changed, the HU will also change. For example, the change of filter type can lead to approximately 5 %

- 10 % variations of HU, and the change of the CT devices and other parameters (tube current, filter type, etc.) can lead to approximately 7 % - 8 % variations of the HU. Tube voltage is the most sensitive parameter, since the change of tube voltage can lead to 37.3 % or even more variations of HU. The change of tube voltage is more sensitive to the materials with high equivalent BMD. The parameters of CT scans in clinical environment can hardly kept constant. Thus, it is better to perform the scans with a calibration phantom each time, to get a more accurate value of BMD. The BMD can be reported in two different standards: BMD in mg HA/cm^3 and BMD in mg K_2HPO_4/cm^3, but they can be converted from one to another.

4.3.2 Prediction of material properties of pediatric rib cortical bones

From the results of the previous chapter, it is known that both the BMD measured by clinical CT and HR-pQCT are linearly related to material properties (Elastic modulus E and maximal bending strength σ_{max}). However, the relationships measured by HR-pQCT have higher coefficient of determination (r^2). In this study, the material properties of pediatric rib cortical bones will be predicted based on the relationships found by HR-pQCT approach, which has been detailed in the previous chapter. The relationships are listed as follows:

$$E = 0.015\ \rho_{HR\text{-}pQCT} - 2.89\ (r^2 = 0.62,\ p < 0.01) \quad (4\text{-}5)$$

$$\sigma_{max} = 0.18\ \rho_{HR\text{-}pQCT} - 64.02\ (r^2 = 0.48,\ p < 0.01) \quad (4\text{-}6)$$

To use the Equations (4-5) and (4-6), two steps should be followed: first, using the Equation (4-4) to convert BMD in mg K_2HPO_4/cm^3 to BMD in mg HA/cm^3; second, based on the simulation in previous chapter, convert BMD in QCT into BMD in HR-pQCT, using the equation as follows:

$$\rho_{CT} = 0.98\ \rho_{HR\text{-}pQCT} - 252.9\ (r^2 = 0.75,\ p < 0.001) \quad (4\text{-}7)$$

The whole ribs were divided into three parts: the posterior part is defined from 5 % to 25 % of the rib length, the lateral part from 35 % to 65 % rib length and the anterior

part from 75 % to 95 % rib length. The predicted elastic modulus E and maximal bending strength σ_{max} are listed in Table 4.5 and Table 4.6.

It was found that the material properties of the ribs increase then decrease from vertebrae to sternum, resulting in higher material properties in the lateral part than the anterior and the posterior part. Besides, the material properties increase along the age, resulting approximately 2 times of the material properties values in older group than the young group, as shown in Figure 4.10.

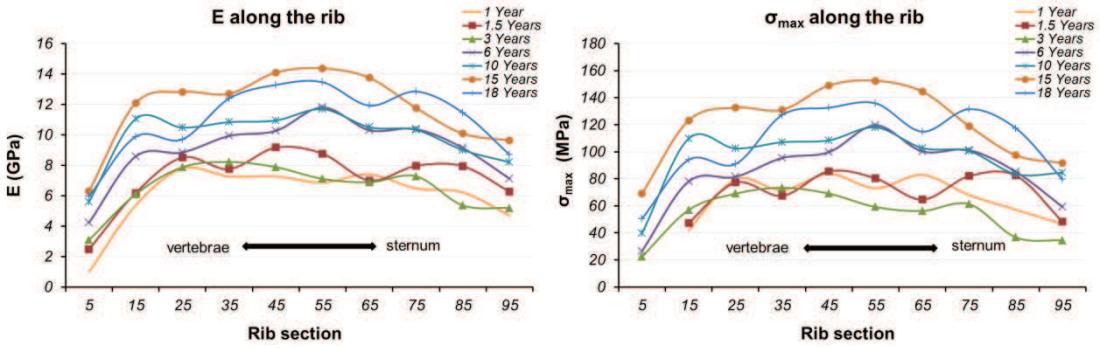

Figure 4.10: The predicted elastic properties (E) and maximal bending strength (σ_{max}) along the rib.

The material properties increase along the age. The mean values of the elastic modulus and maximal bending strength in each age group were calculated, and showed a growing trend along the age, as shown in Figure 4.11. The regressions were given as follows:

$$E = 6.01\ Age^{0.22}\ (r^2 = 0.88,\ p < 0.001) \quad (4\text{-}8)$$

$$\sigma_{max} = 54.50\ Age^{0.25}\ (r^2 = 0.78,\ p < 0.001) \quad (4\text{-}9)$$

Table 4.5. Summary of the predicted E (GPa).

Group		Age (year)	Rib cross sectional slices (% of the length, vertebrae to sternum)										Mean global*	Mean posterior*	Mean lateral*	Mean anterior*
			5	15	25	35	45	55	65	75	85	95				
1	Mean	0.9	1.0	5.4	7.8	7.3	7.3	6.9	7.4	6.5	6.2	4.7	6.3	6.0	7.3	5.8
	S.D.	0.2	2.8	1.5	2.6	3.0	3.4	2.9	3.2	3.1	2.7	2.3	2.6	1.9	2.9	2.6
2	Mean	1.8	2.5	6.2	8.5	7.8	9.2	8.8	7.0	8.0	7.9	6.3	7.0	5.5	8.0	7.2
	S.D.	0.4	0.6	1.6	1.3	1.9	1.9	3.7	2.5	2.6	2.7	1.5	1.6	1.0	2.4	2.4
3	Mean	3.1	3.1	6.1	7.9	8.2	7.9	7.1	6.9	7.3	5.4	5.2	6.4	5.9	7.3	5.9
	S.D.	0.5	1.4	2.1	1.5	1.9	2.3	1.3	1.2	1.7	2.2	1.6	1.1	1.2	1.5	1.7
4	Mean	6.9	4.2	8.6	8.8	9.9	10.3	11.8	10.3	10.4	9.1	7.1	9.3	7.6	10.6	8.9
	S.D.	0.3	0.8	3.0	2.3	3.4	3.6	3.2	3.4	3.4	3.1	2.7	2.6	2.2	3.3	3.0
5	Mean	10.1	5.6	11.0	10.5	10.8	10.9	11.7	10.5	10.3	9.0	8.2	10.1	10.3	10.9	9.1
	S.D.	1.3	0.8	1.5	1.8	2.6	2.3	1.9	3.1	3.1	3.2	2.9	1.8	1.3	2.0	2.8
6	Mean	13.9	6.3	12.1	12.8	12.7	14.1	14.4	13.7	11.8	10.1	9.6	11.9	11.0	13.7	10.5
	S.D.	0.7	3.3	2.3	1.2	3.3	3.4	2.6	2.3	2.0	3.3	1.7	1.9	1.9	2.7	2.1
7	Mean	17.8	6.0	9.9	9.7	12.4	13.3	13.5	11.9	12.8	11.5	8.7	10.9	8.0	12.6	11.0
	S.D.	1.1	1.8	3.0	3.2	4.0	4.0	1.9	2.1	0.8	1.2	1.1	1.5	2.4	2.8	0.6

* global: slices 5% - 95%; posterior: slices 5% - 25%; lateral: slices 35% - 65%; anterior: slices 75% - 95%.

Table 4.6. Summary of the predicted σ_{max} (MPa).

Group		Age (year)	Rib cross sectional slices (% of the length, vertebrae to sternum)										Mean global*	Mean posterior*	Mean lateral*	Mean anterior*
			5	15	25	35	45	55	65	75	85	95				
1	Mean	0.9	NAN	41.7	79.5	71.7	83.6	73.0	82.9	68.0	57.2	46.4	59.6	57.2	70.9	58.1
	S.D.	0.2	NAN	15.7	14.4	29.7	25.9	24.4	19.9	29.5	26.8	11.6	23.4	7.7	29.2	19.8
2	Mean	1.8	NAN	47.2	77.2	67.4	85.6	80.4	64.7	82.0	82.3	48.2	66.4	60.3	72.5	70.8
	S.D.	0.4	NAN	20.2	17.1	24.9	25.0	47.4	28.2	11.2	12.4	19.5	19.3	16.9	29.5	12.8
3	Mean	3.1	22.5	56.9	69.0	73.4	69.0	59.1	56.3	61.3	36.7	34.4	53.8	55.2	61.8	44.1
	S.D.	0.5	17.9	7.5	19.4	24.9	29.3	17.3	15.2	22.2	28.8	20.8	15.0	15.7	19.6	21.5
4	Mean	6.9	26.6	78.1	81.4	95.4	99.7	119.5	100.2	101.2	85.2	59.3	89.5	69.4	103.7	81.9
	S.D.	0.3	10.6	38.7	30.2	43.6	46.9	40.5	43.6	44.4	40.2	34.5	37.1	34.5	42.4	38.6
5	Mean	10.1	39.7	109.8	102.4	107.0	108.4	118.0	102.7	100.5	83.5	84.5	99.2	99.6	107.6	86.9
	S.D.	1.3	10.1	18.7	22.8	33.3	29.7	24.4	40.3	40.0	40.9	25.6	22.5	16.3	25.3	33.8
6	Mean	13.9	69.0	123.1	132.6	131.0	149.0	152.5	144.5	119.0	97.3	91.6	123.6	118.5	144.2	102.6
	S.D.	0.7	36.4	29.5	15.9	42.0	43.4	33.2	29.6	25.2	42.7	21.4	21.8	17.4	34.3	27.5
7	Mean	17.8	50.5	94.0	90.9	127.2	132.5	135.8	114.9	131.5	117.3	79.5	107.0	72.9	126.7	103.9
	S.D.	1.1	18.3	39.9	40.3	50.6	58.0	29.9	39.3	9.6	15.9	14.5	27.7	28.1	41.5	20.0

* global: slices 5% - 95%; posterior: slices 5% - 25%; lateral: slices 35% - 65%; anterior: slices 75% - 95%.

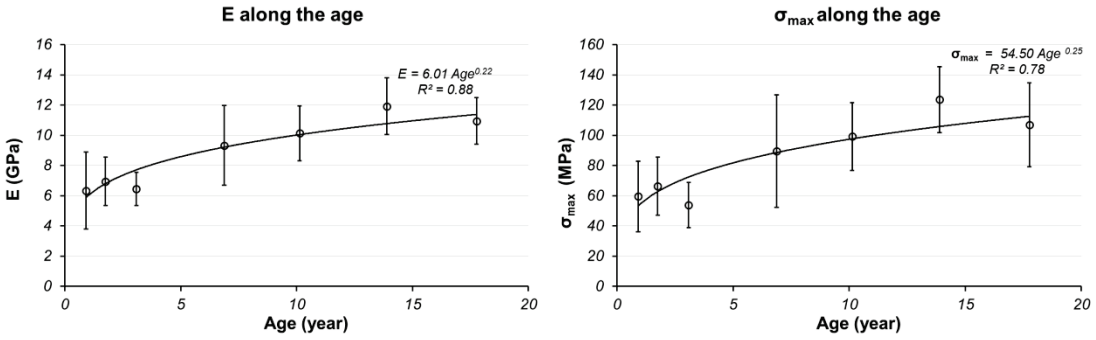

Figure 4.11: The predicted elastic properties (E) and maximal bending strength (σ_{max}) along age.

4.4 Discussion

This chapter firstly discussed about the phantoms, which were used to convert HU to BMD. Results showed that HU for a specific object can be changed due to different configurations. If scanned in a same and constant condition, the variation of HU can be less than 1 %. However, changing parameters (e.g. tube current and filter type) or performed in different CT devices can lead to approximately 5 % - 10 % variations of HU. Changing tube voltage can significantly change HU and it can lead to approximately 37.3 %. Thus, it is suggested to perform the scans with a calibration phantom each time, to get a more accurate value of BMD.

Based on the 47 scans with Phantom 062M on adult population, a global regression between HU and BMD were given out. However, using the unique regression to convert HU into BMD is risking. According to Figure 4.7, the calculated BMD using the global regression can lead to an average difference of approximately 20 % compared to the real BMD. It should be emphasized that this global regression was obtained from scans with the same tube voltage of 120 kVp. This result could be interesting for studies with non-calibrated images, e.g. Sandoz et al., 2013b. They obtained the variations of HU along the rib for child population based on non-calibrated images. If the CT images in their study were scanned with the tube voltage of 120 kVp, the HU could be converted to BMD (in mg HA/cm^3) using Equation (4-1). The error of this conversion could be approximately 20 %. However, this

convention might be only used for scans under 120 kVp, since different tube voltage can lead to a large variation of HU.

This is the first study which estimated material properties of pediatric rib cortical bones *in vivo*. Based on a methodology extracting rib cross-sectional images from clinical CT slices, which has been described by Sandoz et al., 2013b, and the relationships between BMD and material properties which were found on adult rib cortical bones, the elastic properties (E) and maximal bending strength (σ_{max}) of pediatric rib cortical bones were estimated. Previous studies explored material properties mainly relying on biomechanical tests on pediatric tissues. However, the paucity of pediatric tissues for biomechanical research was the main limitation. This study has overcome the drawback. This non-invasive method gives the opportunity to study material properties of pediatric rib cortical bones in a clinical environment and with a large population.

To our knowledge, the studies exploring material properties of pediatric rib cortical bones are rather few. Berteau et al., 2012 determined the material properties (Young's modulus and Poisson's ratio in transversal direction) of pediatric ribs through ultrasonic (US) measurements, with 12 rib segments harvested from two female subjects aged 15 and 17 years. They reported Young's modulus (E) of 14.1 and 15.4 GPa for the two subjects, respectively. Rib BMD were also assessed, however, they reported a mean value of 2 188 mg HA/cc, which were much higher compared with our study on human rib cortical bones and other studies on human cortical bones, but the reasons were unknown.

Agnew et al., 2013a and 2013b performed two studies involving pediatric ribs. They performed quasi-static (loading rate 0.042 mm/s) three-point bending tests on 44 rib sections collected from 12 subjects aged from 5 months to 9 years. They reported a mean Young's modulus of 4.9 GPa with a mean ultimate stress of 87.4 MPa, which are similar as the results in our study. The detailed results in Agnew et al., 2013a also allowed drawing a relationship between material properties and the age of the subjects, which can be compared with our study. Another study by Agnew et al., 2013b reported the effective stiffness of human ribs across the age. They showed a similar

effective stiffness of human ribs of the groups under 18 years and over 40 years. However, elastic modulus and ultimate stress were not calculated in that study. Combined these results with the findings in our study, a relationship between elastic properties and the age of the subjects can be compared. Figure 4.12 listed the elastic modulus of ribs and the age of the subjects. It should be noted that the methods to obtain the elastic modulus in these studies were different.

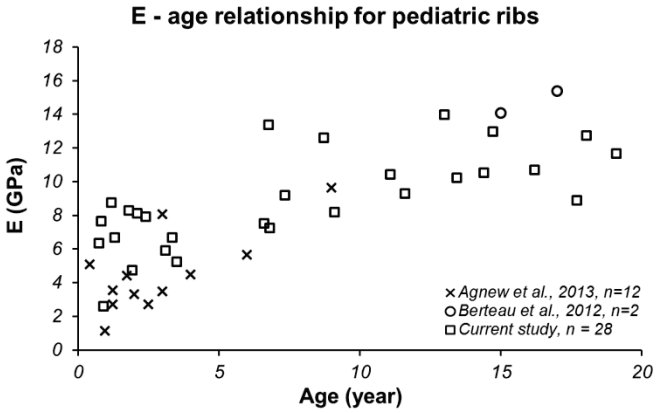

Figure 4.12: Elastic modulus of ribs and the age of the subjects, derived from Berteau et al., 2012, Agnew et al., 2013a and the current study.

The material properties varied along the rib, from vertebrae to sternum, resulting in higher values in lateral part compared to the anterior and posterior parts. Similar results have been reported by Stitzel et al., 2003 on adult ribs. They reported a higher average stiffness and ultimate stress in the lateral portion of ribs than the anterior and posterior regions. The Young's modulus and ultimate stress in the lateral portion (11.9 GPa, 153.5 MPa) of the ribs are significantly ($p = 0.0007$ and 0.0067) larger than those in the anterior (7.5 GPa, 116.7 MPa) and posterior (10.7 GPa, 127.7 MPa).

Combined previous studies exploring Elastic modulus – BMD relationships, it was found that the elastic modulus predicted in this study fit the cloud of points of Elastic modulus – BMD relationships on human femoral / tibial cortical bones. It might indicate that human cortical bones share a unique Elastic modulus – BMD relationship, as shown in Figure 4.13.

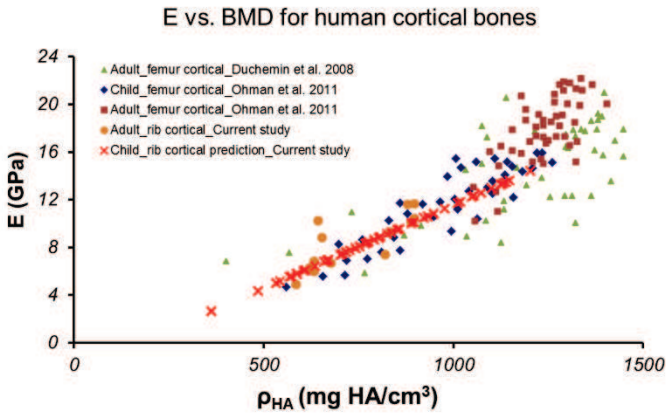

Figure 4.13: Elastic modulus and BMD relationships of human cortical bones, derived from Duchemin et al., 2008, Öhman et al., 2011 and Kaneko et al., 2003.

Some limitations should be discussed. First, the method used to extract rib cross sectional images from clinical CT slices was developed for an adult population. When it was applied to child population, the contours for cortical part were sometimes not reliable and need to correct manually, which might introduce error sometimes. In this study, less than 10% of the images need manual correction. Second, only the 6th rib of patients was calculated in this study. More ribs need to be studied and it will be interesting to investigate the variations of material properties of pediatric ribs along rib levels. Finally, the size of population can be extended to strengthen the results.

4.5 Conclusions

This study estimates the material properties of pediatric rib cortical bones *in vivo* for the first time. This non-invasive method overcame the drawback of the paucity of pediatric tissues for biomechanical research. The material properties were found higher in the lateral part of the ribs than the anterior and posterior regions. Material properties increase along age for the child population, and the relationships between material properties and age were given out in this study. Combined with previous studies on other cortical bones, it is suggested that human rib cortical bones share the Elastic modulus-BMD relationships with other cortical bones. This study opens the way to estimate material properties of pediatric cortical bones *in vivo*.

General conclusion

Pediatric trunk is one of the main injured body segments in case of a crash. The physical and numerical pediatric models are important tools to understand children's behavior during an impact. However, to develop or validate a pediatric model, biomechanical knowledge is still limited. This thesis aimed to provide more knowledge on mechanical behavior of the child *in vivo*, with particular attention to the trunk. A specific focus was made on the mechanical response of the trunk under loading and the mechanical properties of rib cortical bones.

The first chapter introduced the specific anatomical characteristics of children. There are considerable variations of anatomy and tissue properties for children during growth. Unlike adults, pediatric data can hardly be acquired directly from tests on cadavers or cadaveric tissues. To overcome this limitation, *in vivo* methods are expected for studies on children. Some methods which could be used to study biomechanical responses of children in clinical environments were proposed. Trunk compliance was previously assessed using force-deflection curves. However, such curves have been found different with each other. Do these differences come from the methods of the population? To answer this question, the goal of Chapter 2 was to explore the force-deflection characteristics of pediatric trunk under loading *in vivo*.

Chapter 2 quantified and explained the *in vivo* mechanical response of pediatric and adult trunks during respiratory physiotherapy. Time lags between force time histories and displacement time histories were observed on both children and adults. Different time lags resulted in different shapes of the force-displacement curves. Factors including respiration, muscle contraction and loading pattern are part of the assumptions used to explain this phenomenon. The maximum displacements of the pediatric and adult trunks were 18 mm and 44 mm, respectively, with a maximum load of 208 N and 250 N, respectively. Chapter 2 provided a better explanation of the peculiar force-displacement characteristics of both living and active children and adults under a non-injurious, low-rate compression condition.

For a better understanding of the mechanical responses of pediatric trunk, tissue property is also an important concern. Rib cortical bone is the main issue in this thesis. Non-invasive methods are valuable to study rib cortical bone mechanical properties for children. Previous studies have proved that bone mechanical properties are correlated to BMD, which can be measured by QCT *in vivo*. However, this method has not been applied to ribs. Thus, Chapter 3 explored this method ex vivo.

Chapter 3 provided significant relationships between mechanical properties of adult rib cortical bones and BMD measured by QCT and HR-pQCT. The BMD measured by HR-pQCT was significantly correlated to the elastic modulus and the ultimate bending strength of adult rib cortical bones (r^2 ranged from 0.48 to 0.75, $p < 0.01$), while the correlation between BMD measured by QCT and elastic modulus and the ultimate bending strength were little less strong (r^2 ranged from 0.22 to 0.50, $p < 0.08$). Compared with the results from literature, the BMD-mechanical properties relationships assessed by HR-pQCT on adult ribs meet the cloud of points for human femoral cortical bones. The BMD measured by QCT and HR-pQCT are different but linearly related. Since the BMD could be measured by QCT images scanned in a clinical environment, these linear relationships could be used to predict rib mechanical properties *in vivo*. This study is a first step towards the prediction of mechanical properties of pediatric rib cortical bones *in vivo*.

Chapter 4 mainly discussed about two issues. The first part of this chapter mainly studied the calibration phantoms, which were used to convert HU values of the QCT images to BMD. It was found that HU for a specific subject was not stable in different CT scan conditions. The variation of HU could be less than 1 % when scanned in the same conditions. The change of the CT devices and some parameters (tube current, filter type) could lead to approximately 7 % - 8 % variations of the HU. Tube voltage was the most sensitive parameter, since the change of tube voltage could lead to 37.3 % variations of HU. It suggested performing the scans with a calibration phantom each time, to get a more accurate value of BMD or to perform post-calibration for specific conditions. The second part of this chapter estimated the material properties of pediatric rib cortical bones *in vivo*. The material properties were found higher in the

lateral part of the ribs than the anterior and posterior regions. It was found that material properties increased along age for a child population, and the relationships between material properties and age were given out. The estimated material properties were comparable to previous studies. In addition, combined with other studies on human cortical bones, it is suggested that human rib cortical bones share the elastic modulus-BMD relationship with other cortical bones. This study estimated the material properties of pediatric rib cortical bones *in vivo* for the first time.

Some limitations should be discussed. First, for the mechanical response of pediatric trunk under loading, the studied force-displacement characteristics may not represent the real reaction of the trunk in the case of a crash since the rate of loading in this study was far lower than real crash rates. However, this study provided fundamental data regarding the mechanical response under non-injury, low-rate compression conditions. Second, BMD was proved to be a good predictor of the mechanical properties of rib cortical bones, both for adults and children. However, the BMD measured *in vivo* by QCT was not accurate enough compared to that measured *ex-vivo* by HR-pQCT, but this is the limitation of medical imaging techniques. Lastly, the sample size in this study can be enlarged. Obviously, more subjects could strengthen the results.

The results in this study could be helpful for child modeling. For example, the mechanical properties along age for child population could be guidance for scaling techniques. It is also interesting to study the sensitivity of pediatric numerical models using these new data on pediatric rib cortical bones. However, chest is a complex mechanism, besides ribs, the mechanical properties of cartilages or muscles are also important. Future works could be on mechanical properties of other tissues in the chest. All these data can contribute to child modeling, and models could be possibly developed directly with these data rather than scaling from adult data.

This study showed that mechanical behavior of the child population could be studied *in vivo*, through medical treatments or medical imaging techniques. This study opens the way of *in vivo* studies on child population. The non-invasive method in this study could be considered to apply on other anatomical sites of children.

Bibliography

Abdel-Aziz, Y. I., and Karara, H. M. (1971). *Direct linear transformation from comparator coordinates into object-space coordinate.* Paper presented at the ASP Symposium on Close-Range Photogrammetry, Falls Church.

Agnew, A. M., Kang, Y.-S., Moorhouse, K., Herriott, R., and IV, J. H. B. (2013a). *Age-related changes in stiffness in human ribs.* Paper presented at the IRCOBI Conference, Gothenburg, Sweden.

Agnew, A. M., Moorhouse, K., Kang, Y. S., Donnelly, B. R., Pfefferle, K., Manning, A. X., et al. (2013b). The response of pediatric ribs to quasi-static loading: mechanical properties and microstructure. *Ann Biomed Eng, 41*(12), 2501-2514.

Arbogast, K. B., Maltese, M. R., Nadkarni, V. M., Steen, P. A., and Nysaether, J. B. (2006). Anterior-posterior thoracic force-deflection characteristics measured during cardiopulmonary resuscitation: comparison to post-mortem human subject data. *Stapp Car Crash J, 50*, 131-145.

Arbogast, K. B., Mong, D. A., Marigowda, S., Kent, R. W., Stacey, S., Mattice, J., et al. (2005). *Evaluating pediatric abdominal injuries.* Paper presented at the 19th International Technical Conference on the Enhanced Safety of Vehicles.

Arbogast, K. B., Nishisaki, A., Balasubramanian, S., Nysaether, J., Niles, D., Sutton, R. M., et al. (2009). Expert clinical assessment of thorax stiffness of infants and children during chest compressions. *Resuscitation, 80*(10), 1187-1191.

Aubert, B., Vergari, C., Ilharreborde, B., Courvoisier, A., and Skalli, W. (2014). 3D reconstruction of rib cage geometry from biplanar radiographs using a statistical parametric model approach. *Computer Methods in Biomechanics and Biomedical Engineering: Imaging & Visualization*(ahead-of-print), 1-15.

Beillas, P., Alonzo, F., Chevalier, M.-C., Lesire, P., Leopold, F., Trosseille, X., et al. (2012). Abdominal twin pressure sensors for the assessment of abdominal injuries in q dummies: in-dummy evaluation and performance in accident reconstructions. *Stapp Car Crash Journal, 56*, 387-410.

Benameur, S., Mignotte, M., Destrempes, F., and De Guise, J. A. (2005). Three-dimensional biplanar reconstruction of scoliotic rib cage using the estimation of a mixture of probabilistic prior models. *Biomedical Engineering, IEEE Transactions on, 52*(10), 1713-1728.

Bermond, F., Bergeau, J., Alonzo, F., Goubel, C., Bruyère, K., Joffrin, P., et al. (2006). *Enhanced method and tools for child thoracic and abdominal compliance assessment by clinical treatments observation.* Paper presented at the Journal of Biomechanics.

Berteau, J. P., Pithioux, M., Follet, H., Guivier-Curien, C., Lasaygues, P., and Chabrand, P. (2012). Computed tomography, histological and ultrasonic measurements of adolescent scoliotic rib hump geometrical and material properties. *J Biomech, 45*(14), 2467-2471.

Beusenberg, M. C., Happee, R., Twisk, D., and Janssen, E. G. (1993). *Status of injury biomechanics for the development of child dummies.* Paper presented at the Child Occupant Protection Symposium, San Antonio, Texas, USA.

Bosisio, M. R., Talmant, M., Skalli, W., Laugier, P., and Mitton, D. (2007). Apparent Young's modulus of human radius using inverse finite-element method. *Journal of Biomechanics, 40*(9), 2022-2028.

Brown, J., Griffiths, M., and Paine, M. (2002). Effectiveness of child restraints: The Australian experience. *Australian New Car Assessment (ANCAP)*.

Brown, J. K., Jing, Y., Wang, S., and Ehrlich, P. F. (2006). Patterns of severe injury in pediatric car crash victims: Crash Injury Research Engineering Network database. *J Pediatr Surg, 41*(2), 362-367.

Burdi, A. R., Huelke, D. F., Snyder, R. G., and Lowrey, G. H. (1969). Infants and children in the adult world of automobile safety design: pediatric and anatomical considerations for design of child restraints. *J Biomech, 2*(3), 267-280.

Burghardt, A. J., Buie, H. R., Laib, A., Majumdar, S., and Boyd, S. K. (2010). Reproducibility of direct quantitative measures of cortical bone microarchitecture of the distal radius and tibia by HR-pQCT. *Bone, 47*(3), 519-528.

Burstein, A. H., Currey, J. D., Frankel, V. H., and Reilly, D. T. (1972). The ultimate properties of bone tissue: the effects of yielding. *Journal of Biomechanics, 5*(1), 35-44.

CDCP. (2006). *CDC's Injury Fact Book*. Atlanta: Center for Disease Control and Prevention.

Charpail, E. (2006). *Analyse du comportement mécanique des côtes humaines en dynamique.* Arts et Métiers ParisTech.

Charpail, E., Trosseille, X., Petit, P., Laporte, S., Lavaste, F., and Vallancien, G. (2005). Characterization of PMHS Ribs: A New Test Methodology. *Stapp Car Crash J, 49*, 183-198.

Cormier, J. M., Stitzel, J. D., Duma, S. M., and Matsuoka, F. (2005). *Regional variation in the structural response and geometrical properties of human ribs.* Paper presented at the Annual Proceedings/Association for the Advancement of Automotive Medicine.

Crandall, J. R., Myers, B. S., Meaney, D. F., and Schmidtke, S. Z. (2013). *Pediatric Injury Biomechanics* (Vol. 1).

Dansereau, J., and Stokes, I. A. (1988). Measurements of the three-dimensional shape of the rib cage. *J Biomech, 21*(11), 893-901.

de Jager, K., van Ratingen, M., Lesire, P., Guillemot, H., Pastor, C., Schnottale, B., et al. (2005). *Assessing new child dummies and criteria for child occupant protection in frontal impact.* Paper presented at the 19th ESV conference. TNO–LAB–BASt–IDIADA–UTAC.

Demont, B., Vincon, C., Bailleux, S., Cambas, C. H., Dehan, M., and Lacaze-Masmonteil, T. (2007). Chest physiotherapy using the expiratory flow increase procedure in ventilated newborns: a pilot study. *Physiotherapy, 93*(1), 12-16.

Dempster, W. T., and Liddicoat, R. T. (1952). Compact bone as a non‐isotropic material. *American Journal of Anatomy, 91*(3), 331-362.

Duchemin, L., Bousson, V., Raossanaly, C., Bergot, C., Laredo, J. D., Skalli, W., et al. (2008). Prediction of mechanical properties of cortical bone by quantitative computed tomography. *Med Eng Phys, 30*(3), 321-328.

ERF. (2012). European Road Statistics 2012.

European-Commission. (2013). Mobility and transport, Road safety. from http://ec.europa.eu/transport/road_safety/users/children/index_en.htm

Forman, J. (2009). *The structural characteristics of the costal cartilage: the roles of calcification and the perichondrium, and the representation of the costal cartilage in finite element models of the human body.* (P.h.D P.h.D thesis), University of Virginia. (440)

Franklin, A. (2007). Human-nonhuman animal relationships in Australia: An overview of results from the first national survey and follow-up case studies 2000-2004. *Society & Animals, 15*(1), 7-27.

Franklyn, M., Peiris, S., Huber, C., and Yang, K. H. (2007). Pediatric material properties: a review of human child and animal surrogates. *Crit Rev Biomed Eng, 35*(3-4), 197-342.

Funk, J. R., Kerrigan, J. R., and Crandall, J. (2004). *Dynamic bending tolerance and elastic-plastic material properties of the human femur.* Paper presented at the Annual Proceedings/Association for the Advancement of Automotive Medicine.

Granik, G., and Stein, I. (1973). Human ribs: static testing as a promising medical application. *Journal of Biomechanics, 6*(3), 237-240.

Gray, H. (1918). *Anatomy of the human body*: Lea & Febiger.

Halperin, H. R., and Berger, R. D. (2002). CPR chest compression monitor: Google Patents.

Hammer, J., and Eber, E. (2005). The peculiarities of infant respiratory physiology. *Prog Respir Res., 33*, 2-7.

Helgason, B., Perilli, E., Schileo, E., Taddei, F., Brynjólfsson, S., and Viceconti, M. (2008). Mathematical relationships between bone density and mechanical properties: A literature review. *Clinical Biomechanics, 23*(2), 135-146.

Hildebrand, T., Laib, A., Müller, R., Dequeker, J., and Rüegsegger, P. (1999). Direct Three‐Dimensional Morphometric Analysis of Human Cancellous Bone: Microstructural Data from Spine, Femur, Iliac Crest, and Calcaneus. *Journal of Bone and Mineral Research, 14*(7), 1167-1174.

Hoffman, E. J., Huang, S. C., and Phelps, M. E. (1979). Quantitation in positron emission computed tomography: 1. Effect of object size. *J Comput Assist Tomogr, 3*(3), 299-308.

Hvid, I., Bentzen, S. M., Linde, F., Mosekilde, L., and Pongsoipetch, B. (1989). X-ray quantitative computed tomography: the relations to physical properties of proximal tibial trabecular bone specimens. *Journal of Biomechanics, 22*(8), 837-844.

Jiang, B., Cao, L., Mao, H., Wagner, C., Marek, S., and Yang, K. H. (2012). Development of a 10-year-old paediatric thorax finite element model validated against cardiopulmonary resuscitation data. *Comput Methods Biomech Biomed Engin*.

Kallieris, D., Barz, J., Schmidt, G., Heess, G., and Mattern, R. (1976). *Comparison between child cadavers and child dummy by using child restraint systems in simulated collisions.* Paper presented at the 20th Stapp Car Crash Conference, Dearborn, Michigan, USA.

Kaneko, T. S., Pejcic, M. R., Tehranzadeh, J., and Keyak, J. H. (2003). Relationships between material properties and CT scan data of cortical bone with and without metastatic lesions. *Medical engineering & physics, 25*(6), 445-454.

Kapoor, T., Altenhof, W., Snowdon, A., Howard, A., Rasico, J., Zhu, F., et al. (2011). A numerical investigation into the effect of CRS misuse on the injury potential of children in frontal and side impact crashes. *Accident Analysis & Prevention, 43*(4), 1438-1450.

Keller, T. S. (1994). Predicting the compressive mechanical behavior of bone. *J Biomech, 27*(9), 1159-1168.

Kemper, A. R., McNally, C., Kennedy, E. A., Manoogian, S. J., Rath, A. L., Ng, T. P., et al. (2005). Material properties of human rib cortical bone from dynamic tension coupon testing. *Stapp Car Crash J, 49*, 199-230.

Kemper, A. R., McNally, C., Pullins, C. A., Freeman, L. J., Duma, S. M., and Rouhana, S. M. (2007). The biomechanics of human ribs: material and structural properties from dynamic tension and bending tests. *Stapp Car Crash J, 51*, 235-273.

Kent, R., Lee, S. H., Darvish, K., Wang, S., Poster, C. S., Lange, A. W., et al. (2005). Structural and material changes in the aging thorax and their role in crash protection for older occupants. *Stapp Car Crash J, 49*, 231-249.

Kent, R., Lessley, D., and Sherwood, C. (2004). Thoracic response to dynamic, non-impact loading from a hub, distributed belt, diagonal belt, and double diagonal belts. *Stapp Car Crash J, 48*, 495-519.

Kent, R., Lopez-Valdes, F. J., Lamp, J., Lau, S., Parent, D., Kerrigan, J., et al. (2011, June 13-16). *Characterization of the pediatic chest and abdomen using three post-mortem human subjects.* Paper presented at the 22nd International Technical Conference on the Enhanced Safety of Vehicles (ESV), Washington, D.C.

Kent, R., Salzar, R., Kerrigan, J., Parent, D., Lessley, D., Sochor, M., et al. (2009). Pediatric thoracoabdominal biomechanics. *Stapp Car Crash J, 53*, 373-401.

Kent, R., Stacey, S., Kinding, M., Forman, J., and Woods, W. (2006). Biomechanical response of the pediatric abdomen, Part 1: Development of an experimental model and quantification of structural response to dynamic belt loading. *Stapp Car Crash Journal, 50*, 1-26.

Keyak, J., Meagher, J., Skinner, H., and Mote Jr, C. (1990). Automated three-dimensional finite element modelling of bone: a new method. *Journal of biomedical engineering, 12*(5), 389-397.

Kopperdahl, D. L., Morgan, E. F., and Keaveny, T. M. (2002). Quantitative computed tomography estimates of the mechanical properties of human vertebral trabecular bone. *J Orthop Res, 20*(4), 801-805.

Kroell, C. K., Allen, S. D., Warner, C. Y., and Perl, T. R. (1986). *Interrelationship of velocity and chest compression in blunt thoracic impact to Swine II.* Paper presented at the 30th Stapp Car Crash Conference, San Diego, California, USA.

Kroell, C. K., Pope, M. E., Viano, D. C., Warner, C. Y., and Allen, S. D. (1981). *Interrelationship of velocity and chest compression in blunt thoracic impact to swine.* Paper presented at the 25th Stapp Car Crash Conference, San Francisco, California, USA.

Lakes, R. S., Katz, J. L., and Sternstein, S. S. (1979). Viscoelastic properties of wet cortical bone--I. Torsional and biaxial studies. *J Biomech, 12*(9), 657-678.

Lau, A., Oyen, M. L., Kent, R. W., Murakami, D., and Torigaki, T. (2008). Indentation stiffness of aging human costal cartilage. *Acta biomaterialia, 4*(1), 97-103.

Li, Z., Kindig, M. W., Subit, D., and Kent, R. W. (2010). Influence of mesh density, cortical thickness and material properties on human rib fracture prediction. *Med Eng Phys, 32*(9), 998-1008.

Lobdell, T., Kroell, C., Schneider, D., Hering, W., and Nahum, A. (1973). Impact response of the human thorax. *Human Impact Response Measurement and Simulation*, 201-245.

Maltese, M. R., Castner, T., Niles, D., Nishisaki, A., Balasubramanian, S., Nysaether, J., et al. (2008). Methods for determining pediatric thoracic force-deflection characteristics from cardiopulmonary resuscitation. *Stapp Car Crash J, 52*, 83-105.

Marechal, L., Barthod, C., Lottin, J., Gautier, G., and Jeulin, J. C. (2007). Measurement system for gesture characterization during chest physiotherapy

act on newborn babies suffering from bronchiolitis. *Conf Proc IEEE Eng Med Biol Soc, 2007*, 5771-5774.

Melvin, J. W., Stalnaker, R. L., and Mohan, D. (1978). *Protection of child occupants in automobile crashes*. Paper presented at the Proceedings: Stapp Car Crash Conference.

MindwaysSoftwareInc. (2005). QCT PRO™ Bone Mineral Densitometry Software Phantom Module (Version 4.0).

Mitton, D., Minonzio, J.-G., Talmant, M., Ellouz, R., Rongieras, F., Laugier, P., et al. (2014). non-destructive assessment of human rib mechanical properties using quantitative ultrasound. *J Biomech, in press*.

Mitton, D., Zhao, K., Bertrand, S., Zhao, C., Laporte, S., Yang, C., et al. (2008). 3D reconstruction of the ribs from lateral and frontal X-rays in comparison to 3D CT-scan reconstruction. *J Biomech, 41*(3), 706-710.

Mizuno, K., Iwata, K., Deguchi, T., Ikami, T., and Kubota, M. (2005). Development of a three-year-old child FE model. *Traffic Inj Prev, 6*(4), 361-371.

Mohr, M., Abrams, E., Engel, C., Long, W. B., and Bottlang, M. (2007). Geometry of human ribs pertinent to orthopedic chest-wall reconstruction. *J Biomech, 40*(6), 1310-1317.

Moore, K. L., Dalley, A. F., and Agur, A. M. (2013). *Clinically oriented anatomy*: Wolters Kluwer Health.

MPSTA. (2013). Statistics of road traffic accidents of china (in chinese): the Ministry of Public Security Traffic Administration.

Nahum, A. M., and Schneider, D. C. (1975). Cadaver skeletal response to blunt thoracic impact.

NHTSA. (2013). Traffic Safety Facts. *DOT HS 811 767*.

Niles, D. E., Nishisaki, A., Sutton, R. M., Nysaether, J., Eilevstjonn, J., Leffelman, J., et al. (2012). Comparison of relative and actual chest compression depths during cardiac arrest in children, adolescents, and young adults. *Resuscitation, 83*(3), 320-326.

Nishisaki, A., Nysaether, J., Sutton, R., Maltese, M., Niles, D., Donoghue, A., et al. (2009). Effect of mattress deflection on CPR quality assessment for older children and adolescents. *Resuscitation, 80*(5), 540.

Öhman, C., Baleani, M., Pani, C., Taddei, F., Alberghini, M., Viceconti, M., et al. (2011). Compressive behaviour of child and adult cortical bone. *Bone*, 769-776.

ONISR. (2012). Bilan de l'accidentalité de l'année 2012.

Openshaw, P., Edwards, S., and Helms, P. (1984). Changes in rib cage geometry during childhood. *Thorax, 39*(8), 624-627.

Ouyang, J., Zhao, W., Xu, Y., Chen, W., and Zhong, S. (2006). Thoracic impact testing of pediatric cadaveric subjects. *J Trauma, 61*(6), 1492-1500.

Perrotta, C., Ortiz, Z., and Roque, M. (2005). Chest physiotherapy for acute bronchiolitis in paediatric patients between 0 and 24 months old. *Cochrane Database Syst Rev*(2), CD004873.

Perz, R., Toczyski, J., Kindig, M., Ito, D., Ejima, S., Kamiji, K., et al. (2013). *Evaluation of the geometrical properties distribution along the human ribs using different X-Ray imaging methods.* Paper presented at the IRCOBI Conference, Gothenburg, Sweden.

Pezowicz, C., and Glowacki, M. (2012). The mechanical properties of human ribs in young adult. *Acta of Bioengineering & Biomechanics, 14*(2).

Pfefferle, K., Litsky, A., Donnelly, B., and Bolte IV, J. (2007). *Biomechanical properties of the excised pediatric human rib.* Paper presented at the Injury Biomechanics Research: Proceedings of the Thirty-fifth International Workshop.

Reilly, D. T., Burstein, A. H., and Frankel, V. H. (1974). The elastic modulus for bone. *J Biomech, 7*(3), 271-275.

Rho, J. Y., Hobatho, M. C., and Ashman, R. B. (1995). Relations of mechanical properties to density and CT numbers in human bone. *Med Eng Phys, 17*(5), 347-355.

Roque i Figuls, M., Gine-Garriga, M., Granados Rugeles, C., and Perrotta, C. (2012). Chest physiotherapy for acute bronchiolitis in paediatric patients between 0 and 24 months old. *Cochrane Database Syst Rev, 2*, CD004873.

Roth, S., Raul, J.-S., and Willinger, R. (2008). Biofidelic child head FE model to simulate real world trauma. *Computer methods and programs in biomedicine, 90*(3), 262-274.

Sandoz, B., Badina, A., Laporte, S., Lambot, K., Mitton, D., and Skalli, W. (2013a). Quantitative geometric analysis of rib, costal cartilage and sternum from childhood to teenagehood. *Med Biol Eng Comput, 51*(9), 971-979.

Sandoz, B., Sidelkeir, Z., Badina, A., Bermond, F., Mitton, D., and Skalli, W. (2013b). *Variability of child rib bone hounsfield units using in vivo computed tomography.* Paper presented at the IRCOBI Conference, Gothenburg, Sweden.

Sandoz, B., Vajda, E., Alonzo, F., Bruyere, K., and Bermond, F. (2011). The mechanics of the in vivo infant and toddler trunk during respiratory physiotherapy. *Clin Biomech (Bristol, Avon), 26*(6), 535-542.

Stitzel, J. D., Cormier, J. M., Barretta, J. T., Kennedy, E. A., Smith, E. P., Rath, A. L., et al. (2003). Defining regional variation in the material properties of human rib cortical bone and its effect on fracture prediction. *Stapp Car Crash Journal, 47*, 243-265.

Stürtz, G. (1980). Biomechanical Data of Children. In SAE (Ed.). Stuttgart, Germany.

Subit, D., de Dios, E. d. P., Valazquez-Ameijide, J., Arregui-Dalmases, C., and Crandall, J. (2013). Tensile material properties of human rib cortical bone

under quasi-static and dynamic failure loading and influence of the bone microstucture on failure characteristics. *arXiv preprint arXiv:1108.0390*.

Suzuki, S., Yamamuro, T., Okumura, H., and Yamamoto, I. (1991). Quantitative computed tomography: comparative study using different scanners with two calibration phantoms. *The British journal of radiology, 64*(767), 1001-1006.

Trosseille, X., Cassan, F., and Schrooten, M. (2001). *Child restraint system for children in cars—CREST results.* Paper presented at the Proceedings of 17th Enhanced Safety of Vehicles Conference.

Verzin, P., and Berthet, F. (2009). Structural characterization of human rib cage behavior under dynamic loading. *Stapp Car Crash J, 53*, 93-125.

Viano, D. C., and Lau, I. V. (1988). A viscous tolerance criterion for soft tissue injury assessment. *J Biomech, 21*(5), 387-399.

Vose, G. P., and KUBALA, A. L. (1959). Bone strength—its relationship to x-ray-determined ash content. *Human Biology, 31*(3), 261-270.

WHO. (2013). *WHO global status report on road safety 2013: supporting a decade of action*: World Health Organization.

Will, K. E., and Geller, E. S. (2004). Increasing the safety of children's vehicle travel: from effective risk communication to behavior change. *Journal of Safety Research, 35*(3), 263-274.

Yamada, H., and Evans, F. G. (1970). *Strength of biological materials* (Vol. 1000): Williams & Wilkins Baltimore.

Yoganandan, N., and Pintar, F. A. (1998). Biomechanics of human thoracic ribs. *J Biomech Eng, 120*(1), 100-104.

Zhu, Y., Bruyère-Garnier, K., Mitton, D., Vajda, E., and Bermond, F. (2014). Mechanical behaviour of the in vivo paediatric and adult trunk during respiratory physiotherapy. *Proceedings of the Institution of Mechanical Engineers, Part H: Journal of Engineering in Medicine, 228*(1), 27-36.

Appendix 1: Mechanical property of adult rib cortical bones based on three-point bending tests

The material properties of the 13 rib segments have been published in Mitton et al., 2014 and these data was introduced in this study. The methods to obtain these data are described here.

Three-point bending experiments were performed until failure on each rib segment using a servo-hydraulic testing machine (INSTRON 8802, High Wycombe, England), as shown in Figure A.1. The main points are recalled in the following. The specimen was placed centered on two rotatable supporters spaced by 10 cm. The upper nose with cylindrical surface applied load centered on the specimen with a speed of 0.5 m/s. Tests were performed in room temperature. Load and displacement were recorded by a load cell (accuracy 0.5 %) and the testing machine displacement transducer (accuracy 1 %), respectively.

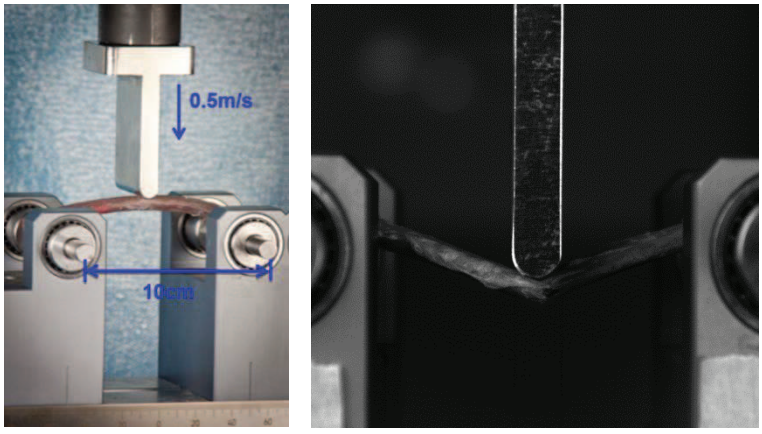

Figure A.1: Left: three-point bending experiment on rib segments; Right: the specimens were tested until failure, recorded by a high speed camera.

The elastic modulus (E) and the maximal bending strength (σ_{max}) were calculated in two ways:

1. Analytical approach. Assuming that the specimen can be deemed as a linear elastic beam with constant cross sections, using Equations (A-1) and (A-2).

$$E_a = K\frac{L^3}{48\,I} \qquad \text{(A-1)}$$

$$\sigma_{max\,a} = \frac{F_{max}}{4\,Z}L \qquad \text{(A-2)}$$

Where E_a is analytical modulus of elasticity; K is effective stiffness which can be obtained from force-displacement curves; L is the span length and it is 10 cm in this study; I is cross sectional area moment of inertia, which is reported by HR-pQCT measurements; $\sigma_{max\,a}$ is analytical maximal bending strength; F_{max} is the maximum load; Z is the section modulus, which is reported by HR-pQCT measurements, and it could also be expressed as I/c, where c is distance from the neutral axis.

2. Numerical approach. Using an inverse approach combining a finite-element (FE) model of the rib and the load-displacement curve from the corresponding three-point bending experiment (Bosisio et al., 2007; Mitton et al., 2014).

For each rib, a FE model was built by Hypermesh (HyperWorks, Altair, USA). The geometrical data of the model was derived from HR-pQCT measurements. The rib was defined as a shell with a thickness of corresponding mean cortical thickness derived from HR-pQCT, and the internal part is composed of solid elements representing the trabecular bone. The mechanical properties of the trabecular bone were derived from literature and kept constant since they have negligible influence on the rib response (Li et al., 2010). The rotatable supporters and the loading nose are defined as rigid cylinders. Simulations were performed by LS-DYNA (LSTC, USA). The elastic modulus and the maximal bending strength of the rib cortical bone were adapted manually, to fit the force-displacement curve in the simulation to that of the corresponding experiment. Simulations were performed until a difference below 5 % of the stiffness (the slope of the force/displacement) and the maximum force. The elastic modulus (E_n) and the maximal bending strength ($\sigma_{max\,n}$) of the specimen were identified with this inverse approach. Figure A.2 illustrates the FE model simulation and the force-displacement curves in the experiment and the simulations.

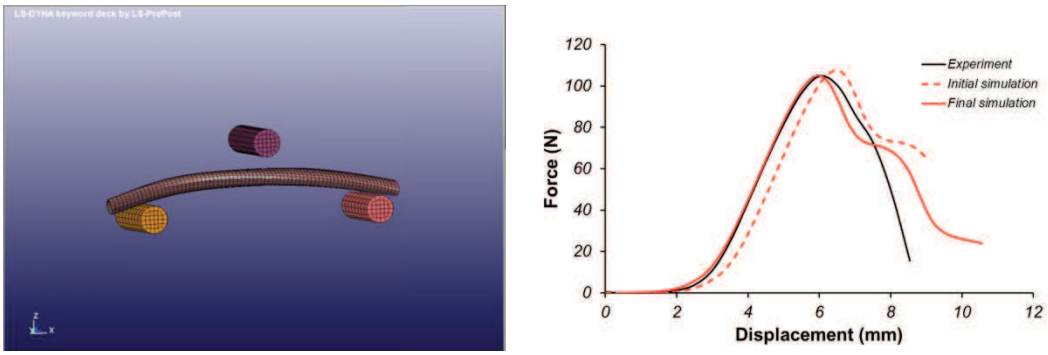

Figure A.2: Left: FE model simulation of a rib segment; Right: force-displacement curves from the experiment and the simulations.

Appendix 2: The BMD along the rib obtained by QCT and the BMD of rib specimens measured by HR-pQCT

Here lists the BMD along the rib obtained by QCT (left) and the BMD along the rib specimens measured by HR-pQCT (right). However, the accurate location of the 120 mm rib specimen analyzed by HR-pQCT is not known inside the full associated rib. Thus, the evolution of the density in the following graphs cannot be compared.

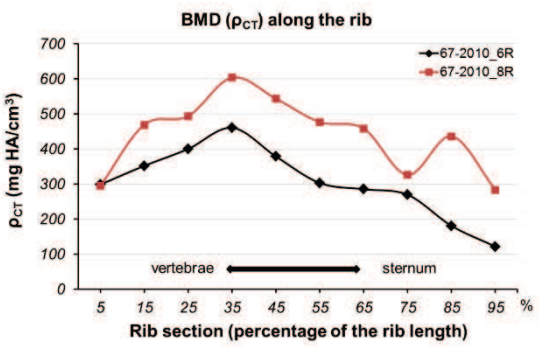

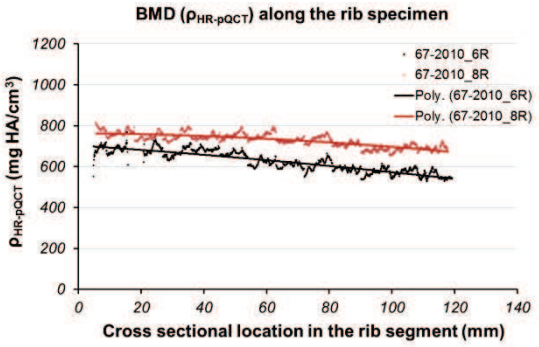

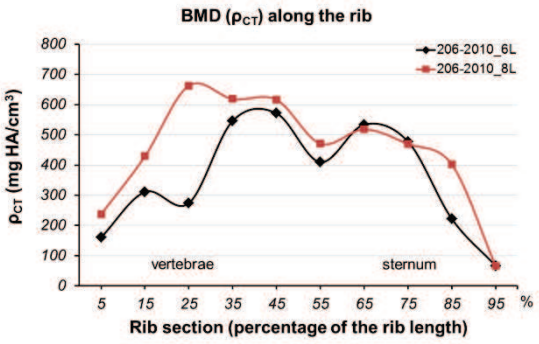

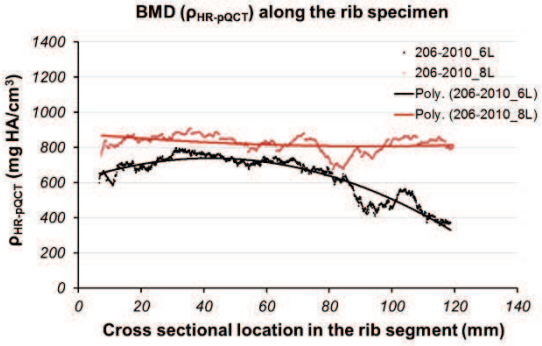

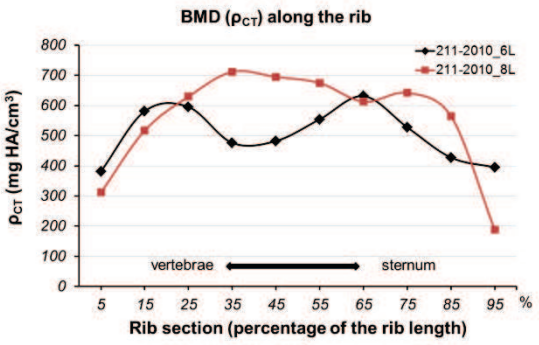

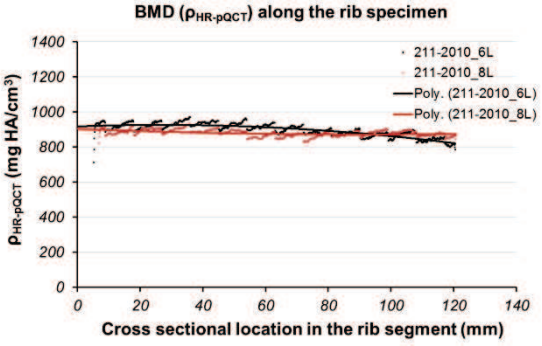

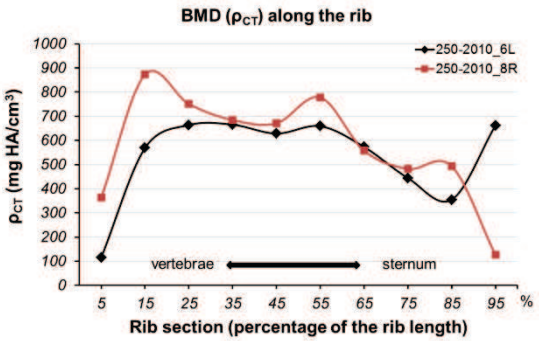
BMD (ρ_{CT}) along the rib
250-2010_6L
250-2010_8R
ρ_{CT} (mg HA/cm³)
vertebrae
sternum
Rib section (percentage of the rib length)

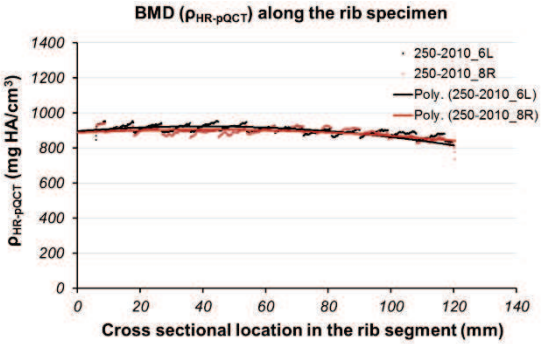
BMD ($\rho_{HR\text{-}pQCT}$) along the rib specimen
250-2010_6L
250-2010_8R
Poly. (250-2010_6L)
Poly. (250-2010_8R)
$\rho_{HR\text{-}pQCT}$ (mg HA/cm³)
Cross sectional location in the rib segment (mm)

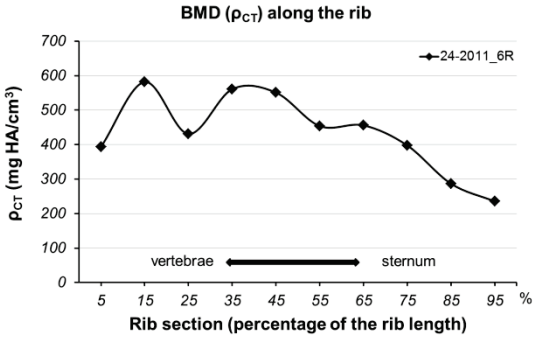
BMD (ρ_{CT}) along the rib
24-2011_6R
ρ_{CT} (mg HA/cm³)
vertebrae
sternum
Rib section (percentage of the rib length)

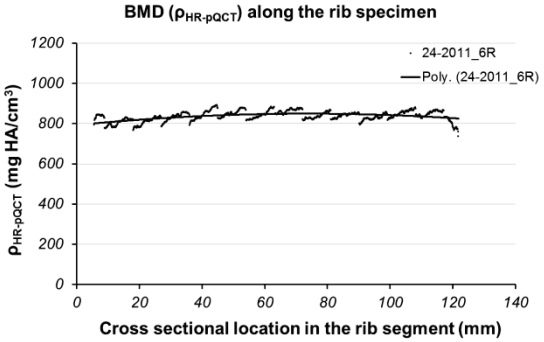
BMD ($\rho_{HR\text{-}pQCT}$) along the rib specimen
24-2011_6R
Poly. (24-2011_6R)
$\rho_{HR\text{-}pQCT}$ (mg HA/cm³)
Cross sectional location in the rib segment (mm)

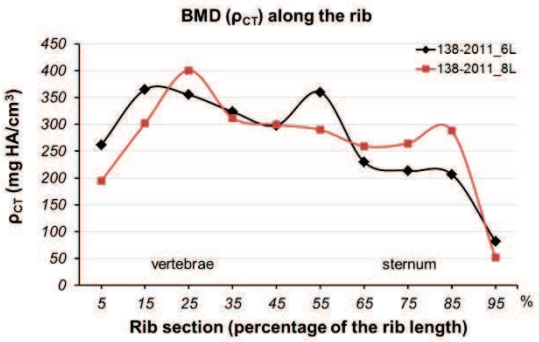
BMD (ρ_{CT}) along the rib
138-2011_6L
138-2011_8L
ρ_{CT} (mg HA/cm³)
vertebrae
sternum
Rib section (percentage of the rib length)

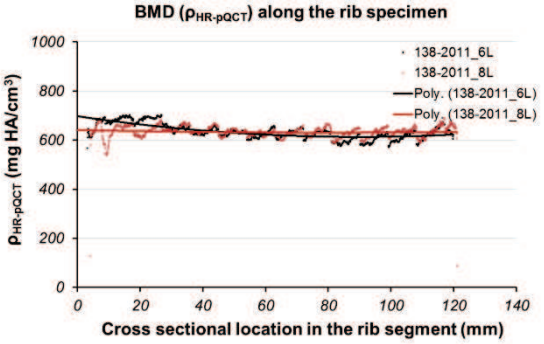
BMD ($\rho_{HR\text{-}pQCT}$) along the rib specimen
138-2011_6L
138-2011_8L
Poly. (138-2011_6L)
Poly. (138-2011_8L)
$\rho_{HR\text{-}pQCT}$ (mg HA/cm³)
Cross sectional location in the rib segment (mm)

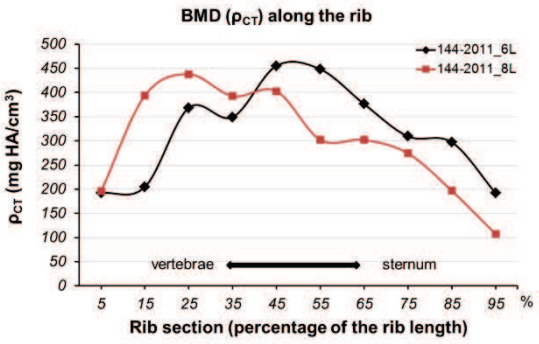
BMD (ρ_{CT}) along the rib
144-2011_6L
144-2011_8L
ρ_{CT} (mg HA/cm³)
vertebrae
sternum
Rib section (percentage of the rib length)

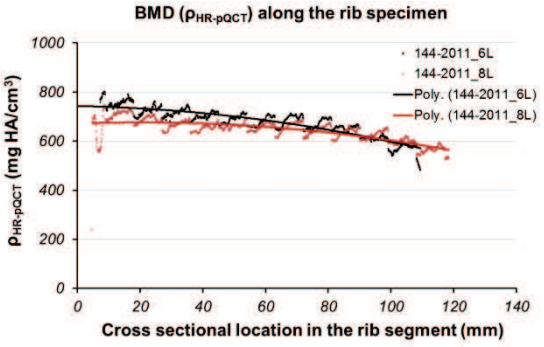
BMD ($\rho_{HR\text{-}pQCT}$) along the rib specimen
144-2011_6L
144-2011_8L
Poly. (144-2011_6L)
Poly. (144-2011_8L)
$\rho_{HR\text{-}pQCT}$ (mg HA/cm³)
Cross sectional location in the rib segment (mm)

Appendix 3: Summary in French

A3.1 Introduction

Les accidents de voitures sont l'une des principales causes de décès et de blessures pour les enfants partout dans le monde (WHO, 2013). En cas d'accident, le tronc (thorax et abdomen) est l'une des principales régions blessées chez les enfants (Crandall et al., 2013). Ainsi, cette étude se concentrera sur le tronc de l'enfant.

Des efforts de recherche sont menés dans le domaine de la biomécanique de l'enfant pour la sécurité routière. Pour mieux comprendre le comportement biomécanique de l'enfant, diverses recherches ont été faites telles que des expérimentations avec des sujets d'anatomie (Kallieris et al., 1976; Kent et al., 2011; Kent et al., 2009; Ouyang et al., 2006), des expérimentations avec des modèles animaux (Arbogast et al., 2005; Kent et al., 2006), des observations sur des volontaires dans le domaine infra lésionnel (Sandoz et al., 2011), etc. Toutefois, les études sur les enfants sont limitées par rapport à celles sur les adultes (Franklyn et al., 2007). Les matériaux biologiques des enfants sont difficiles à recueillir limitant les expérimentations pouvant être réalisées.

La rareté des données sur l'enfant a conduit à l'élaboration de modèles de l'enfant par mise à l'échelle des données à partir de celle concernant les adultes. Les enfants diffèrent des adultes non seulement pour les caractéristiques géométriques, mais aussi en ce qui concerne les propriétés mécaniques des tissus. Les structures anatomiques, les propriétés des matériaux, les mécanismes de blessures et les tolérances associées, des enfants peuvent changer considérablement en fonction de l'âge par rapport à celles des adultes. Par conséquent, il y a un besoin de données spécifiques pour les enfants.

L'objectif principal de ce manuscrit est d'explorer la biomécanique du tronc de l'enfant en utilisant des approches non - invasives. Pour atteindre cet objectif, le premier chapitre présente une revue de la littérature de la biomécanique du tronc de l'enfant sous chargement et des propriétés mécaniques de l'os cortical des côtes de

l'enfant. Après une brève description anatomique du thorax et de la croissance de l'enfant, ce chapitre détaille les études sur le comportement biomécanique du tronc de l'enfant grâce à des expérimentations sur sujets d'anatomie et des essais de chargement *in vivo*. Ensuite, les expériences sur les côtes humaines, y compris celles de l'enfant, sont introduites pour identifier les propriétés mécaniques. Enfin, les études portant sur les relations entre les propriétés mécaniques et la densité osseuse sont décrites pour discuter de la méthode qui peut être éventuellement utilisée pour étudier les propriétés mécaniques des côtes *in vivo*.

Après cette revue de la littérature, des questions se posent:

- Le comportement du tronc de l'enfant a déjà été évalué à l'aide des courbes de force en fonction du déplacement. Toutefois, ces courbes présentent une variabilité. Ces différences proviennent-elles des méthodes utilisées ou de la population ?
- Certaines études ont montré que les propriétés mécaniques osseuses sont en corrélation avec la densité minérale osseuse (DMO). Cependant, les relations n'ont pas été étudiées sur l'os cortical des côtes. Existe-t-il des relations similaires entre les propriétés mécaniques et la DMO sur les côtes de l'homme ?
- Les relations entre les propriétés mécaniques et la DMO peuvent-elles être appliquées à la population des enfants, pour estimer les propriétés mécaniques de la côte de l'enfant en fonction de la DMO mesurée *in vivo* ?

Pour répondre à ces questions, ce manuscrit se concentre sur les réponses mécaniques du tronc de l'enfant et les propriétés mécaniques de l'os cortical. Il est composé des parties suivantes :

- Le **Chapitre 2** porte sur les réponses mécaniques du tronc de l'enfant. Les relations de force en fonction du déplacement de tronc humain, à la fois des enfants et des adultes, sont observées. Certaines hypothèses sont formulées pour expliquer les différences entre ses deux populations. Pour une meilleure compréhension des réponses mécaniques du tronc de l'enfant, les propriétés des tissus sont également une problématique importante.

- **Le Chapitre 3** traite des propriétés mécaniques des tissus. Il vise à observer les relations entre les propriétés mécaniques de l'os cortical des côtes et la DMO de l'adulte. Deux modalités différentes de rayons X sont présentées pour mesurer la DMO, et les résultats sont comparés. Comme la DMO des côtes de l'enfant peut être mesurée *in vivo*, ce chapitre ouvre la voie à l'estimation des propriétés mécaniques de l'os cortical des côtes de l'enfant *in vivo*.
- **Le Chapitre 4** estime les propriétés mécaniques de l'os cortical des côtes de l'enfant sur la base de la DMO mesurée *in vivo*. Les propriétés mécaniques de côtes selon l'âge sont également présentées.
- La conclusion générale soulignées résultats principaux apportés par cette thèse et présente les perspectives ouvertes notamment pour la modélisation des enfants.

A3.2 Le Chapitre 1 : Etat de l'art

Ce chapitre souligne l'importance de la protection des enfants dans les accidents de la route. En cas d'accident, le tronc est l'un des principaux segments corporels blessé (Crandall et al., 2013), et cette thèse se concentrera sur le tronc pédiatrique. Pour construire ou valider un modèle pédiatrique, les principales limitations sont liées au faible nombre des données pédiatriques. Une meilleure connaissance du tronc pédiatrique, y compris la réponse mécanique et les propriétés des tissus est attendue.

La deuxième partie de ce chapitre présente les caractéristiques anatomiques spécifiques des enfants. Il existe des variations considérables d'anatomie et de propriétés mécaniques pour les enfants en cours de croissance. Pour développer un modèle pédiatrique de haute biofidélité, les données anatomiques et les propriétés mécaniques apparaissent essentielles. Toutefois, les données pédiatriques existantes sont basées principalement sur la mise à l'échelle de celles des adultes. La technique de mise à l'échelle, largement utilisée pour la modélisation pédiatrique, présente certaines limitations.

Contrairement aux adultes, les données pédiatriques peuvent difficilement être obtenues directement à partir d'essais sur des cadavres ou des tissus provenant de

cadavres. En effet, seuls quatre expérimentations post-mortem sur le tronc pédiatrique ont été reportés jusqu'à présent dans la littérature (Kallieris et al., 1976; Kent et al., 2011; Kent et al., 2009; Ouyang et al., 2006).

Pour contourner cette limitation, des méthodes *in vivo* présentent a priori un potentiel. Certaines méthodes qui pourraient être utilisées pour étudier les réponses biomécaniques des enfants dans des environnements cliniques ont été proposées.

La réponse mécanique du tronc a déjà été évaluée à l'aide des courbes force-déplacement (Maltese et al., 2008). Toutefois, ces courbes présentent une variabilité. Ces différences proviennent-elles des méthodes utilisées? Pour répondre à cette question, le premier objectif de cette thèse est d'étudier les caractéristiques de force - déplacement de tronc pédiatrique sous chargement *in vivo*.

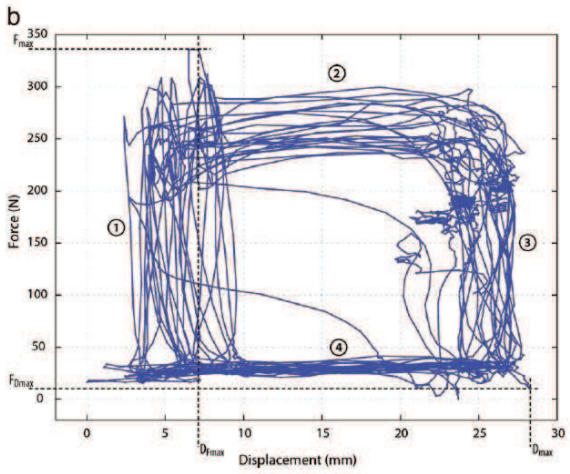

Figure A3.1: Relations force-déplacement de nourrissons et tout-petits sous chargement durant les traitements de physiothérapie (Sandoz et al., 2011).

Pour une meilleure compréhension des réponses mécaniques du tronc pédiatrique, la propriété des tissus est également une préoccupation importante. De plus, les propriétés des os trabéculaires ont une influence négligeable sur les réponses des côtes par rapport à l'os cortical (Li et al., 2010), l'os cortical costal est l'intérêt principal dans cette thèse. Alors que les études sur les propriétés des côtes adultes sont nombreuses, peu d'études existent sur les côtes pédiatrique jusqu'à maintenant (Franklyn et al., 2007). Différents tests ont été effectués avec des sections de côtes

adultes ou petits échantillons sous différents protocoles, entraînant des résultats différents (Charpail et al., 2005; Cormier et al., 2005; Granik et al., 1973; Mitton et al., 2014; Stitzel et al., 2003; Subit et al., 2013; Yoganandan et al., 1998).

Très peu d'études sur les propriétés des matériaux (le module d'élasticité de Young et de résistance maximale) de l'os cortical costal existent dans la littérature pour l'enfant (Berteau et al., 2012; Agnew et al., 2013a; Agnew et al., 2013b). Une relation entre le module et l'âge de l'enfant est présentée Figure A3.2. Une relation globale pour deux études selon des protocoles différents est un défi. La Figure A3.2 suggère une augmentation du module de Young (E) en fonction de l'âge pour l'os cortical des côtes de l'enfant.

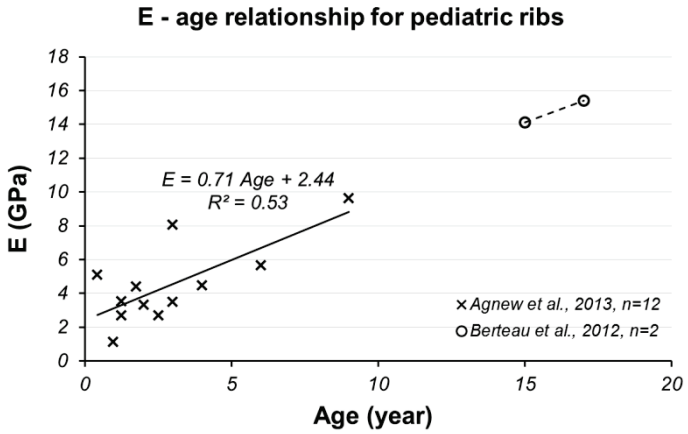

Figure A3.2: Le module de Young (E) en fonction de l'âge pour les côtes d'enfants, issu de Berteau et al., 2012 et Agnew et al., 2013a.

En conclusion, les propriétés des matériaux de l'os cortical des côtes humaines ont montré des variations dues aux différentes conditions d'essai, comme indiqué à la Figure A3.3. Pour la population des enfants, des tests biomécaniques ne sont pas faciles à réaliser. Une méthode non invasive devrait être considérée pour les études sur la population des enfants.

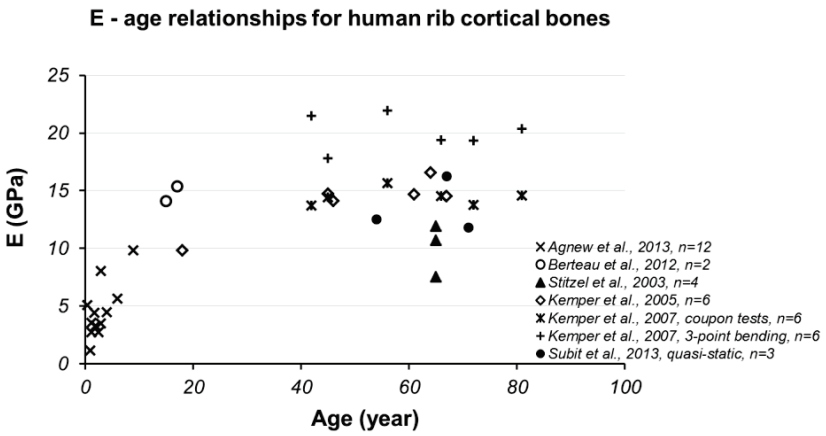

Figure A3.3: Le module de Young (E) en fonction de l'âge pour l'os cortical des côtes humaines, provenant d'études précédentes.

Comment les propriétés mécaniques pourraient-elles être évaluées de manière non invasive ? Certaines études ont montré que les propriétés mécaniques osseuses sont en corrélation avec la densité minérale osseuse (DMO), qui peut être mesurée par Quantitative Computed Tomography (QCT) de manière non invasive. Toutefois, cette méthode n'a pas été appliquée aux côtes. Y at-il des relations similaires entre les propriétés mécaniques et la DMO (évalués par QCT) sur les côtes humaines ? Cette méthode peut-elle être utilisée pour une population d'enfants ? Cette thèse vise à apporter des réponses à ces questions.

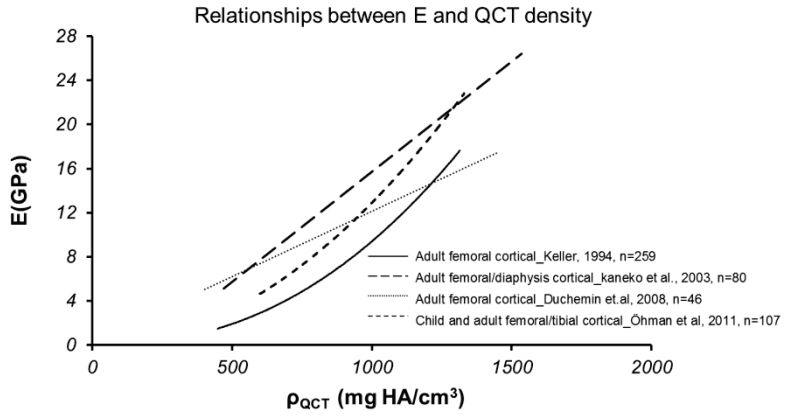

Figure A3.4: Les relations entre le module de Young (E) et les densités QCT (ρ_{QCT}).

A3.3 Chapitre 2 : Comportement mécanique *In vivo* du tronc pédiatrique et adulte pendant la kinésithérapie respiratoire

Ce chapitre discutera principalement du comportement mécanique du tronc pédiatrique et adulte *in vivo,* pendant la kinésithérapie respiratoire. Les données ont été recueillies dans un projet précédent sur l'enfant (Sandoz et al., 2011) et proviennent de données non-publiées chez l'adulte acquises au laboratoire. La principale contribution de ce travail est l'analyse des données et la rédaction d'un article (Zhu et al., 2014).

Huit patients pédiatriques âgés de 5 à 15 mois ont participé à cette étude. Tous les patients pédiatriques ont souffert de bronchiolite et étaient dans la phase de récupération. La kinésithérapie respiratoire a été utilisée pour accélérer leur rétablissement. Huit volontaires adultes en bonne santé âgés de 30 à 87 ans ont participé à l'étude. Les participants adultes ont été traités de la même manière.

Sandoz et al., 2011 décrit en détail la méthode de manipulation de la kinésithérapie respiratoire . Pendant les manipulations, les patients pédiatriques et adultes volontaires s'allongeaient sur une table de manipulation. Le kinésithérapeute a effectué des compressions multiples sur le tronc des enfants et des adultes. Une plateforme de force a été insérée dans la table de manipulation afin d'enregistrer la force de réaction. Sept cibles réfléchissantes ont été temporairement collées sur le dos des mains du kinésithérapeute. Seuls trois cibles visibles (sur chaque main) tout au long de l'enregistrement ont été sélectionnées pour l'étude. Deux caméras numériques synchronisées ont filmé la manipulation. Les coordonnées bidimensionnelles (2D) de chaque cible choisie ont été obtenues en utilisant le logiciel MotionTrack. Le déplacement 3D et centre de gravité géométrique de chaque cible ont ensuite été calculées à l'aide d'un objet d'étalonnage et d'une Transformation directe linéaire (DLT) de l'algorithme (Abdel-Aziz et al., 1971). A la fin de chaque manipulation, la vidéo enregistrée et la force mesurée ont été synchronisées à l'aide d'un capteur de contact électroluminescent.

La Figure A3.5 illustre un exemple des courbes de force et de déplacement synchronisés au cours du temps. Les courbes montrent la consistance de la force appliquée par le kinésithérapeute. Au cours de la manipulation, les patients pédiatriques étaient toujours beaucoup plus actifs que les volontaires adultes. Pour mieux contrôler les patients pédiatriques et parvenir à un meilleur effet thérapeutique, le kinésithérapeute a parfois chargé le tronc au maximum immédiatement, ensuite tenu le tronc de l'enfant, et enfin relâché la force. En revanche, le kinésithérapeute a appliqué une force plutôt constante sur le tronc des sujets adultes. Un décalage temporel de la force et du déplacement a été constaté chez les enfants et les adultes. Un plus grand laps de temps a été observé chez les enfants. Le rapport de décalage dans le temps des enfants est autour de 5% à 25 % et plus grand que celui des volontaires adultes, qui est inférieur à 5%.

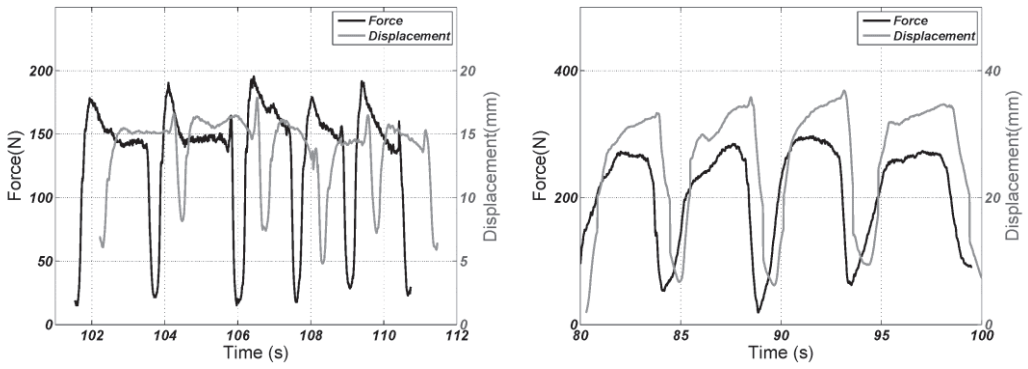

Figure A3.5: Courbes de force et de déplacement en fonction du temps. Gauche: garçon de 5 mois. Droite: sujet de 67 ans de sexe féminin. Le déplacement inclut la déformation du système.

Trois formes typiques de courbes de force-déplacement ont été observées dans cette étude, comme le montre la Figure A3.6. Ces différentes formes illustrent le comportement particulier *in vivo* des sujets vivants. Les formes différentes sont liées aux décalages temporels, ainsi qu'aux décalages temporels relatifs. Les formes I et II ont été principalement observées chez les volontaires adultes, qui ont des décalages temporels, ainsi que des décalages temporels relatifs plus petits. La forme III a été principalement observée chez les patients pédiatriques. Il faut noter que des formes I

et II ont coexisté chez certains volontaires adultes, tandis que les formes II et III ont coexisté chez certains patients pédiatriques.

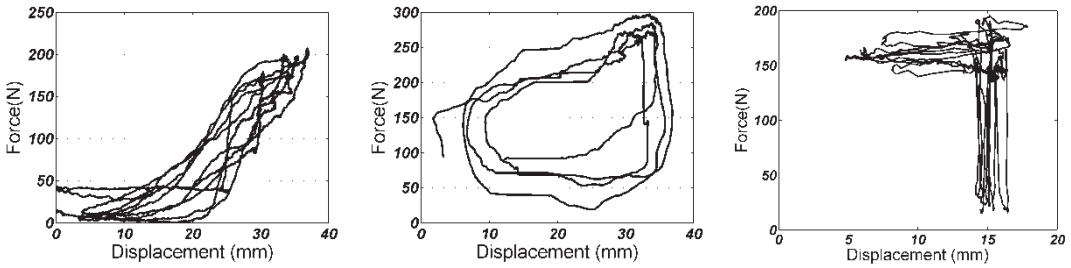

Shape I Shape II Shape III

Figure A3.6: Différentes formes de courbes force-déplacement. Gauche: 37 ans de sexe féminin. Moyen: 67 ans de sexe féminin. Droite: garçon de 5 mois. Le déplacement inclut la déformation du système.

La manière dont le kinésithérapeute a appliqué l'effort peut influencer la réponse en déplacement, comme le montre la Figure A3.7. Quelques modifications ont été apportées sur des volontaires adultes. Le kinésithérapeute a changé le schéma de chargement sur un adulte de 30 ans. Un chargement rapide (cycle de chargement 1 dans la Figure A3.7) pourrait entraîner la Forme II de courbes force-déplacement alors que le chargement progressif (cycle de chargement 2 dans la Figure A3.7) a entraîné Forme I de courbes force-déplacement.

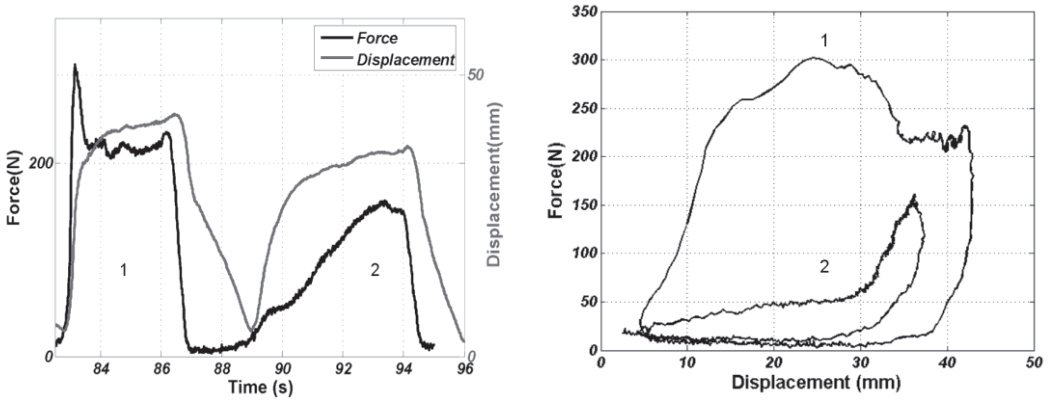

Figure A3.7: Modèles de charge différentes dans un volontaire adulte de 30 ans. Gauche: courbes de force et de déplacement au cours du temps. Droite: courbes force-déplacement.

Ce chapitre a étudié la réponse mécanique des troncs des enfants *in vivo* et des adultes actifs au cours de la kinésithérapie respiratoire. Trois formes typiques de courbes force-déplacement ont été observées. Un décalage temporel plus grand entre la force et le déplacement a été observé plus fréquemment chez les enfants que chez les adultes. Différents décalages ont abouti à différentes formes de courbes force-déplacement entre les enfants et les adultes. Certains facteurs, y compris la respiration, la contraction musculaire et les modèles de chargement font partie des hypothèses pour expliquer ce phénomène.

Ce chapitre a également fourni des données fondamentales concernant la réponse mécanique du tronc pédiatrique et adulte sous un faible taux de compression et en infra lésionnel. Des données complémentaires (par exemple, l'activité musculaire, la respiration) doivent être collectées à l'avenir pour aller vers la modélisation *in vivo* du tronc.

A3.4 Chapitre 3 : Les relations entre les propriétés mécaniques et la densité minérale osseuse de l'os cortical costal

Pour une meilleure compréhension des réponses mécaniques du tronc pédiatrique, la propriété des tissus est également une préoccupation importante. Les chapitres suivants présenteront l'étude des propriétés mécaniques des tissus. Le but de ce chapitre est de trouver des relations entre la DMO mesurée par QCT (tomodensitométrie quantitative) et le module d'élasticité, ainsi que la résistance à la rupture (sur la base des expériences biomécaniques) pour l'os cortical costal chez l'adulte.

Sept sujets ont été obtenus auprès du Département Universitaire d'Anatomie Rockefeller (Lyon, France) à travers le programme de français de don de corps à la science, dont 6 hommes et 1 femme âgée de 65 à 85 ans (moyenne : 76,6, SD : 7,6). Treize segments de côte de 120 mm de longueur ont été prélevés sur la partie latérale des côtes 6 ou 8 dans la partie la plus rectiligne. Les segments ont été conservés

congelés à - 20 °C. Ils ont été décongelés à 4 °C pendant 12 heures et à 20 °C pendant 2 heures avant les mesures.

Avant de prélever les segments de côte, tous les sujets ont eu un scanner corps complet par QCT. Ensuite, les images QCT de la cage thoracique ont été reconstruites en 3D. Pour chaque côtes 6 et 8, 100 images transversales également réparties de la vertèbre au sternum ont été extraites selon la méthode qui a été détaillée dans Sandoz et al., 2013b. La DMO moyenne (ρ_{CT}, dans mg HA/cm^3) de la section transversale de la côte a été calculée. Pour chaque côte étudiée, 10 images de sections transverses à la ligne moyenne de la côte, entre 5 % à 95 % de la longueur entre les vertèbres et le sternum, ont été sélectionnées.

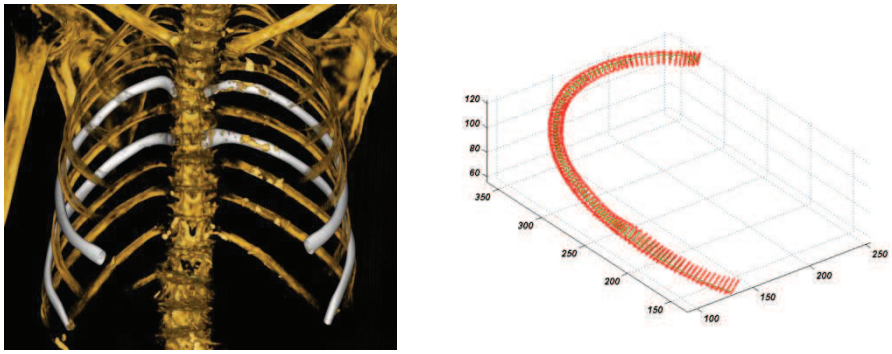

Figure A3.8: A gauche: la reconstruction 3D de la cage thoracique des tranches CT, les côte blanches sont les 6ème et 8ème côtes; à droite: un exemple de 100 images équidistantes de la vertèbre au sternum.

Les 13 segments de côte ont été mesurés par HR-pQCT (tomodensitométrie haute résolution périphérique quantitative). La DMO moyenne ($\rho_{HR\text{-}pQCT}$, en mg HA/cm3) des segments de côte a également été calculée.

Les propriétés mécaniques (module d'Young E et maximale de résistance à la flexion σ_{max}) des 13 échantillons de côte ont été obtenus précédemment (Mitton et al., 2014) et ces données ont été réutilisés dans cette étude. La méthode a été détaillée annexe 1.

Figure A3.9 montre la répartition de la DMO moyenne ainsi que l'écart-type le long de la côte. Des valeurs plus élevées de la DMO ont été observées dans la partie latérale par rapport aux parties antérieures et postérieures.

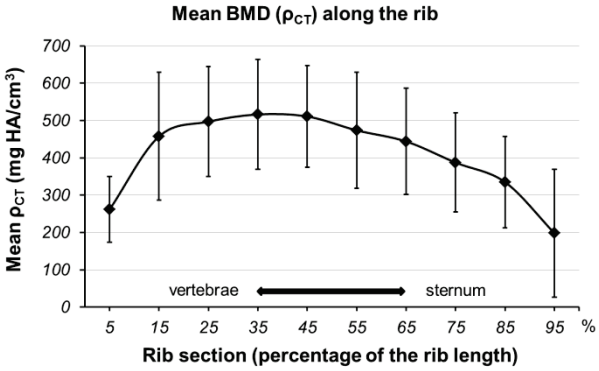

Figure A3.9: Moyenne et écart type de la côte le long de la DMO (mesurée par QCT, n = 13).

La DMO mesurée par HR-pQCT était significativement corrélée avec les propriétés mécaniques ($p < 0,01$), comme le montre la Figure A3.10.

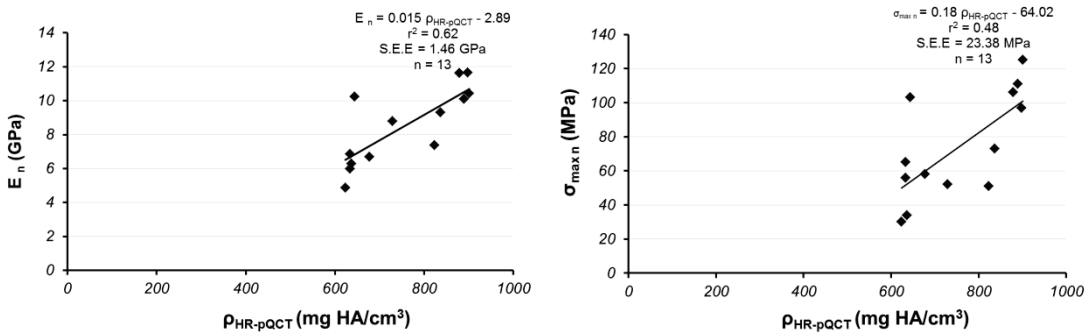

Figure A3.10: Les corrélations entre la DMO mesurée par HR-pQCT et les propriétés mécaniques.

Cette étude a fourni des relations entre la DMO et les propriétés mécaniques de l'os cortical de côtes humaines. Il a été constaté que la relation $\rho_{HR\text{-}pQCT}$ - E pour l'os cortical costal dans la présente étude suit le même nuage de points que l'os cortical fémoral dans les études précédentes, comme le montre la Figure A3.11. Cela peut indiquer que l'os cortical des côtes humaines pourrait présenter la même relation DMO - E que l'os cortical d'autres sites anatomiques. Par ailleurs, l'étude de Öhman et al., 2011 a suggéré que les enfants et les adultes partagent la même relation entre les propriétés mécaniques et la DMO. Les relations trouvées dans ce chapitre seront donc

utilisées sur une population d'enfants, pour estimer les propriétés mécaniques de l'os cortical des côtes.

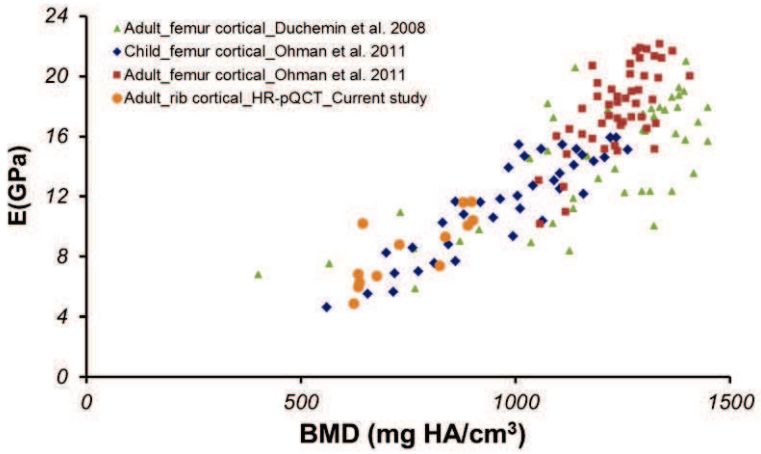

Figure A3.11: Les relations entre la DMO et les propriétés mécaniques (les données de Öhman et al., 2011 sont issus d'une combinaison des résultats de Öhman et al., 2011 et Kaneko et al., 2003).

Cette étude a fourni des relations significatives entre les propriétés mécaniques des côtes os cortical humain et la DMO mesurée par QCT et HR-pQCT. Ces relations linéaires pourraient être utilisées pour prédire les propriétés mécaniques des côtes, à partir d'images tomodensitométriques. Cette étude *ex vivo* est une première étape vers la prédiction des propriétés mécaniques de l'os cortical des côtes humaines *in vivo*. Dans le chapitre suivant, La DMO de l'os cortical des côtes des enfants, et les relations entre les propriétés mécaniques et la DMO (pour les adultes) seront utilisées pour estimer les propriétés mécaniques de l'os cortical des côtes des enfants.

A3.5 Chapitre 4 : Estimation *in-vivo* des propriétés mécaniques de l'os cortical des côtes pédiatriques

Dans le chapitre précédent, des relations entre les propriétés mécaniques et la DMO de l'os cortical des côtes adultes ont été trouvées. L'objectif principal de ce chapitre est d'estimer le module d'élasticité, ainsi que la résistance à la rupture de l'os cortical

des côtes des enfants *in vivo*, fondées sur des relations propriétés mécaniques - DMO qui ont été trouvées sur côtes adultes.

Vingt-huit patients pédiatriques dont 14 garçons et 14 filles âgés de 9 mois à 19 ans ont participé à cette étude. Les patients ont été divisés en 7 groupes en fonction de l'âge (4 patients par groupe). Pas de fracture de côte ou d'autre maladie thoracique ont été diagnostiquée. Les acquisitions ont été effectuées à l'Hôpital Femme Mère Enfant (Hospices Civils de Lyon, France), avec un même scanner.

La méthode utilisée pour obtenir la DMO de côtes a été décrite dans le chapitre précédent. Pour chaque côte 6 des patients, 100 images transversales équidistantes de la vertèbre au sternum ont été extraites. La DMO moyenne des sections transversales de la côte a ensuite été calculée.

Les résultats suggèrent que la variation de HU pourrait être inférieure à 1% dans les mêmes conditions d'analyse. Dans ce cas, l'étalonnage des images QCT pourrait être effectué une fois. Si le type de filtre ou le dispositif d'imagerie a été modifié, la variation de HU pourrait être inférieure à environ 10%. La nécessité de l'étalonnage pour les images QCT pourrait dépendre de l'acceptation de la modification. Une modification de la tension du tube pourrait conduire à une plus grande variation de HU. Pour le compartiment de référence qui a une densité de 375,8 mg K_2HPO_4/cm^3, la variation de HU pourrait atteindre 37%. Comme le montre le tableau A3.1., le calibrage de chaque acquisition est nécessaire dans ce cas.

Sur la base des relations propriétés mécaniques - DMO trouvées sur les adultes, les propriétés mécaniques de l'os cortical des côtes pédiatriques ont été estimées. Il a été constaté que les propriétés mécaniques des côtes augmentent puis diminuent des vertèbres à sternum. En outre, les propriétés mécaniques augmentent avec l'âge, comme le montre la Figure A3.12.

Tableau A3.1: La variation de HU sous différentes configurations d'aquisition.

Configuration	Variation de HU	Recommandation
Mêmes conditions: dispositif de CT, type de filtre, de tension de tube ... n = 12	< 1%	Calibration une fois.
Différents types de filtres (filtre os / tissus mous) même CT, même tension de tube (120 kV) n = 12	5% - 10%	Calibration une fois ou chaque fois
Les différents types de filtres, différents appareils de tomodensitométrie (3 appareils) même tension du tube (120 kV) n = 47	6% - 8%	Calibration une fois ou chaque fois
Tension du tube différente (120 kV et 80 kV) même CT, même type de filtre n = 51	12% - 37%	Calibration à chaque acquisition.

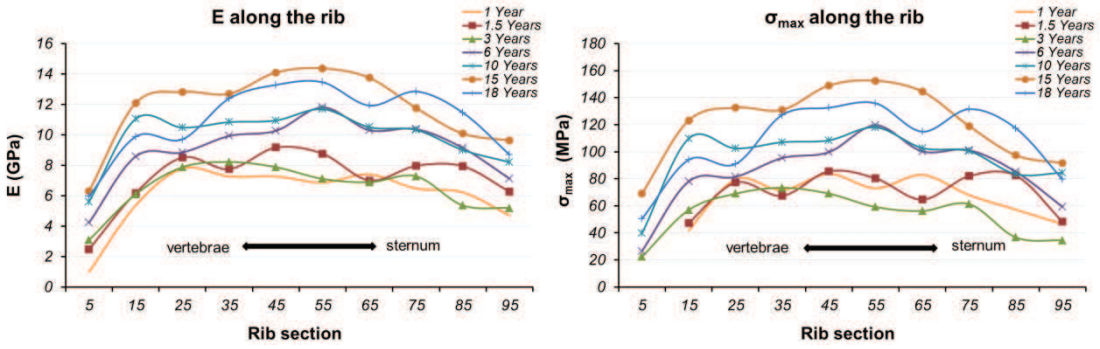

Figure A3.12: Les propriétés prédites : élasticité (E) et la résistance à la flexion maximale (σ_{max}) le long de la côte.

Les valeurs des propriétés des matériaux augmentent avec l'âge. Les valeurs moyennes de module d'élasticité et la résistance à la flexion maximale dans chaque groupe d'âge ont été calculées, et ont montré une tendance croissante le long de l'âge, comme le montre la Figure A3.13.

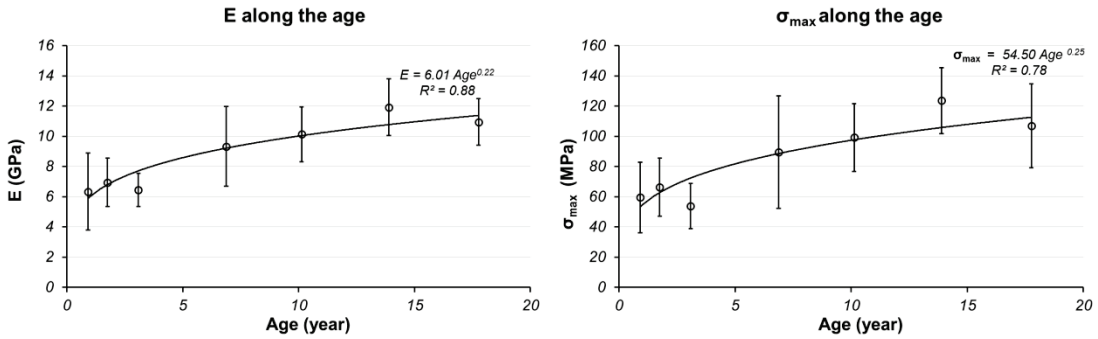

Figure A3.13: Les propriétés prédites : élasticité (E) et résistance à la flexion maximale (σ_{max}) en fonction de l'âge.

La Figure A3.14 présente le module d'élasticité des côtes selon l'âge sur la base des données provenant de l'étude en cours et des études précédentes.

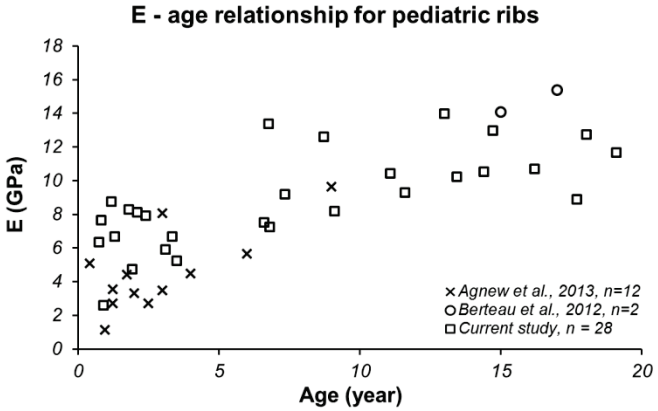

Figure A3.14: Module d'élasticité de côtes en fonction de l'âge des sujets, provenant de Berteau et al., 2012 et Agnew et al., 2013a et de l'étude en cours.

Cette étude a évalué les propriétés mécaniques de l'os cortical des côtes pédiatriques *in vivo* pour la première fois. Cette méthode non-invasive a surmonté l'inconvénient du manque de tissus pédiatriques pour la recherche en biomécanique. Les propriétés des matériaux ont été trouvées plus hautes dans la partie latérale des côtes que les régions antérieure et postérieure. Les propriétés des matériaux augmentent avec l'âge de la population des enfants. Cette étude ouvre la voie à l'estimation des propriétés mécaniques de l'os cortical pédiatrique *in vivo*.

A3.6 Conclusion

Le tronc de l'enfant est le principal segment lésé lors de la survenue d'un accident. Les modèles physiques et numériques de l'enfant sont des outils importants pour comprendre le comportement des enfants lors d'un impact. Cependant, pour développer ou valider un modèle de l'enfant, les connaissances biomécaniques sont encore limitées. Cette thèse a visé à fournir plus de connaissances sur le comportement mécanique de l'enfant *in vivo*, avec une attention particulière pour le tronc. La réponse mécanique du tronc sous charge pendant des manipulations de kinésithérapie respiratoire et les propriétés mécaniques de l'os cortical des côtes ont été principalement étudiées.

Le premier chapitre a présenté les caractéristiques anatomiques spécifiques des enfants. Il existe des variations considérables d'anatomie et de propriétés mécaniques des tissus pour les enfants, en cours de croissance. Contrairement aux adultes, les données concernant les enfants peuvent difficilement être obtenues directement à partir d'essais sur des cadavres ou des tissus provenant de cadavres. Pour contourner cette limitation, des méthodes *in vivo* sont attendues pour les études sur les enfants. Certaines méthodes qui pourraient être utilisées pour étudier les réponses biomécaniques des enfants dans des environnements cliniques ont été proposées. La réponse mécanique du thorax a déjà été évaluée à l'aide des courbes de force en fonction du déplacement. Toutefois, ces courbes ont été trouvées différentes les unes par rapport aux autres. Ces différences proviennent-elles des méthodes ou de la population ? Pour répondre à cette question, l'objectif du chapitre 2 a été d'explorer les caractéristiques force et de déformation de tronc de l'enfant sous chargement *in vivo*.

Le chapitre 2 a quantifié et a expliqué la réponse mécanique *in vivo* du tronc de l'enfant et de l'adulte sous charge pendant des manipulations de kinésithérapie respiratoire. Des décalages en temps entre les courbes de force en fonction du temps et les courbes de déplacement en fonction du temps ont été observés. Ces décalages ont abouti à différentes formes de courbes de force en fonction du déplacement. Les facteurs, comme la respiration, la contraction musculaire et le modèle de chargement font partie des hypothèses retenues pour expliquer ce phénomène. Les déplacements

maximaux des troncs des enfants et des adultes étaient de 18 mm et 44 mm, respectivement, avec une charge maximale de 208 N et 250 N, respectivement. Le chapitre 2 a fourni une meilleure explication des caractéristiques *in vivo* de la relation de la force en fonction du déplacement du tronc de l'enfant et de l'adulte sous chargement infra lésionnel.

Pour une meilleure compréhension des réponses mécaniques du tronc de l'enfant, les propriétés mécaniques des tissus sont également une préoccupation importante. L'os cortical des côtes a été l'objet principal dans cette thèse. Des études antérieures ont démontré que les propriétés mécaniques osseuses sont corrélées à la DMO, qui peut être mesurée par QCT *in vivo*. Toutefois, cette méthode n'a pas été appliquée aux côtes. Ainsi, le chapitre 3 a exploré cette méthode *ex vivo* et le chapitre 4 a appliqué cette méthode sur une population d'enfants pour estimer les propriétés mécaniques de l'os cortical des côtes de l'enfant.

Le chapitre 3 a fourni des relations significatives entre les propriétés mécaniques de l'os cortical des côtes de l'adulte et la DMO mesurée par QCT et HR-pQCT. La DMO mesurée par HR-pQCT était significativement corrélée au module d'élasticité et à la contrainte limite en flexion de l'os cortical des côtes de l'adulte (r^2 variait de 0,48 à 0,75, $p < 0,01$), tandis que la corrélation entre la densité minérale osseuse mesurée par QCT et le module élastique et la contrainte limite en flexion étaient un peu moins fort (r^2 variait de 0,22 à 0,50, $p < 0,08$). En comparaison avec les résultats de la littérature, les relations entre les propriétés mécaniques et la DMO évalués par HR-pQCT sur les côtes de l'adulte sont proches de celles de l'os cortical du fémur humain. La DMO mesurée par QCT et HR-pQCT sont différentes mais elles sont liées de façon linéaire. Etant donné que la DMO peut être mesurée par des images QCT dans un environnement clinique, ces relations linéaires pourraient être utilisées pour prédire les propriétés mécaniques de l'os cortical des côtes *in vivo*. Cette étude est une première étape vers la prédiction des propriétés mécaniques de l'os cortical des côtes de l'enfant *in vivo*.

Le chapitre 4 a discuté principalement sur deux questions. La première partie de ce chapitre a principalement étudié les fantômes de calibration, qui ont été utilisés pour

convertir les valeurs en unité Hounsfield (HU, Hounsfield Unit) des images QCT à la DMO. On a constaté que les valeurs en HU n'étaient pas stables dans les différentes conditions de tomodensitométrie. La variation en HU pouvait être inférieure à 1 % dans une condition identique et constante. Le changement des appareils de TDM et d'autres paramètres (courant du tube, type de filtre, etc.) peut conduire à environ 7% - 8 % de variation de la valeur en HU. La tension du tube a été le paramètre le plus sensible, elle peut conduire à une variation de 37% de la valeur en HU. Il a été suggéré d'effectuer les analyses avec un fantôme d'étalonnage à chaque fois, pour obtenir une valeur plus précise de la DMO. La deuxième partie de ce chapitre a estimé les propriétés des matériaux de l'os cortical des côtes de l'enfant *in vivo*. Les propriétés des matériaux ont été trouvées plus élevées dans la partie latérale de côtes que dans les régions antérieures et postérieures. Il a été constaté que les propriétés des matériaux de l'enfant augmente en fonction de l'âge. Les propriétés des matériaux estimés étaient comparables aux études précédentes. Combiné avec d'autres études sur l'os cortical humain, il a été suggéré que l'os cortical des côtes humaines partage la même relation entre le module élastique et la DMO que l'os cortical d'autres os. Cette étude a évalué les propriétés des matériaux de l'os cortical des côtes de l'enfant pour la première fois *in vivo*.

Certaines limites doivent être indiquées. Tout d'abord, pour la réponse mécanique du tronc de l'enfant pendant des manipulations de kinésithérapie respiratoire, les caractéristiques, de la force en fonction du déplacement, étudiées ne représentent pas la réaction réelle du tronc dans le cas d'un accident, puisque la vitesse de chargement est beaucoup plus basse que celle lors d'accidents réels. Cependant, cette étude a fourni des données fondamentales concernant la réponse mécanique dans des conditions infra lésionnelles, de chargement. Deuxièmement, la DMO se révèle être un bon prédicteur des propriétés mécaniques de l'os cortical des côtes de l'enfant. Toutefois, la densité minérale osseuse mesurée *in vivo* n'est pas aussi précise que celle mesurée *ex vivo*, mais il s'agit de la limitation des techniques d'imagerie médicale. Évidemment, l'étude de plus de sujets renforcerait ces résultats.

L’ensemble des résultats peut maintenant être implémenté pour la modélisation des enfants. Il sera intéressant d'étudier la sensibilité des modèles numériques de l’enfant à l'aide de ces nouvelles données sur l’os cortical des côtes de l’enfant. Cependant, le thorax est une structure complexe, en plus des côtes, les propriétés mécaniques des cartilages et des muscles sont également importantes. Des travaux futurs pourraient être menés sur les propriétés mécaniques d’autres tissus du tronc.

Cette étude a montré que le comportement mécanique de la population des enfants pourrait être étudié *in vivo*, par des traitements médicaux ou des techniques d'imagerie médicale. Cette étude ouvre la voie des études *in vivo* sur la population des enfants. La méthode non-invasive dans cette étude pourrait être appliquée sur d'autres sites anatomiques de l’enfant.

Pour le long terme, toutes les nouvelles connaissances biomécaniques sur la population des enfants peuvent conduire à des modèles numériques plus biofidèle, qui peuvent avoir une application plus large que la biomécanique des chocs.